Nonlinear Dynamics of Nanoscale Systems

Thesis by

Nathan Oken Hodas

In Partial Fulfillment of the Requirements

for the Degree of

Doctor of Philosophy

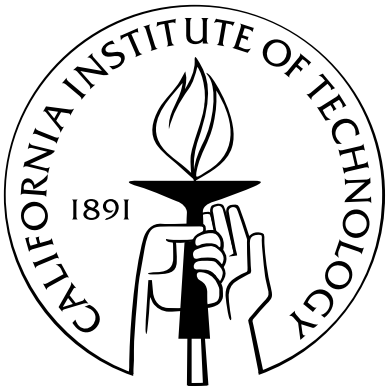

California Institute of Technology

Pasadena, California

2011

(Defended May 6, 2011)

"The Sun is a mass of incandescent gas..."

—*Why Does the Sun Shine?* by They Might by Giants

"The Sun is a miasma of incandencent plasma. The Sun's not simply made of gas... That thesis has been rendered invalid!"

—*Why Does the Sun Really Shine?* by They Might be Giants

Acknowledgements

I am honored to thank so many people for helping and guiding me over the past years.

I learned a great deal in my previous life in Hideo Mabuchi's lab. Mike Armen and Andy Berglund made great squash partners as well as great tutors, enthusiastically teaching me all about optics and electronics. I really appreciate Ramon van Handel's patience with my questions about Markov processes and the Fokker-Planck equation. Kevin McHale and Asa Hopkins were great office- and benchmates. I also want to thank Tony Miller, John Au, John Stockton, Ben Lev, Nicole Czakon, Gopal Sarma, Orion Crisafulli, and Joe Kerckhoff. The quantitative finance seminar with Luc Bouten and Tim McGarvey was fun and a welcome diversion when I was trying to get over the hump of my third and fourth year, plus I now understand the Ito calculus. Of course, the other member of the Mabuchi lab to remain at Caltech, Sheri Stoll, was both a friend and a resource, and without her I would not know about Liō, the boy who loves giant squid.

A tip from Andy started a collaboration with Kris Helmerson at NIST. It was there I really learned about single molecule microscopy. I thank Kris for hosting me in Maryland for those many weeks. I enjoyed worked closely with Jauyang Tong and Ana Jofre, with whom I spent many hours in a darkened tent trying to catch droplets

of water with a laserbeam. Many thanks to Rani Kishore for working with me to advance the hydrosome project, doing much of the DNA wet work, and teaching me the best ways to prepare pristine samples. It was a shame we could never get things to work completely before Hideo left for Stanford, but my time at NIST also taught me that cutting edge research requires squashing gremlin after gremlin. Otherwise, it would have been done already! I have many thanks for Hideo for supporting me and encouraging me, and I know I have missed out on a lot by not following the lab to Stanford. That said, I have no regrets for staying at Caltech.

I have many people to thank in my second life at Caltech. The members of the Marcus lab, past and present, were great companions at our Friday lunches, Zhaoyan Zhu, Wei-Chen Chen, Yousung Jung, Evans Boney, Maksym Kryvohuz, Nima Ghaderi, and Yun-Hua Hong. I also want to thank Jau Tang for help with the GFPmut2 project and Yanting Wang for doing the simulations for the SFG work. I want to extend extra thanks to Evans and Nima for sharing so many great conversations and for productive collaborations. It is hard to express adequate appreciation for the mentorship and advising from Rudy. Every minute was enlightening and informative, and I was lucky to be able to work with someone so dedicated to his students and supportive of my interests.

In the Fraser lab, I also have many people to thank. Aura Keeter was indispensable for helping me find my way around the lab and helping with maxi-preps and getting machines to work. I extend similar appreciation to Mary Flowers, the lab mom, Kristy Hilands, the former lab administrator, and Pat Anguiano, Scott's admin. I

am indebted to the help from Christie Canaria, who shared so many reagents and protocols with me. I have special thanks for Thai Truong for helping me with the microscopes and many helpful discussions. I also thank Jeff Fingler for our last minute attempts to use OCT to measure the refractive index of zebrafish. It was worth a try. Thanks to Jelena Culic-Viskota for tirelessly working to perfect the SHG nanoparticles. WIthout Andres Collazo, I would not have had access to the House Ear Institute's Zeiss 710, and he was great to talk to while sitting in that dark, cold room. Thanks to my officemates, Mat Barnet, Cambrian Liu, and, recently, Danielle Bower. I would not have even had an office if it weren't for the generosity of Larry Wade, who knew exactly what I was going through when we were both struggling to get things to work. To my closest collaborators, Bill Dempsey and Laki Pantazis, you both taught me a great deal, and I would not be graduating now if it weren't for your help and advice. You have also been good friends, and I was lucky to find such great partners. I also thank the other members of the lab for their support, including Le Trinh, Luca Caneparo, Roee Amit, Max Ezin, Alana Dixon, Greg Reeves, Frederique Ruf, David Huss, David Koos, and Dave Wu. Of course, I extend my deep thanks to Scott Fraser, whose advice and insight proved vital over and over. Without your great sense for experimental design, I would still be shooting lasers at globs of barium titanate, and I am honored that you were willing to support me after Hideo left.

There were many people outside the lab who helped me reach this point. Edgardo Garcia was the right person at the right time to help me, and I'm lucky to have him as a friend. Best of luck in San Jose. Of course, all of my fellow RAs helped me

successfully navigate the world of the Caltech undergraduate housing system. Also, many thanks to Dean Barbara Green, Sue Chiarchiaro, Geoff Blake, and Tim Chang for helping us overcome so many challenges with the students. Ruddock House was our home for three years, and it was an amazing time. We laughed, we cried, and we learned a lot about life. It was the second half of my life at Caltech, outside research, and it was very fulfilling.

I am lucky to have such a loving family to help me through. As a new parent, I am now doubly aware how nurturing and supportive my parents have been at every step of my life. I don't know how they dealt with me, but I am lucky to have them. Of course, it's easy to thank little Leo. There is nothing like coming home to his bright face to help me relax and recharge, and my productivity significantly increased after he joined us. He even literally inspired a section of my thesis, and he is duly noted in that chapter. Last, it is hard to overstate the help I got from my wife and best friend, Jenn. From helping me purify GFPmut2 to supporting our family while I went into hermit mode to write my thesis, she was there every step of the way; and I am lucky to have such a caring companion, and I look forward to spending many future happy years together. This work is dedicated to you. Love, Sq.

Abstract

This work builds theoretical tools to better understand nanoscale systems, and it explores experimental techniques to probe nanoscale dynamics using nonlinear optical microscopy. In both the theory and experiment, this work harnesses nonlinearity to explore new boundaries in the ongoing attempts to understand the amazing world that is much smaller than we can see. In particular, the first part of this work proves the upper-bounds on the number and quality of oscillations when the system in question is homogeneously driven and has discrete states, a common way of describing nanoscale motors and chemical systems, although it has application to networked systems in general. The consequences of this limit are explored in the context of chemical clocks and limit cycles. This leads to the analysis of spontaneous oscillations in GFPmut2, where we postulate that the oscillations must be due to coordinated rearrangement of the beta-barrel. Next, we utilize nonlinear optics to probe the constituent structures of zebrafish muscle. By comparing experimental observations with computational models, we show how second harmonic generation differs from fluorescence for confocal imaging. We use the wavelength dependence of the second harmonic generation conversion efficiency to extract information about the microscopic organization of muscle fibers, using the coherent nature of second

harmonic generation as an analytical probe. Finally, existing experiments have used a related technique, sum-frequency generation, to directly probe the dynamics of free OH bonds at the water-vapor boundary. Using molecular dynamic simulations of the water surface and by designating surface-sensitive free OH bonds on the water surface, many aspects of the sum-frequency generation measurements were calculated and compared with those inferred from experiment. The method utilizes results available from independent IR and Raman experiments to obtain some of the needed quantities, rather than calculating them *ab initio*. The results provide insight into the microscopic dynamics at the air-water interface and have useful application in the field of on-water catalysis.

Contents

Acknowledgements **iv**

Abstract **viii**

1 Introduction **1**

2 Oscillations on Networks **6**

2.1 The Limits of Oscillations in Overdamped Systems 8

2.2 The Limits on Oscillations 10

2.3 Oscillations in Macrostates: Chemical Clocks 13

2.4 Oscillations in Green Fluorescent Protein GFPmut2 18

2.4.1 Limit Cycles 21

2.4.2 Loop Dynamics 30

2.5 Conclusion 36

3 Endogenous Second Harmonic Generation in Zebrafish **39**

3.1 Structure of Muscle 42

3.1.1 Muscle Construction 42

3.1.2 Optical Properties of Muscle 47

3.2 Methods for Measuring Second Harmonic Generation 52

3.3 Discussion 59

3.3.1 Representative Images 59

3.3.2 Wavelength-Dependent SHG 63

4 Theory of Second Harmonic Generation from Zebrafish Muscle 74

4.1 Foundations of Nonlinear Optics 74

4.2 SHG Phase-Matching with Focused Light 79

4.2.1 The Paraxial Approximation of the Wave Equation 80

4.2.2 SHG from Periodic Media 82

4.3 Explaining Patterns in Muscle Structure 90

4.4 Wavelength Dependence of SHG 95

4.4.1 Wavelength Dependence Due to Myofibril Packing 99

4.4.2 Wavelength Dependence Due to Collection Efficiency 102

4.5 Conclusion 105

5 Microscopic Structure and Dynamics of Air/Water Interface by Computer Simulations and Comparison with Sum-Frequency Generation Experiments 107

5.1 Methods 109

5.2 Results and Discussion 122

5.3 Conclusion 124

Bibliography 129

List of Figures

2.1 The region R_N in the complex plane contains all possible eigenvalues of N-dimensional stochastic matrices with unit spectral radius 12

2.2 Oscillations as a function of system size 14

2.3 The effect of system size on macrostate oscillations 14

2.4 Ribbon representation of GFP 22

2.5 The local neighborhood of the GFP chromophore 23

2.6 When the chromophore is anionic its excess charge draws its tightly coupled neighbors into alignment with the chromophore. When neutral, the amino acids are now free to preferentially align with their neighbors, increasing the structural rigidity of the β-barrel. 27

2.7 Oscillations produced by two-variable model 28

2.8 Phase-space dynamics of GFPmut2 denaturing 31

2.9 Time-dependent rates create a transition from a static system to a limit cycle. 32

2.10 Illustration of secondary and tertiary structure of GFP 33

2.11 Baby Leo's toy, the bead maze, is an example of linear motion producing a periodic signal. 36

3.1 Sagittal section of zebrafish 36 hours post fertilization, with composite brightfield 41

3.2 Anatomical planes. Zebrafish are oriented laterally, meaning the sagittal plane is parallel to the ground and perpendicular to the laser. 42

3.3 Label-free image of fixed zebrafish embryo, sagittal section. 43

3.4 Second harmonic generation from muscle and collagen 44

3.5 (a) A multiscale illustration of muscle organization, and (b) a cartoon of the process of muscle contraction. 46

3.6 TEM micrographs of myofibril crosssection, showing hexagonal packing of myosin and actin. 47

3.7 TEM images of muscle fibers 48

3.8 Reflection of 850 nm laser pulses indicates the optical density of the zebrafish transverse section 50

3.9 Using experimentally measured refraction index data from porcine muscle [120] (total internal reflection), we determine the refractive index across the entire spectrum. Points are experimental data, line is fit by eq. (3.1). 52

3.10 Each element of the imaging pathway has different wavelength dependent transmission or sensitivity. 55

3.11 Fluorescent debris from the zebrafish were used to measure point spread functions at 790 nm, 850 nm, and 890 nm, using 25x 0.8 NA 56

3.12 An image of second harmonic generation from morphant zebrafish, optically sectioned along the sagittal plane. Lesions are evidenced by the circular outlines of luminescence. 57

3.13 Epithelial cells accumulate damage over a 2 minute exposure to 820 nm Ti-Sapphire laser pulses 58

3.14 High maginfication view of discrete structure of myofibrils. 60

3.15 Second harmonic generation from wildtype. 61

3.16 Inset shows magnified view of herringbone or “vernier” pattern from a 7 day post-fertilization zebrafish. 62

3.17 Transgenic fish were used to visualize the interface between myofibril SHG and fluorescent-protein labeled membranes and nuclei 67

3.18 Multiple views of membrane-labeled wildtype zebrafish 68

3.19 Second harmonic generation from zebrafish morphant muscle. 69

3.20 Comparison of SHG from sagittal sections between (a) wildtype and (b) morphant. 70

3.21 The wavelength dependent SHG detected from a single sagittal plane of 5-day old zebrafish 71

3.22 Normalized intensity spectrum density map of points from figure 3.21 of low-intensity background points. 72

3.23 The wavelength dependent SHG detected from a single coronal plane of 5-day old morphany zebrafish 73

4.1 Second harmonic generation production efficiency depends on the magnitude of the phase-matching, Δk, determined by eq. (4.7). Absent perfect phase-matching, corresponding to $\Delta k = 0$, SHG can only be produced across a distance constrained by $\Delta k \Delta x < 2\pi$. 79

4.2 With a focused beam, the conversion efficiency is very sensitive to the magnitude and sign of the phase-matching, Δk, as well as the width of the medium, $z_f - z_0$. $b = 0.5$ 83

4.3 Theoretical calculations illustrate the qualitative difference between SHG and two-photon fluorescence 92

4.4 Tilting the laser causes the SHG doublets to disappear 96

4.5 The nonlinear susceptibility of muscle, $\chi^{(2)}(\omega)$, based on Miller's rule. . 97

4.6 Plot of SHG susceptibility map. Here, $p = 2$. 101

4.7 ℓ_c as a function of wavelength for the refractive index defined in Eq 3.1. All units are μm. 101

4.8 Fit of eq. (4.37) using the quasi-phase-matching structure in eq. (4.36), with $p = 5$ μm. The experimental data are from figure 3.21. The x-axis is wavelength in nanometers, and the y-axis normalized intensity. . . . 102

4.9 SHG emission has angular dependence 103

4.10 The wavelength dependent SHG may also be due to the variation of the size of the laser focus. Here, the SHG active region was constrained to a box extending $5.2b$ along the z-axis and $1.9w_0$ along the x- and y-axis. 104

5.1 The simulated water/vacuum interface 126

5.2 Probability density of the cosine of the tilt angle with respect to the surface normal 127

5.3 Correlation functions of free OH bonds produced by simulation, using three different snapshot times, 1 , 10 , and 100 fs. 128

List of Tables

5.1 Average number of free surface OH bonds, $\langle N_{OH} \rangle$, and average orientation angle, $\langle \theta_{OH} \rangle$, of free surface OH bonds calculated from three MD simulations with different snapshot time intervals 125

5.2 Results of fitting the calculated spectrum to a Lorentzian and correcting for experimental width. 125

Chapter 1

Introduction

The nanoscale is the spatial regime at least 10 times larger than atoms and simple molecules, yet also 10 times too small to be resolved by the unaided human eye. Such small things are often readily disturbed by the constant jostling of their air and liquid environments. A grandfather clock that is 50 nm tall will not tick, no matter how precisely it is machined. A bacteria does not swim by paddling through water like a fish, instead it moves by spinning a flagella. Making things smaller can make them different. Gold, when broken down into 10 nanometer crystals, transforms in color from the familiar shiny metal into a deep red, and silver turns yellow. Hence, nanotechnology is exciting not just because we can make big things smaller but because we can make new things.

A crystal composed of thousands or millions of atoms may have completely differently properties from its isolated constituent atoms and may also be different from a larger version of the same crystals. At first, this would be no surprise to someone like a baker, who transforms unpalatable flour, salt, baking soda, fat, and sugar into delicious doughnuts. But, making a doughnut is a series of chemical reactions, while the changes in size-dependent properties occur spontaneously. A better analogy would be

making a doughnut by cutting it out of a pizza, and suddenly it was sweet and savory, or by squeezing two pieces of rye bread together and ending up with tasty dessert. These metaphors are drawn from examples in this thesis, where we explore how the optical properties of water at the water-vapor boundary are different from those in the liquid bulk. We prove that making a system larger may allow it to oscillate longer and more predictably. Finally, we consider how the microscopic arrangement of protein fibers in muscle interact nonlinearly with laser light, yet a different arrangement of the same proteins on the nanoscale would make such a nonlinear interaction impossible. We use this information to learn more about the organization of muscles on the microscopic level.

Nanoscale systems often contain a limited number of relevant states,[1] and we often want to do something useful with those states, such as operate a motor protein or convert light into electricity. These require highly correlated dynamics that persist in time. Unfortunately, damping by the environment, due to buffeting by solvent molecules, tends to prevent oscillatory dynamics which might be necessary for successful operation of nano-machines or chemical systems. The second law of thermodynamics implies that no macroscopic system may oscillate indefinitely without consuming energy, so dissipation is not surprising *prima facie*. Yet, the maximum number of possible oscillations and the coherent quality of these oscillations remain unknown, until now. The first part of this work proves the upper-bounds on the number and quality of such oscillations when the system in question is homogeneously

[1] An obvious exception to this rule would be living biological systems. They are both nanoscale and have a large number of relevant states, but we try our best to focus on only the most essential parts.

driven and has discrete states. In a closed system, the maximum number of oscillations is bounded by the number of states. In open systems, the system size bounds the quality factor of oscillation, which is a figure of merit for the predictability of recurring behavior. This work also explores how the quality factor of macrostate oscillations, such as would be observed in chemical reactions, are bounded by the smallest loop in the reaction network, not the size of the entire system. The consequences of this limit are explored in the context of chemical clocks and limit cycles. This leads to the analysis of spontaneous oscillations in denatured GFPmut2, where, using these principles, we identify the oscillation mechanism to be the coordinated rearrangement of the hydrogen bond network of the β-barrel. We further calculate that the oscillations are touched off by one of the major loops adjoining the β-barrel, which provide a verifiable means to control the oscillation period.

To optically probe probing nanoscale systems of biological relevance with conventional techniques often requires one to use a focused laser to achieve highest possible signal contrast and resolution. Fluorescent labels in the sample absorb light from the laser and emit a photon with less energy. The detection of the low-energy photon then indicates the presence of the labeled object of interest. Unfortunately, the diffraction limit leads to a fundamental bound of the resolving power of the conventional microscope. To achieve higher resolution, we utilize nonlinear optics to probe the constituent structures of zebrafish muscle. In this case, nonlinearity is a tool for extracting additional information. Because the myosin fibers are asymmetric on the nanoscale, they have the ability to fuse two photons into one, a process known as sec-

ond harmonic generation. Instead of looking for a photon with less energy than the incoming laser, as with fluorescence, we try to detect photons with twice the energy of the incoming light. Second harmonic generation (SHG) based images can be very similar to fluorescence but with up to twice the resolution. Additionally, because light produced via second harmonic generation is coherent, while fluorescence is incoherent, the images have subtle yet significant differences, which we explore and explain. We use the wavelength dependence of the second harmonic generation conversion efficiency to extract information about the microscopic organization of muscle fibers, using the coherent nature of second harmonic generation as an analytical probe.

Second harmonic generation only occurs when the underlying material is asymmetric on the nanometer scale, and this is always the case at the boundary between two different materials. Existing experiments have used technique related to SHG, called sum-frequency generation (SFG), to directly probe the dynamics of free OH bonds at the water-vapor boundary. Using molecular dynamics simulations of the water surface, and by designating surface-sensitive free OH bonds on the water surface, we attempt to computationally reproduce the SFG experiment. The corresponding SFG susceptibility measurements were calculated and compared with those inferred from experiment. The method utilizes results available from independent IR and Raman experiments to obtain some of the needed quantities, rather than calculating them *ab initio*, allowing us to focus on the components of the water dynamics that best capture the observed SFG signature. We determine that the rotational dynamics, with a small quantum correction, are sufficient to produce the observed SFG signal.

The results provide insight into the microscopic dynamics at the air-water interface, and has useful application in the field of on-water catalysis.

To properly establish the path through all of these topics, I note my role in each. The first chapter is work which I have undertaken myself. The research on the GFPmut2 oscillations was directed by Rudy Marcus and advised by Scott Fraser, but the work is primarily my own. The work on zebrafish muscle was a close collaboration with Bill Dempsey, under the direction of Scott Fraser. Bill prepared all of the zebrafish for imaging, injected the morphants, and produced the transgenic fish. I imaged the fish and conducted the computations and theory. The SFG project was directed by Rudy Marcus, and it has since been published [1] and an addendum as been posted with necessary updates.[2] Yanting Wang produced the MD simulations. Yousung Jung and Professor Marcus spearheaded the project. I helped construct the theory with Professor Marcus and process the simulation data. Without this help and guidance from all of these individuals, especially Professors Marcus and Fraser, I certainly would not have much to report, nor would I know nearly as much as I do now.

[2] http://www.rsc.org/suppdata/cp/c0/c0cp02745f/addition.htm

Chapter 2

Oscillations on Networks

To better understand how to build, design, and operate nanoscale machines, we have to understand more about what makes dynamics on the smallest scales different from dynamics we observe in our everyday lives. By dynamics, we refer to the displacements, oscillations, and momentum transformations that give rise to observable behavior. Although popular science is full of interesting discussions of how the world of quantum mechanics leads to wonderful and nonintuitive dynamics, this is only part of the story of why small is different. Classical dynamics, "the science of the 19^{th} century," plays a central role. The reason, in short, is "scaling."

Consider an object in a fluid medium. It is subject to buffeting by molecules of the medium, which deliver kicks that knock the mass off-course, but conservation of momentum also causes the same molecules to sap momentum from any directed motion the body may possess. Newton's law states that $F = ma$, but the total force on the object will be a combination of endogenous forces (which are those forces still acting on the body even in a vacuum) and the buffeting and damping forces from the viscous medium. If the endogenous forces are extensive, meaning they are proportional to the size of the object, they scale as R^3, where R is the effective radius

of the object. In contrast, the fluid medium acts on the surface area of the object, so the forces from the bath causing buffeting and damping scale as R^2. Thus, the ratio of the endogenous forces, which are the forces we would rely on to do useful work, to the bath forces, which impart noise, scale as R. The smaller an object gets, the smaller the endogenous forces become in relation to the bath forces. At a critical length scale, which would depend on the precise forces involved and the nature of the immersion medium, the buffeting and damping by the bath would completely swamp the object's ability to do persistent work. This scaling has been well explored in fluid mechanics via a number of ratios to understand the balance of various factors [2]. Reynolds number, in particular, captures the change in viscous dynamics relative to inertial dynamics as length scales shrink. It is defined as $\mathrm{Re} = VL/\nu$, where V is the velocity of the object, L is a characteristic length scale, and ν is the kinematic viscosity. When Re is small, inertial forces are overwhelmed by viscous forces, and any directed motion is rapidly quenched.

Small objects inherently live in the world of small Re. In the low Reynolds number regime, dynamic motion such as oscillations cannot be sustained. This chapter will explore ways to create oscillatory behavior in the low Reynolds number regime. It has direct application to the design of nanoscale machines and the operation of proteins within the body.

2.1 The Limits of Oscillations in Overdamped Systems

Oscillations are ubiquitous. We celebrate them and attempt to harness them. Naturally, this interest drives us to study them. There has been no shortage of analysis of the simple harmonic oscillator in all of its variations, but much of the periodicity around us is not equivalent to a mass on a spring. For example, the beating heart is driven by molecular motors which exist in the low-Reynolds number regime, where viscous damping overwhelms inertial forces. For these molecular constituents, buffeting by solvent molecules prevents coherent oscillations from persisting on a timescale longer than the mean time between collisions, which is on order picoseconds [3]. Despite this, we observe the coordination of overdamped components to produce periodic behavior [4]. Studying this coordination on a problem-by-problem basis has uncovered some conceptual principles to designing oscillatory behavior in the overdamped regime, but few truly fundamental laws exist [5, 6, 7, 8, 9]. This work bounds the performance of all discrete-state over-damped oscillatory systems, providing a new look at the necessary conditions for creating coherent oscillations in overdamped systems.[1]

When the energy landscape of an overdamped system can be divided into distinct basins of attraction with barriers higher than k_BT, the system will tend to reach a local equilibrium within a basin of the energy landscape before fluctuations stochas-

[1] We all possess an intuitive comfort with oscillations, but we have to formalize this notion for our analysis. To separate coherent oscillations from random fluctuations, we demand that oscillations be predictable and have a characteristic timescale. Predictability implies that the autocorrelation of a signal will have distinct peaks or troughs corresponding to the period of the oscillations.

tically drive it over a barrier into a neighboring basin. Under these conditions, it is common and appropriate to model each basin as a distinct state, with a fixed rate of transitioning from one state to another [10, 11, 12]. These systems are finite state first-order Markov processes[2] and can be modeled by the master equation:

$$\frac{dp_i(t)}{dt} = \sum_{j}^{N} T_{ij} p_j(t) - \sum_{j \neq i}^{N} T_{ij} p_i(t), \tag{2.1}$$

where T_{ij} is the transition rate from state j to state i. For introductions to the master equation and its numerous physical applications see [13, 14]. We will assume that all rates are time-independent, meaning no external factors change the rates (but does not necessarily mean that the system is closed). We also make the assumption that $\mathbf{T}$ is an irreducible matrix, enforcing the trivial condition that we are not modeling multiple mutually isolated systems. Finally, we assume that the systems conserve probability, which can always be enforced by adding states to the system to represent sinks. The solution to eq. (2.1) is $\mathbf{p}(t) = \exp(\mathbf{T}t)\mathbf{p}(0)$, where $\mathbf{T}$ is matrix notation for T_{ij}, $T_{ii} = -\sum_{j \neq i} T_{ji}$ and $\mathbf{p}(t)$ is vector notation for $p_j(t)$ [15]. Systems represented by the master equation are completely described by the transition rate matrix, $\mathbf{T}$, and the initial conditions $\mathbf{p}(0)$. The complete solution is

$$\mathbf{p}(t) = \sum_{j} \mathbf{v}_j e^{\lambda_j t} \left(\mathbf{V}_j^{-1} \cdot \mathbf{p}(0) + a_j(t) \right), \tag{2.2}$$

where $\mathbf{v}_j$ is the j^{th} eigenvector and $\mathbf{V}^{-1}$ is the inverse of the matrix of eigenvec-

[2]This means we exclude systems with high degrees of quantum coherence or those that are underdamped and therefore inertial. The systems in question completely thermalizes before changing states. Without loss of generality, we will only describe the probability of occupying a given state.

tors.[3] Hence, characterizing the properties of $\mathbf{T}$ also characterizes the dynamics of the system [16, 17, 13]. Because the time dynamics of individual modes are ultimately determined by the eigenvalues of $\mathbf{T}$ (see eq. (2.2)), we will be concerned with these eigenvalues and how they relate to oscillations. We first explore these eigenvalues and prove how they constrain the possible oscillations to be fewer than the number of states in the system. Second, I provide examples of these limits by exploring the quality of oscillations in a hypothetical stochastic clock, showing how both microscopic oscillations and macrostates are constrained by the number of states in the system. I conclude by proposing some experiments which may cast direct light onto the physical realization of these bounds on oscillations.

2.2 The Limits on Oscillations

To understand the oscillations in the system represented by $\mathbf{T}$, we consider the relative contributions of different eigenmodes. From the Perron-Frobenius theorem, all eigenvalues of $\mathbf{T}$ have nonpositive real parts, so all but the $\lambda = 0$ equilibrium mode decay away. Eigenvectors with nonzero imaginary eigenvalues oscillate in magnitude as they decay. As we see in eq. (2.2), after a time $(\mathrm{Re}\,\lambda_i)^{-1}$, mode i's contribution to $\mathbf{p}(t)$ will have substantially diminished. If there is an imaginary part to λ_i, before decaying mode i will oscillate $|\mathrm{Im}\,\lambda_i/\mathrm{Re}\,\lambda_i|$ times. Because each oscillatory mode will have a resonance independent of the other modes, the overall quality of oscillations

[3] Dennery, P. & Kryzwicki, A. *Mathematics for Physicists*, Dover 1996.

is given by :

$$\mathcal{Q} = \frac{1}{2} \max_i \left| \mathrm{Im}\, \lambda_i / \mathrm{Re}\, \lambda_i \right| . \tag{2.3}$$

In closed systems, $\mathcal{Q}$ is the upper bound on the number of oscillations. In an open and homogeneously driven system, $\mathcal{Q}$ describes the coherence of those oscillations, in analogy to the quality-factor of harmonic oscillators. This work establishes upper-bounds on $\mathcal{Q}$ by showing the eigenvalues of $\mathbf{T}$ only exist in specific regions of the complex plane.

Karpelevich's Theorem, as clarified by Ito [18, 19], states that all possible eigenvalues of an N-dimensional stochastic matrix with unit spectral radius ($\max_i |\lambda_i| = 1$) are contained in a bounded region, which we call R_N, on the complex plane, shown in figure 2.1. R_N intersects the unit circle at points $\exp(2\pi i a/b)$, where a and b are relatively prime and $0 \leq a < b \leq N$. The curve connecting points $z = e^{2\pi i a_1/b_1}$ and $z = e^{2\pi i a_2/b_2}$ is described by the parametric equation

$$z^{b_2}(z^{b1} - s)^{\lfloor N/b_1 \rfloor} = z^{b_1 \lfloor N/b_1 \rfloor}(1 - s)^{\lfloor N/b_1 \rfloor}, \tag{2.4}$$

where s runs over the interval $[0, 1]$ and $\lfloor x/y \rfloor$ is the integer floor of x/y. For example, the curve that connects $z = 1$, corresponding to $(a_1 = 0,\ b_1 = N)$, with $z = e^{2\pi i/N}$ $(a_2 = 1, b_2 = N)$ is $z(s) = (e^{2\pi i/N} - 1)s + 1$.

The rate matrix from eq. (2.1), $\mathbf{T}$, is not a stochastic matrix. To preserve probability, the sum of each columns of $\mathbf{T}$ is zero, and the diagonal elements are ≤ 0.[4]

[4]This may be obtained by letting $p_i = (1, 0, 0, \dots)$, substituting p_i into eq. (2.1), and solving for the condition $\sum_i p_i = 0$.

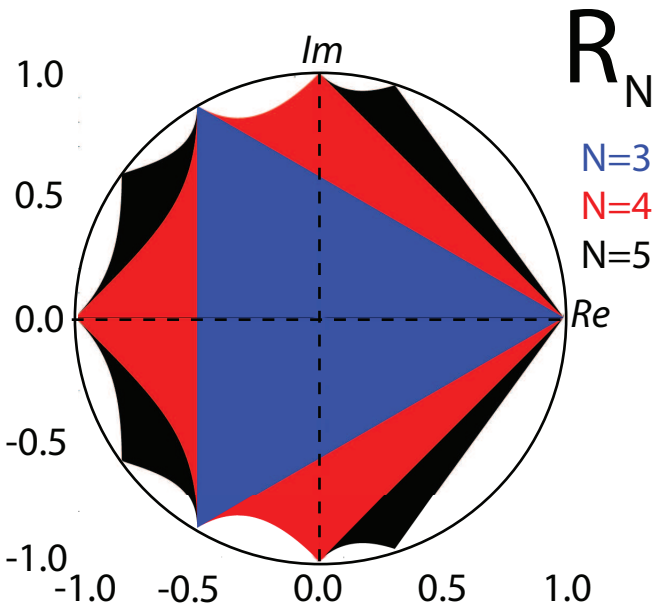

Figure 2.1: The region R_N contains all possible eigenvalues of N-dimensional stochastic matrices with unit spectral radius. Region R_{N+1} contains R_N. This region is symmetric to the real axis and circumscribed by the unit circle. The curves defining each region are given by eq. (2.4), due to Karpelevich's Theorem.

To transform $\mathbf{T}$ into a stochastic matrix, denoted $\mathbf{T}'$, divide $\mathbf{T}$ by the sum of its largest diagonal element and largest eigenvalue, and add the identity matrix. This transformation allows us to write the eigenvalues of $\mathbf{T}'$ in terms of the eigenvalues of $\mathbf{T}$:

$$\lambda_i' = \frac{\lambda_i}{\max_j|\mathbf{T}_{jj}| + \max_j|\lambda_i|} + 1. \tag{2.5}$$

Because the most positive eigenvalues of the original $\mathbf{T}$ are 0 and all others have negative real parts, the most positive eigenvalue of $\mathbf{T}'$ is 1. This unique normalization technique ensures all other eigenvalues are less than 1 and fit within the region R_N on the complex plane. Therefore, all of the eigenvalues of $\mathbf{T}$, will fit within the region $(\max_i|\mathbf{T}_{ii}| + \max_i|\lambda_i|) \times (R_N - 1)$, where these operations on R_N denote scaling and translation, respectively. Within this transformed region, the maximum number of

oscillations will be produced by eigenvalues on the line $\lambda \propto (e^{\pm 2\pi i/N} - 1)$, giving

$$\mathcal{Q}_{\max} = \frac{1}{2}\left|\frac{\sin(2\pi/N)}{\cos(2\pi/N) - 1}\right| = \frac{1}{2}\cot(\pi/N) < \frac{N}{2\pi}. \tag{2.6}$$

We can further refine the limit in eq. (2.6) using a result from Kellogg and Stephens [20], giving

$$\mathcal{Q}_{\max} = \frac{1}{2}\cot\frac{\pi}{\ell_{cyc}} < \frac{\ell_{cyc}}{2\pi}, \tag{2.7}$$

where ℓ_{cyc} is the longest cycle in the system.

Up to this point in our proof, we have restricted ourselves to systems without any degeneracy in the eigenvalues of $\mathbf{T}$. With degeneracy, as shown in eq. (2.2) , the time dependence of eigenvector j may pick up an extra polynomial factor, $a_j(t)$, with degree less than the degeneracy of λ_j, which is always less than $N - 1$. Fortuitous balancing of coefficients could allow a p^{th}-order polynomial to add an additional $p/2$ oscillations. Examining eq. (2.2), we see that the total maximum oscillation quality can be

$$\mathcal{Q}_{\max} < \frac{\ell_{cyc}}{\pi} + \frac{N-1}{2} < N, \tag{2.8}$$

where the second term is strictly due to degeneracy[5]

2.3 Oscillations in Macrostates: Chemical Clocks

Oscillations which consist of cycles on the discrete state-space are only possible when the system in question violates detailed balance [17], which would be the case in a

[5]Such degeneracy will usually emerge only in hypothetical systems where rates balance perfectly.

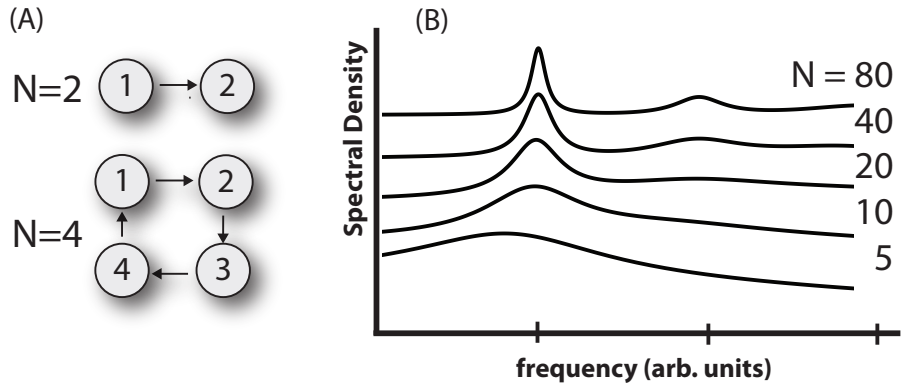

Figure 2.2: (a) When the energy landscape has barriers much larger than k_BT, the system will spend most of its time in the minima of the environment. Approximating the continuous landscape by discrete states gives the familiar master equation kinetics. Here we document two examples of systems with unidirectional transition rates. This cyclical system produces the maximum $\mathcal{Q}$ for any given N. (b) As shown in eq. (2.6), a system with only two states cannot coherently oscillate. It produces only random jumps. As the number of states in the unidirectional cycle increases (in the same family as shown in (a)), oscillations become more coherent and more persistent. The spectral density of the unidirectional cycle shows a distinct peak which becomes sharper as N increases. The transition rates have been normalized by the number of states. The $\mathcal{Q}$ of the systems are, from bottom to top: $0.75, 1.46, 3.09, 6.40, 12.7$, obtained by fitting Lorentzian functions to the peaks.

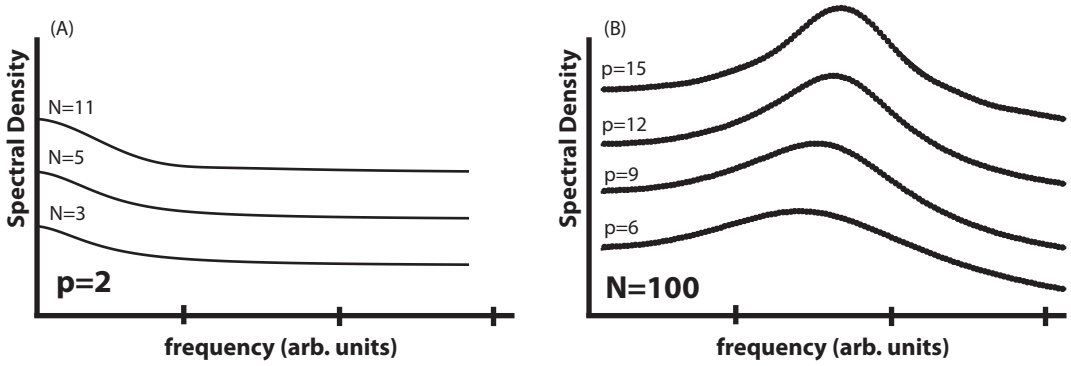

Figure 2.3: Although the linear set of states given by eq. (2.9) does not have any imaginary eigenvalues, macrostates can oscillate. Macrostates are defined as $\langle A \rangle = \sum_i^N A_i^p p_i(t)$. In this case, $A_i^p = \{1 \text{ if } \mathrm{mod}_p i = 0; 0 \text{ otherwise}\}$. (a) Dynamics for different values of N for fixed $p = 2$ (inset) Identical dynamics, but with scaled rates so expected traversal times are the same. (b) Increasing p increases the number and coherence of oscillations given fixed $N = 61$, demonstrating the limit in eq. (2.7).

system which is driven. Otherwise, conservation of energy prevents the system from completing a cycle without encountering significant energy barriers. The microstates of the system, represented by the instantaneous values of $\mathbf{p}(t)$, would not show any oscillatory dynamics or peaks in the spectral density, shown in figure 2.2(a). On the other hand, oscillations in macrostates, which are the linear superpositions $\langle A(t)\rangle = \sum_i A_i p_i(t)$, do not require the underlying microstates to oscillate. The microstate probabilities only need to evolve such that $\langle A(t)\rangle$ oscillates. For example, consider a hypothetical chemical clock[6] described by a cycle of states [22, 10]

$$s_1 \to \cdots \to s_N \to s_1. \tag{2.9}$$

If the clock advances each time the cycle is traversed, adding states to the cycle improves the quality of the clock, as shown in Fig 2.2(b). A more abstract implementation could be to consider a clock cycle and a fuel reservoir. We define that the clock consumes 1 unit of fuel during the transition from s_N back to s_1, so the cycle is an open system. This accounting method, in effect, unrolls the cycle into a linear chain of microstates enumerated by the dyad $\{f, s_i\}$, where f is the amount of fuel remaining. When f is effectively infinite, the dynamics of the open cycle and the linear chain are equivalent. As the system moves from one state to another, we count time by keeping track of the evolution of the macrostate denoted $A(t)$. The macrostate of the clock is $\langle A(t)\rangle = \sum_{i,f} A_i p(f, s_i, t) = \sum_i A_i \langle p(s_i, t)\rangle$. Therefore, the quality of oscillations in

[6]The oscillating chemical clock is distinct from the traditional "clock reaction," where an autocatalytic reaction causes a sudden one-time change in state on a distinct timescale, such as the iodate-bisulphite system [21].

the infinite linear chain is bounded by $\mathcal{Q}_s$, regardless of the precise amount of fuel. When $A_i = \{1 \text{ if } \mathrm{mod}_2 i = 0; 0 \text{ otherwise}\}$, as shown in figure 2.3(a), the total number of states, N does not effect the quality of the clock. However, if we change A_i to

$$A_i^p = \{1 \text{ if } \mathrm{mod}_p i = 0;\ 0 \text{ otherwise}\},$$

figure 2.3(b) shows increasing oscillation in $\langle A(t) \rangle$ with increasing p. That is, adding more states to the clock directly increases its accuracy.

Texts exploring chemical oscillations state that nonlinearity is a requirement for oscillations. In fact, nonlinearity is a shorthand for describing extremely large systems [13]. Under conditions of detailed balance, systems must consume some sort of fuel to sustain oscillations. If we consider the fuel-free states as being an abstract engine with N states, the combined engine-fuel system will be in one of the N different states and have f units of fuel remaining. Therefore, a fuel reservoir can allow a total number of oscillations $\approx fN/\pi$. eq. (2.8) implies that the number of inherently unique states, absent fuel consumption, will constrain the possible regularity of reciprocal motion [10]. Thus, the quality of oscillations appears to be bounded by the smallest irreducible cycle in the system, although this is not proven. That is, the topology of the network is inherently related to the ability of the system to sustain oscillations, and this will be explored in future work.

Similarly, if the system is driven by oscillations in multiple parameters or species, we can again parameterize the state of the system based on the population of each component. However, most chemical dynamics are modeled using continuous vari-

ables, not discrete numbers of states. The microscopic description of the system, comprised of a discrete number of states, is connected to the continuous mass-action approximation of chemical dynamics by a system size expansion described by Van Kampen [13]. Take, as an example, the multidimensional oscillating chemical reaction called the Brusselator. By expanding the mass-action Brusselator into a discrete state-space, the system size-expansion parameter determines the length of the largest cycle [23, 24]. Indeed, multiple authors have observed that the quality of the Brusselator limit cycle scales with system size, consistent with this work [23, 22, 25, 26, 27, 24]. This observation is not merely coincidence, but a fundamental efficiency limit of the master equation.

This efficiency limit of oscillations has obvious implications on how well a high-dimensional system can be numerically approximated by a smaller system. The approximation will only be successful if the relevant eigenvalues of the larger system lie within the allowed region of the smaller system. However, the inverse stochastic eigenvalue problem has not yet been solved, so we cannot know *a priori* if a stochastic matrix exists for a given set of eigenvalues, even if they all reside within the allowed region [28]. This fact prevents us from constructing the opposite bounds, the conditions for a *minimum* number of oscillations. Hopefully, future results will further constrain the present bounds, and we may gain deeper insight into the necessary conditions for creating oscillations.

The bounds on oscillations can play a key role in interpreting experimental observations by determining a minimum number of underlying states. For example,

the oscillation of fluorescence wavelength in fluorescent protein GFPmut2 remains unexplained [29, 30, 31]. After application of a denaturant, the ionic state of the fluorophore can switch up to $\mathcal{Q} \sim 50$ times with high regularity, observed as oscillations in the emission wavelength [29]. Because eq. (2.7) bounds the number of states involved in the oscillation to be at least 3 times larger than $\mathcal{Q}$, this predicts that the oscillations are driven by large-scale rearrangement of the numerous hydrogen bonds in the β-barrel, not merely exchange between the few amino acids directly connected to the fluorophore. If the protein were to be mutated to alter the number of bonds in the β-barrel, we predict that we should see a corresponding alteration in the number and quality of observed oscillations.

2.4 Oscillations in Green Fluorescent Protein GFPmut2

In a series of recent experiments, a mutant of Green Fluorescent Protein, GFPmut2, was encapsulated in silica gel and observed under denaturing conditions [32, 33, 31]. Ordinarily, when folded or even during unfolding, GFPmut2 is stable in the anionic green state, with stochastic transitions to the neutral blue state. At the very end of the denaturing process, just prior to complete fluorescence quenching, the fluorescence oscillates between green and blue [33]. This resonant oscillation is unique in fluorescence behavior and unobserved in single-protein dynamics except for the slow oscillations in activity of the ECTO-NOX protein [34, 35]. In addition to being

a fascinating window into denaturing dynamics, the observed GFPmut2 oscillations prompt the question of how a single molecule can be driven to autonomously oscillate.

Although the GFPmut2 oscillations are fascinating, they have not been fully explored experimentally. Although further experiments could cast new light onto this unique dynamics, the current body of work suggests these oscillations are autonomous, meaning that no laser or mechanical driving occurs. Somehow oscillations spontaneously emerge late in the denaturing process, and they persist far longer than the picosecond timescale of natural underdamped motion in protein bonds [36]. No other groups have reported independent observation of fluorescence observations from GFPmut2 as of early 2011, although we have tried, both at Caltech, and with the help of Jau Tang at Academia Sinica. The largest hurdle has been avoiding photobleaching. Additional experimental evidence will of course further inform the accuracy of the results below.

Because the oscillations take place on the millisecond timescale, and they do not begin for up to an hour after denaturing starts, MD simulation is impossible. Thus, there is no hope of brute force replication of the experiment *in silico*. Furthermore, the oscillations are only apparent on the single molecule level, so NMR cannot directly access the chain of events. We are left with an approach where modeling can suggest new experimental variables and observables to probe.

The timescale of oscillation in GFPmut2 is too long to be attributed to most normal processes associated with protein dynamics, including bond vibrations, torsional modes, and isolated residue rotation [37]. For example, in wildtype GFP, Agmon

has observed that the stochastic blinking in wildtype GFP is due to the rotation of Thr204, but it characterized by a switching time of tens of nanoseconds [38]. Most protein dynamics on the millisecond timescale are characterized as two-step processes, indicating only a single degree of freedom dominates the folding process. However, Langevin dynamics indicate that self-sustained oscillations in a single degree of freedom in a protein would be impossible. In fact, a single degree of freedom cannot produce any oscillations at all without some external driving, as demonstrated in the section 2.2.

Given that the oscillations in GFPmut2 are not associated with any known periodic driving, there must be some coordinated interplay between ordinarily unobservable degrees of freedom. Even the nature of the experiment suggests this, because the fluctuation of any single hydrogen bond normally cannot be observed via the fluorescence of the molecule. The denaturants used, urea and guanidinium HCl, attack the barrel in slightly different ways [39, 40, 41], but the resulting oscillations are identical [42]. The fluorescence photophysics does not deviate from normal throughout the vast majority of the denaturing process, except for the moments before quenching. Because the fluorescence oscillates between anionic and neutral up to 20 times [33], there must be at least 120 separate internal states coordinating the oscillations. The only source of this many states within a single protein would be the hydrogen bonds of the β-barrel. Somehow, the denaturant sets off a cascade of hydrogen bond breaking and reforming that is observed in the experiment as the ionization state of the fluorophore. There is evidence that the oscillations are not due to rearrangements of

precise bond networks, because these networks are sensitive to salt concentrations. Protonation rates vary continuously with GdnHCl, but we do not see oscillation periods vary [43].

Here, we explore our hypothesis of hydrogen bond fluctuations by suggesting a two variable system where the ionic state of the chromophore alters the stability of the β-barrel. Without a direct crystal structure of GFPmut2, we cannot know if there are unique structural features in GFPmut2 to focus on as a starting point. However, we can draw analogies from other GFP mutants, such as S65T [44]. All mutants in the green fluorescent protein family fold into the distinctive β-barrel conformation, shown in figure 2.4. The β-barrel is held tightly closed by dense array of hydrogen bonds running up and down the sides of the barrel. This protects the chromophore, shown in figure 2.5, which is quenched by water.

By considering these facts, we attempt to synthesize a model to increase our understanding of this system.

2.4.1 Limit Cycles

Long term dynamics in closed systems are always driven to equilibrium. This stable state quenches any oscillations, leading to what Lord Kelvin profoundly called "Heat Death," where no more free energy is available to sustain nonstochastic motion [50]. In the case of GFPmut2, we observe this as the fully denatured state where all fluorescence is quenched. Prior to oscillations, and toward the end of the series of oscillations, the ionization state of the fluorophore is stochastic. Only during a brief

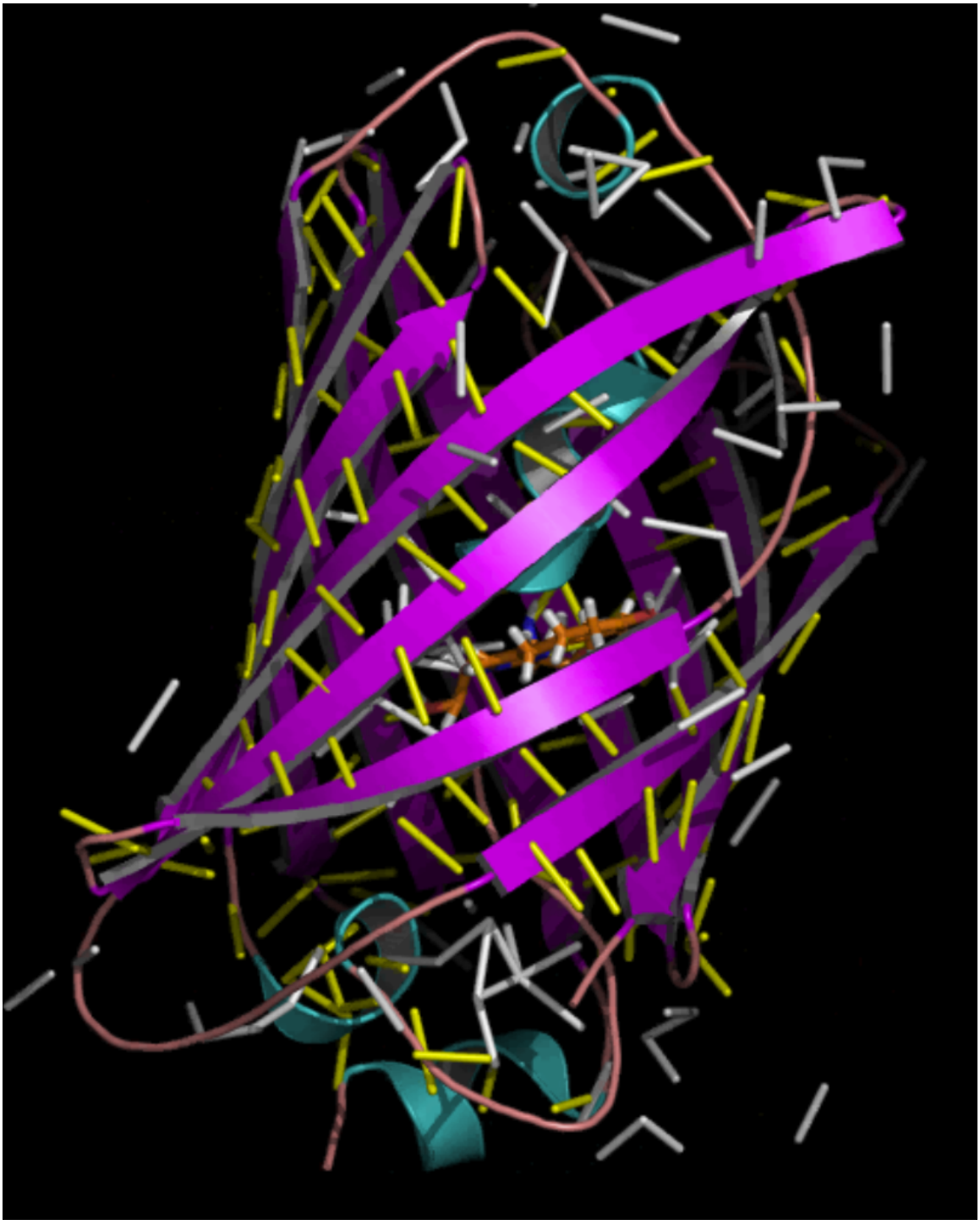

Figure 2.4: Ribbon representation of GFP, made using PyMol [45]. The β-barrel is colored purple. Unstructured regions are pink. α-helix loops are colored blue. White and yellow rods are hydrogen bonds between residues, which are not shown. The chromophore is orang, and can been seen edge-on. Original model was PDB entry 2HPW [46, 47, 48].

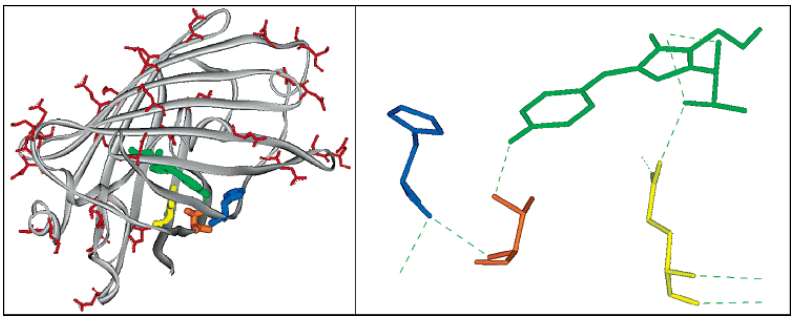

Figure 1. (Left) Three-dimensional structure of S65T GFP at pH 8 (PDB entry 1EMG). The chromophore is shown in green, His148, in blue, Thr203, in orange, and Glu222, in yellow. The carboxylic acids present on the protein are shown in red. (Right.) Closeup of the chromophore with the mutated residues.

Figure 2.5: The chromophore is in green, shown in the center of the β-barrel in left, and in its native H-bond arrangement in the right. Taken from [49].

sub-100 ms window does the ionization state oscillate somewhat deterministically.

A proton determining the ionic state of the chromophore is transported to and from the fluorescent ligand via proton channels determined by the orientation of amino acids in the binding pocket and the barrel. Proton channels transport protons on a picosecond timescale, similar to other breathing modes of amino acids. Therefore, these local vibrations and rotations average out over the course of an oscillation. Large scale rearrangements of the hydrogen bond network are much slower. These "proteinquakes" transpire over milliseconds, the same timescale as the oscillation dynamics [51, 52].

Matching timescales indicates that the oscillations could be dominated by two parameters, the ionization of the fluorophore and a proxy for the number of hydrogen bonds holding the protein together. Because the proton traverses proton-wires that open and close via rotational modes of amino acids along the wire [53], the proton's position will be stochastic over the experimental timescale. We therefore wish to calculate the time-dependent probability of the proton being on the fluorophore (an-

ionic), $p_A(t)$, as a function of a chemical coordinate of hydrogen bonds D, which shall act as our proxy measure of the hydrogen bond network.

The internal charge distribution can determine the stable configuration of the hydrogen bond network, as was also seen in [53]. After exposure to denaturants for some time, a number of stabilizing hydrogen bonds break down, and denaturant begins to penetrate into the internal binding cavity [54]. After sufficient time, the entire β-barrel is broken from the inside-out, leading to a general two-state picture for denaturing. The precise chain of events during the unfolding process may depend on the employed denaturant [39], but the resulting oscillation dynamics do not appear to have any such dependency [31].

Because the observed persistent oscillations are so unusual, we first attempt to find conditions for totally self-sustained oscillations, i.e.,a limit cycle. If one assumes that the internal charge distribution alters the local equilibrium of the hydrogen bond network, and that the internal charge distribution is reported through the ionic state of the fluorophore, the dynamical equation describing their interdependence must take the general form:

$$\dot{p}_A(t) = - f_1(D)p_A(t) + f_2(D)(1 - p_A(t)) \tag{2.10a}$$

$$\dot{D}(t) = g_1(D)p_A(t) + g_2(D)(1 - p_A(t)). \tag{2.10b}$$

Oscillations would be indicated by $p_A(t)$ swinging between 0 to 1 and back on a fixed timescale, representing near certainty of the fluorophore being neutral and anionic, respectively, and then returning. We see that Eq (2.10a) has the form of a

Fokker-Planck equation, while eq. (2.10b) describes the ensemble average dynamics of D. Because eq. (2.10a) is a master equation, detailed balance would suggest f_1 and f_2 to be

$$f_1(D) = k_1 e^{-D/d_0}$$

$$f_2(D) = k_2 e^{D/d_0}.$$

This functional form indicates that the parameter D is affine in the free energy of the protein. It is also consistent with experimentally observed reprotonation rates in GFP as a function of denaturant concentration [43]. When in the anionic state, the charged state favors D growing, consistent with denaturing occuring spontaneously. In the neutral state, small D becomes unfavorable. Hence, the free energy difference between the anionic and neutral states would be $\Delta G = \ln(k_1/k_2) - 2D/d_0$. Research by Saxena et al. has shown that the deprotonation process in native EGFP, a mutant similar to GFPmut2, in nearly barrierless (0.3 kcal/mol), while the reprotonation has an activation energy of 14.8 kcal/mol [43]. Thus, we posit that denaturation alters the free energy balance between the two states, ultimately determining the charge state of the chromophore.

We use eq. (2.10b) to describe the ensemble average of $D(t)$, making g_1 and g_2 the recruitment rate of newly denatured bonds in the anionic and neutral state, respectively. When the protein is well folded, denaturant attacks bonds and opens up the barrel, disrupting cooperative folding. If the state of the chromophore directly or indirectly determines the local equilibrium fold, denaturant may be squeezed out of

the β-barrel under certain conditions. We take

$$g_1(D) = k_3 D$$
$$g_2(D) = -k_4 \frac{D}{k_5 + D}.$$

That is, under the anionic state, hydrogen bonds decay as a first order process. Upon the transition from neutral to the anionic charge state, the fold is now no longer in equilibrium, so the protein undergoes a proteinquake [51]. In the neutral state, the equilibrium structure is one that catalyzes reforming of hydrogen bonds and restabilizing the barrel, leading to a Michaelis-Menten expression due to neighboring amino acids effectively catalyzing bonds with their neighbors. In the neutral state, amino acids no longer have the central anion competing with the other amino acids for preferential alignment due to the anion-induced dipole coupling, diagrammed in figure 2.6. In total, Eqs. (2.10a) and (2.10b) become

$$\dot{p}_A(t) = -k_1 e^{\frac{D}{d_0}} p_A(t) + k_2 e^{-\frac{D}{d_0}} (1 - p_A(t)) \tag{2.11a}$$
$$\dot{D}(t) = k_3 D p_A(t) - k_4 \frac{D}{k_5 + D} (1 - p_A(t)). \tag{2.11b}$$

With a model of this form, we successfully produce oscillations in both charge state. p_A. and structural stability, D. Tools such as Mathematica's EquationTrekker allow a rapid visual search of parameter space. figure 2.7 shows a typical set of phase-space trajectories produced from one combination of parameters, showing that sustained oscillations can be readily produced when the two charge states favor two

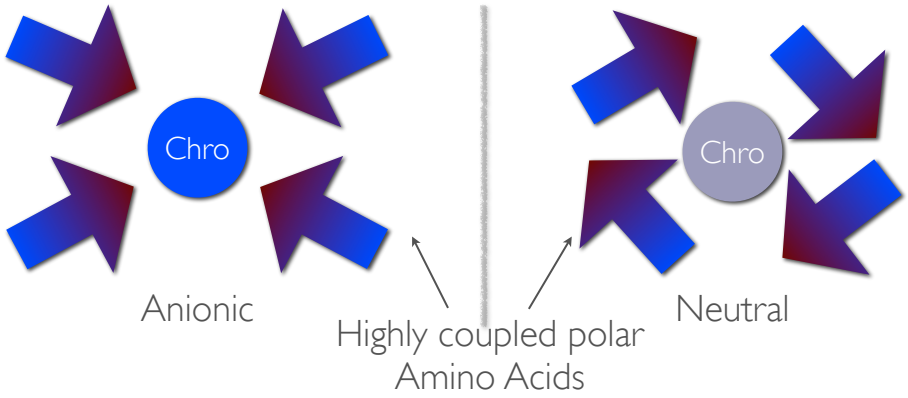

Figure 2.6: When the chromophore is anionic, left, its excess charge draws its tightly coupled neighbors into alignment with the chromophore. When neutral, the amino acids are now free to preferentially align with their neighbors, increasing the structural rigidity of the β-barrel.

different folds, as hypothesized. figure 2.7 shows the GFP oscillating between p_A between approximately 0.9 and 0.1, corresponding to a 90% probability of being in the anionic state when highly structured (D small). The anionic state allows denaturing, and p_A swings to 0.1 as D increases, ultimately reaching a 90% chance of being in the neutral state.

Because eq. (2.11) produce limit cycles, these equations suggest a mechanism for the dynamics. However, limit cycles that produces the desired oscillations cannot explain the complete dynamics of GFPmut2, because no system can oscillate indefinitely. The key assumption is that the energy of the protein spontaneously increases when the charge state flips, favoring a more robust (or delicate) fold. Although it would not be unusual for an internal degree of freedom to shift the energy landscape [52], a physically motivated description of the protein dynamics could not produce indefinite oscillations. Furthermore, GFPmut2 oscillations do not appear

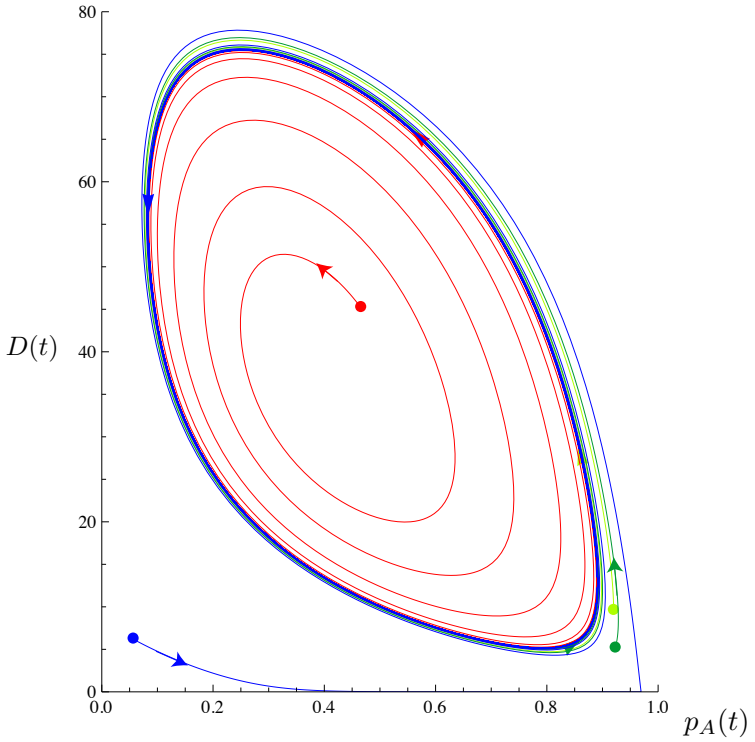

Figure 2.7: Given the parameters $d_0 \to 19.0, k_1 \to 0.12, k_2 \to 3.8, k_3 \to 4.8, k_4 \to 124.0, k_5 \to 1.6$, eq. (2.11) shows that the expected charge state of the chromophore can develop strong oscillations. These parameters are not physically determined, but indicate that the functional form of eq. (2.10) likely corresponds to some underlying dynamics.

the instant denaturant is applied. It can take an hour of denaturing before any oscillations are observed [30, 31]. Our model should be able to suggest an explanation for this as well as predict a finite resolution to the oscillations. To address this, we consider more closely the dynamics of our model system and how the limit cycle forms from eq. (2.11).

Consider the nullclines of the dynamics described by eq. (2.11), which are determined by fixing $\dot{p}_A = 0$ or $\dot{D} = 0$. Each condition will give a different curve, corresponding to the path in phase-space which satisfies each condition. Both curves

can be written as a function of $D(p_A)$:

$$D(p_A) = \frac{d_0}{2} \log\left(\frac{k_2}{k_1}\frac{1-p_A}{p_A}\right) \qquad \dot{p}_A = 0 \tag{2.12a}$$

$$D(p_A) = \frac{k_4}{k_3}\frac{1}{p_A} - \frac{k_4}{k_3} - k_5 \qquad \dot{D} = 0. \tag{2.12b}$$

The mutual intersections of the nullclines determines the character of the phase-space dynamics, as shown in Fig 2.4.1. Altering any of the rates adjusts the position of the nullclines, such that they do not intersect (figure 2.8(a)), intersect once (figure 2.8(b)), or intersect twice (figure 2.8(c)). A limit cycle only emerges when these nullclines intersect at one point. In fact, altering only a single rate, k_3, is sufficient to drive the system from a stable fixed point into a limit cycle by altering the position of the $\dot{D} = 0$ nullcline.

If the rate k_3 were time dependent such that k_3 started small at $t = 0$ and grew monotonically larger over time, the system would initially exhibit the experimentally observed nonoscillatory behavior until k_3 reached a critical value (which is dependent on all other parameters in a nontrivial way). The curves would first intersect twice, as shown in figure 2.8(c). The phase-space dynamics still display a single stable node, but the system entering the unset of instability. This is consistent with the experimentally observed steady increase in the blinking rate in the minutes leading up to the onset of GFPmut2 oscillations [30]. Once k_3 grows a bit large, the nullclines then intersect only once, causing the system to bifurcate into a limit-cycle, corresponding to the experimentally observed oscillations. As k_3 continues to increase, eq. (2.12b) shows the D nullcline monotonically shifts towards the $p_A = 0$ axis. The center of the limit

cycle shifts toward this axis, as well. As a result, the dynamics are shifted to favor the $p_A = 0$ state. As the center of the limit cycle drifts to $p_A = 0$, the probability of returning to the anionic state decreases, and the oscillations begin to look like chaotic blinking, as has been observed [33]. This entire series of events are played out in figure 2.9 by assuming an exponential time dependence for k_3.

What could produce such a time dependence? The GFPmut2 chromophore is tightly coupled to a handful of neighboring amino acids, as shown in figure 2.5. These amino acids coordinate the local field and help determine the equilibrium ionization state of the chromophore, which has been found to have a pKa of 6.2 [55]. However, the amino acids most tightly coupled with the chromophore are also held in place by hydrogen bonds from their neighbors, and so on. As the bonds start to break up, fluctuations in the local pKa grow in proportion to the degree of stabilization. The loss of mutual stabilization increases local fluctuations in the β-barrel, and the amino acids take larger excursions from their local equilibria. This in turn allows the denaturant better access to further destabilize bonds, resulting in a denaturing rate that increases with time. Therefore, k_3 may have some dependence on additional degrees of freedom, approximated to first order by an exponential growing function of time.

2.4.2 Loop Dynamics

Although the limit-cycle model in the previous section established that the denaturing increases as the oscillations evolve, it used a continuous variable, $D(t)$, not the number

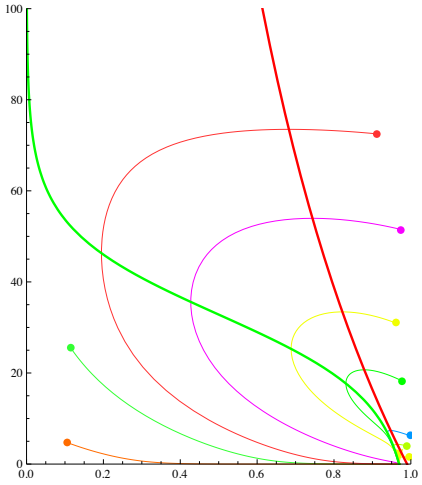

(a) $k_3 \to 0.8$, one fixed point: nullclines do not intersect

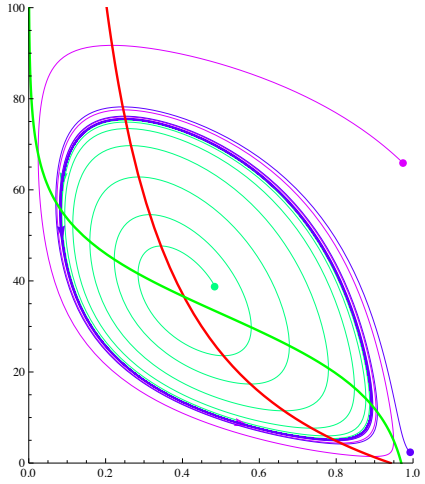

(b) $k_3 \to 4.8$, limit cycle: nullclines intersect once

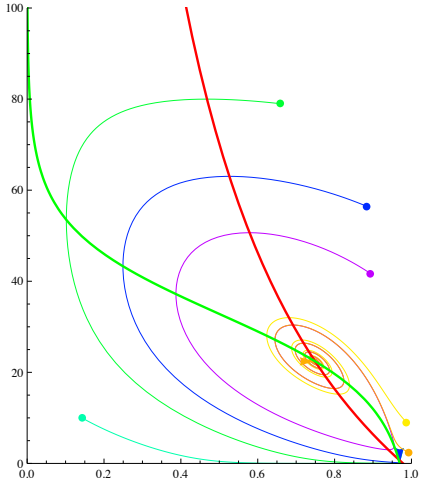

(c) $k_3 \to 1.7$, one stable spiral and one unstable: nullclines intersect twice

Figure 2.8: Green curve: $p_A(t) = 0$ nullcline; Red curve: $D(t) = 0$ nullcline. Above the green curve, $\dot{p}_A < 0$ and below $\dot{p}_A > 0$. Above the red curve, $\dot{D} > 0$, and below $\dot{D} < 0$. $d_0 \to 19.0, k1 \to 0.12, k2 \to 3.8, k4 \to 124, k5 \to 1.6$

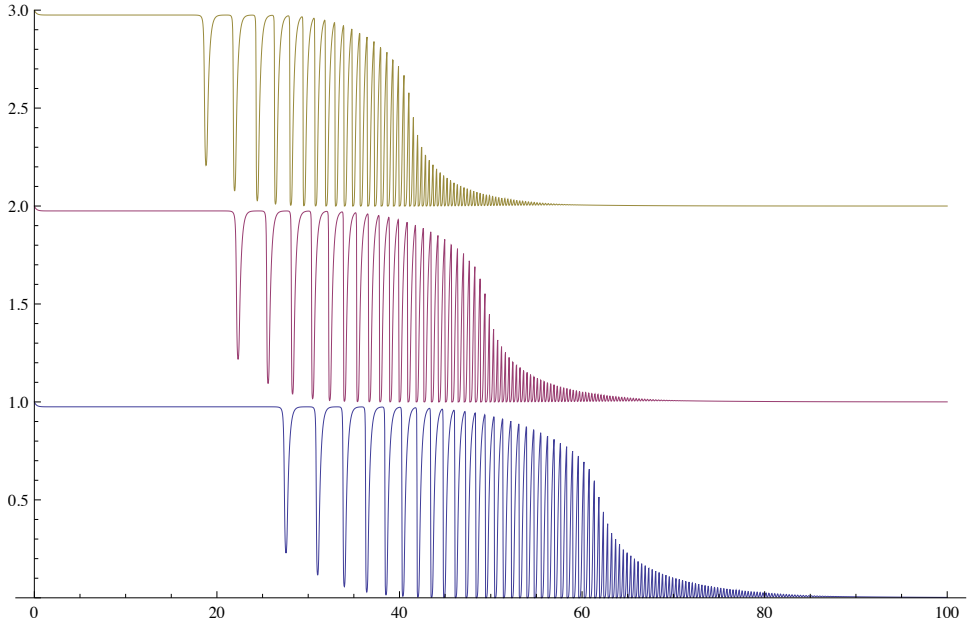

Figure 2.9: Time-dependent rates create a transition from a static system to a limit cycle. In this case, we transform $k_3 \to k_3 e^{k_6 t}$. k_6 is different between the three plots. top: $k_6 \to 0.12$, middle: $k_6 \to 0.10$, and bottom: $k_6 \to 0.08$. Each range runs from $p_A = [0, 1]$ versus time, and the curves are offset for clarity.
$d_0 \to 5.29, k_1 \to 0.11, k_2 \to 4.29, k_3 \to 1.0, k_4 \to 177.18, k_5 \to 1.34$.

of hydrogen bonds. This allowed for better examination of the dynamics, but does not explain the how the bonds break. The speed of bond breakage determines rate of increase in $D(t)$, and thus, also determines the oscillation rate, because a faster change in D directly translates into a faster change in p_A, the observed fluorescent state. We also postulated that the central destabilizing force was a collective breakdown in the mutually stabilizing hydrogen bond network, leading to a time dependent k_3. What determines the precise value of k_3? This may only be hypothesized, but a consideration of the GFP crystal structure shows the β-barrel to be remarkably uniform, with no obvious lines of weakness in the arrangement of hydrogen bonds. However, the β-barrel is constructed by looping the backbone to reach the final fold. Three loops are needed to properly fold GFP, as shown in figure 2.10. Loops are

entropically unfavorable [56], acting like springs pulling on the β-barrel [57, 58].

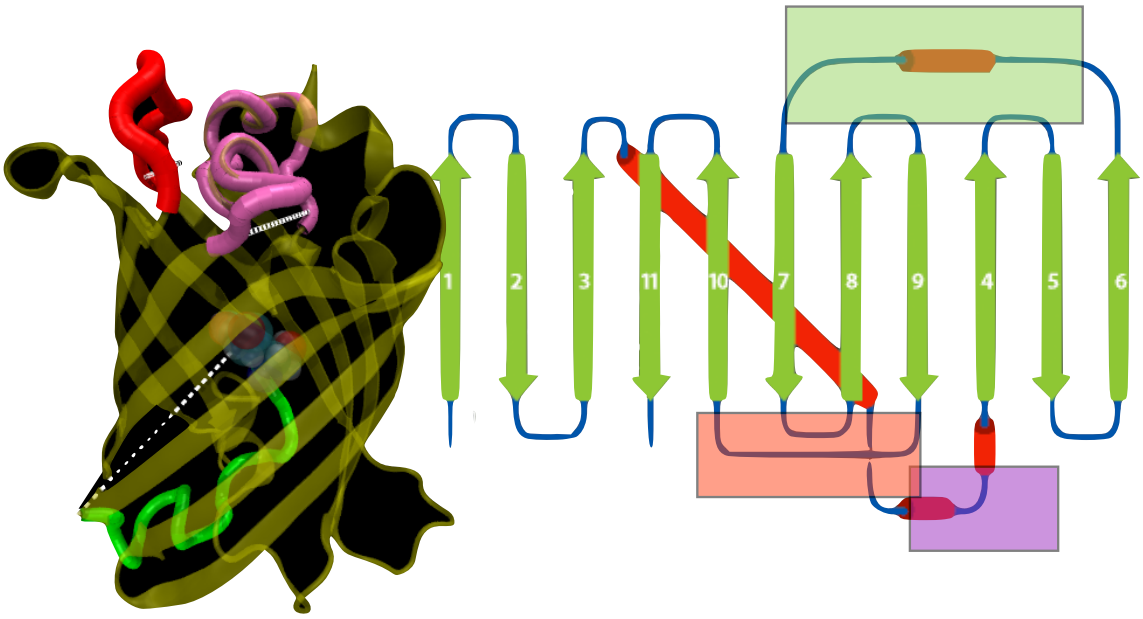

Figure 2.10: left: 3D representation of GFP, with backbone colored yellow. The three loops are colored red, purple, and green. Dotted white lines indicate the distance from the start to end of the loop. right: depiction of the secondary structure of GFP, with strands of the β-barrel numbered $1 - 11$. The loops are the red cylinders, and colored red, purple, and green to correspond to the 3D image on the left.

Because of the large damping, the collisions between the loops and the bath molecules cause the loop to rapidly explore its configuration space, subject to the constraints of its end-to-end distance. This results in an entropic force being exerted on the amino acids at the ends of the loop. Loops are analogous to a spring under tension [59]. Of course, under native conditions the loops have little or no effect on the extremely stabile β-barrel. Over the course of the denaturing process, the loops will eventually dominate the weakened hydrogen bond network and begin to pull apart the β-barrel.

Because of the denaturant, the α-helices in the loops will break down, and there will be very little structure in the loops. This allows the loop to be modeled as

a wormlike chain (WLC)[60, 61, 57], a model defined by the correlation relation $\langle \hat{r}(s) \cdot \hat{r}(s + \Delta s) \rangle = \exp(-\Delta s/p)$, where $\hat{r}(s)$ is the orientation vector of polymer a distance s from the end, and p is called the persistence length. This model works well for short loops of amino acids [62], and under the WLC model, the entropic force is a function of end-to-end distance is given by

$$F(R) = \frac{k_b T}{p} \left(\frac{1}{4}(1 - \frac{R}{N\ell})^{-2} - \frac{1}{4} + \frac{R}{N\ell} \right), \tag{2.13}$$

where R is the end-to-end distance, p is the persistence length, N is the number of amino acids, and ℓ is the effective loop length contribution of each amino acid. Although the loops pulls continuously, the bonds break discretely and regularly. How does one map a continuous linear transduction into a periodic signal?

Consider a common baby's toy, the bead maze, shown in Fig 2.11. Even if a train of beads are moved over the apex of the curve at a continuous rate, only one falls over at a time.[7] If the bead train is moved at constant velocity, v, the time between beads moving over the apex is ℓ/v, where ℓ is the length of the bead. Hence, the audible "click" produced when the beads collide at the bottom has a period of ℓ/v seconds. Linear motion has been transformed into a periodic signal.

Analogously, the drag and damping by the water cause the loop to move without any inertia, leaving a Stokes drag condition, $F(R) = \eta v$, where η is the drag

[7]Because there is no coupling between beads, the bead that is balanced on the apex has an adjacent bead one bead-width, ℓ, lower on the wire track. The bead at the apex becomes unstable and slides over the top, but the adjacent bead must move another ℓ before it reaches the apex and slides over. This takes a time ℓ/v.

coefficient.[8] Under denaturing conditions, the weakened β-barrel is able to be deformed by the loop, pulling the amino acid adjacent to the loop at a constant velocity $v = F(R)/\eta$, and the expected time for the amino acids to be pulled out of their hydrogen bonds with their neighbors is $\tau = F(R)/\eta\ell$. We observe three different loops in figure 2.10, with the following pairs of parameters, $(N, R) = (17, 2.1 \text{ nm}),\ (11, 1.7 \text{ nm}),$ and $(8, 1.7 \text{ nm})$. Based on force-induced denaturing experiments, we have $p = \ell = 0.39$ nm [62]. It is reasonable to assume that any one of the three loops may dominate the final unfolding during a single unfolding cycle, and the resulting oscillation dynamics will depend on that particular driving force, just as a single fracture dominates the initial failure of a brittle object. Experiments observe that GFPmut2 oscillates with one of three frequencies: 930, 720, or 440 s^{-1}. The same protein will oscillate at only one frequency during one unfolding cycle, but it may oscillate at a different frequency during subsequent cycles. Even though we do not know η, the resulting calculated ratios of oscillation rates, 1:0.72:0.41, are in good agreement compared to the experimentally observed ratios, 1:0.72:0.47 [30].

This agreement provides a key insight into the dynamics of GFPmut2 unfolding. If the preceding analysis holds, the unfolding dynamics appear to be primed by the destabilization of the loops in a systematic way. The loops deform the β-barrel, popping out hydrogen bonds one-by-one. As discussed in the previous section, the charge state of the chromophore helps to coordinate the surrounding amino acids in such a way as to loosen the β-barrel sufficiently to allow the loop dynamics to

[8] The drag coefficient η will be a function both of the drag due to moving through the water and the energy absorbed by distortions of the β-barrel, making a calculation of η beyond the scope of the present work.

Figure 2.11: The bead maze, a common children's toy, is an example of linear motion producing a periodic signal. As baby Leo pushes the train of beads over the top of a loop, one bead at a time slides down the other side as it passes the apex. Although Leo moves the beads at a constant velocity, v, he hears a periodic click of frequency v/ℓ as each bead slides to the bottom, where ℓ is the length of the bead.

dominate, but the neutral state strengthens the barrel, neutralizing the effect of the loops. This analysis predicts the oscillation rates are determined by the loop lengths. If experiments are able to observe the oscillations in fluorescence, altering the loop lengths should change the ratio of oscillation rates in systematic way, confirming the present predictions.

2.5 Conclusion

We have examined how system size relates to the dynamic behavior of overdamped systems. Because most systems on the nanoscale operate at very low Reynolds number, they satisfy this condition. When those states are enumerable, systems with more states have the ability to oscillate longer and more coherently. This carries

implications not only for designing nanoscale systems, but also the results apply to any system that may be described as dynamics on a network, such as social networks. The quality bounds proved here are universal. Because the master equation is used in nearly every branch of science, the dynamics being modeled need not be physical. For example, it could be money held by a bank [8], packets of data on the internet [63], agents traversing a network [64], or the populations in an ecosystem [65]. The oscillation limit could also be probed experimentally with sculpted landscapes using optical tweezers [66]. As a probe bead jumps from trap to trap, the energy landscape in unoccupied traps is sculpted to simulate an arbitrarily large designer network of discrete states. The current results are a fresh approach to analyzing the dynamics of discrete systems, and it serves as a new design principle for those seeking to engineer oscillations.

This theorem also has direct application to explaining the curious dynamic of GFPmut2 oscillations. Using the theorem, we were able to construct a model based on the rearrangement of hydrogen bonds in the β-barrel, as opposed to oscillations in the dynamic conditions around the protein or in the underdamped motion of protons. Using a two component model to track the probability of ionization of the chromophore and degree of denaturing of the β-barrel, we are able to analyze how the oscillations emerge and why they dissipate. Further phase-space analysis predicts a cooperative effect maintains the β-barrel. Once the barrel begins to fully destabilize, the denaturing occurs rapidly, and the barrel's ability to repair itself degrades until finally the protein is fully denatured. We hypothesize that the loops of the GFP have a central

role in determining the rate of unfolding due to their destabilizing nature, and an experiment which alters the length of these loops should see a corresponding change in the oscillation time.

This chapter has shown how linear state spaces may be mapped into nonlinear systems, allowing us to better understand oscillations on the nanoscale. Further work will be able to refine both parts of the work in this chapter. First, identifying motifs that give rise to oscillations or other chaotic behavior in reaction networks will uncover more applications for the theorem. Second, connecting the predicted consequences of GFP oscillations with further experimental observations may provide more evidence to refine our understanding of the oscillations. The next chapter will explore how optical nonlinearity, instead of nonlinearity in state-space, may be used to probe the geometry of proteins inside muscle using nonlinear optics, extracting more information than possible using traditional fluorescence techniques.

Chapter 3

Endogenous Second Harmonic Generation in Zebrafish

One emerging technique for biological imaging is harnessing nonlinear optics to probe endogenous structures [67, 68, 69, 70, 71, 72, 73, 74, 75, 76]. The vast majority of an organism is constituted of proteins and water. Water has an index of refraction of 1.33, while tissue has an index of approximately 1.4 [77, 78, 79]. The makes living tissue nearly optically continuous, compared to the optical contrast between tissue and gold, for instance. How does one then optically study objects of interest in such a low-contrast environment? Of course, the most common approach to selective imaging is to introduce something to enhance this contrast, such as a stain or fluorescent dye. Fluorescent dye, in particular, allows for exceptional contrast, because the only source of light at the desired wavelength will be from dye and low-level natural endogenous autofluorescence. However, the natural chirality of proteins can serve as a source of second harmonic generation, allowing us to distinguish highly ordered structures from the amorphous background without introducing any foreign components. That is, only certain structures will transform two photons from the input laser into one

photon at half the wavelength. Detecting the SHG wavelength will then allow for localization of the source structures. For example, the ordered arrangement of muscles and collagen serve as particularly bright sources of biological SHG, shown in figure 3.1 for the case of muscle. There are also a number of studies of SHG and hyper-Rayleigh scattering from films and suspensions of proteins and DNA [80, 81, 82]. SHG has two drawbacks. First, the probability of two photons combining is very small, so the input laser must be very powerful. Second, unlike fluorescence, where a material absorbs light and reemits it in a wavelength characteristic of that dye, SHG is defined as the doubling of the laser frequency, so all sources of SHG will appear identical without further characterization. Often, just the morphology of the object is sufficient to distinguish, for example, myosin from collagen, as in figure 3.4. However, this is not an ideal approach, nor does it leverage the strengths of SHG. By better understanding the process of SHG production, we can identify how SHG from one type of tissue would be unique, whether it be an emission direction, polarization, or intensity specific to the structures in question.

To this end, we investigate the wavelength dependence of SHG from zebrafish (*Danio rerio*) muscle. We measure the SHG from regions of the muscle and characterize the resulting spectrum. In addition, we identify some the of characteristics of SHG imaging distinct from fluorescence imaging. The organism in question is a common subject in optical microscopy due to a number of favorable factors, such as: its genome is sequenced, it can be induced to be highly transparent, it matures rapidly, among other practical reasons for its use as a model organism. Therefore, our

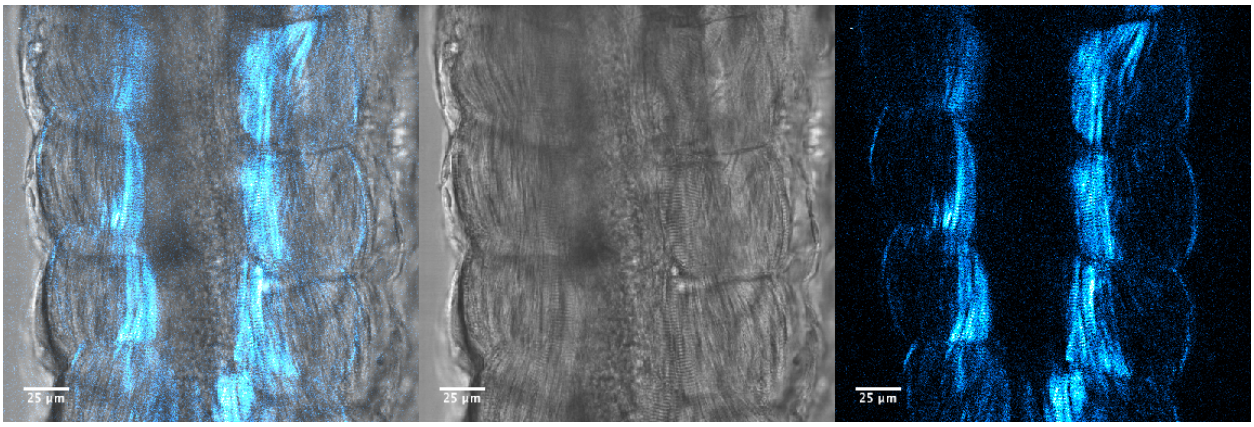

Figure 3.1: Sagittal section of zebrafish 36 hours post fertilization. Left, composite brightfield and transmitted SHG. Center, brightfield. Right, transmitted SHG. Scale bar is 25 microns.

conclusions will be specific to muscle from zebrafish, but most of it is transferrable to images of other organisms.

Muscle in zebrafish are organized into chevron-shaped somites, as shown in figure 3.3. The muscle surrounds a central notochord, which bisects figure 3.3. This image illustrates one of the central attractions of second harmonic generation as an imaging modality. Without any artificial or genetically encoded labels, zebrafish still produce significant autofluorescence, but fluorescence has very small overlap with the SHG wavelength. In addition, fluorescence is radiated isotropically, while muscle SHG is coherently forward directed [84]. There have been a number of studies of wavelength dependence of SHG in proteins [85, 86, 87] but none in muscle, with its unique microscopic structures (see section 3.1.1).

There are a number of factors that could contribute to wavelength dependence. The SHG produced at a point is given by $P^{(2)}(x) = \chi^{(2)}(\omega, \mathbf{x}) : \mathbf{E}(\omega, \mathbf{x})\mathbf{E}(\omega, \mathbf{x})$, where $\chi^{(2)}$ is the SHG susceptibility and $\mathbf{E}$ is the incident electric field vector. From direct

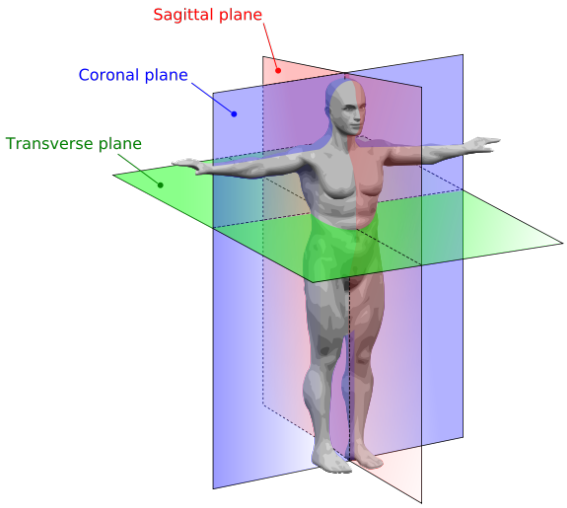

Figure 3.2: Anatomical planes. Zebrafish are oriented laterally, meaning the sagittal plane is parallel to the ground and perpendicular to the laser. Image from [83].

inspection, it is clear that wavelength dependence could originate from the susceptibility itself, which would be due to the underlying material properties of the protein. The incoming electric field will vary in power, which is part of a greater wavelength dependent instrument response. Last, there could be variation in the efficiency of SHG production due to phase-matching, resulting from the underlying crystalline structure of the muscle. It is this last point that suggests possible diagnostic applications of the wavelength dependence of SHG, as there are a number of disorders, namely muscular dystrophy [88], which alter the underlying crystalline structure [89].

3.1 Structure of Muscle

3.1.1 Muscle Construction

Muscle, in particular, is an excellent candidate for biological SHG susceptibility, because it possess a high degree of spatial order. To facilitate gross movement in an

Figure 3.3: Label-free image of fixed zebrafish embryo, sagittal section. Scale bar is 50 microns. Green is autofluorescence from the fish and the fixative, blue is transmitted SHG. Fish is 36 hours post-fertization.

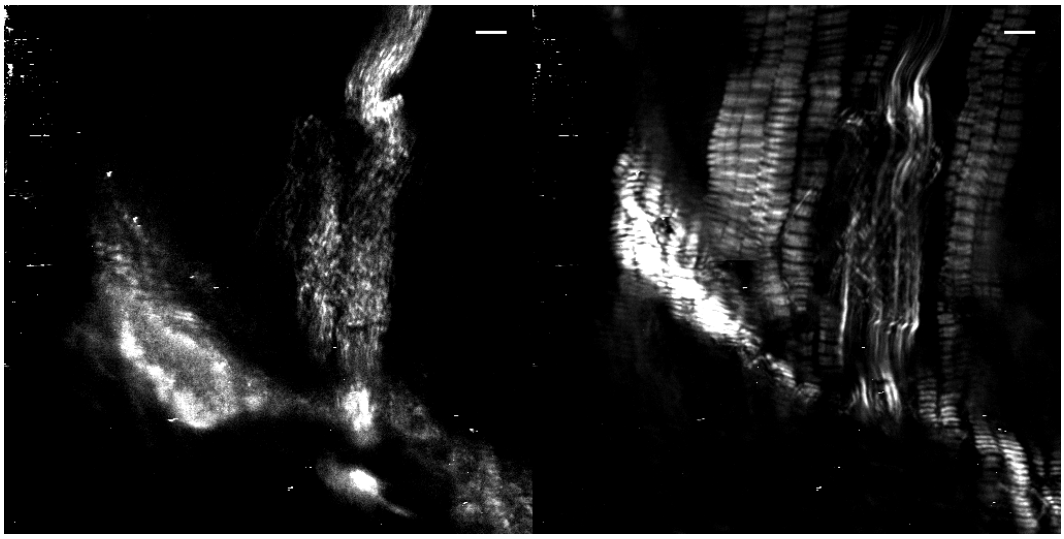

Figure 3.4: Second harmonic generation from muscle and collagen. Image is a sagittal section from the end of a zebrafish tail. Left: Epi collected emission. Collagen are the wispy lines in the middle running vertically. The horizontal streaks are luminescence from laser damage. Right: Trans collected emission. Again, collagen are the wispy lines in the middle, while muscle are the striated ribbons to either side. Exclusively trans-directed SHG is characteristic of muscle. Image taken with 100x α-Plan-Apochromat 1.46NA. Scale bar is 5 microns.

organism, it must be organized in a way to allow it to coordinate the molecular motions of proteins across the entire muscle. In general, muscle fibers are organized on the molecular level as a lattice of parallel protein filaments, including the force generating and scaffolding components, myosin and actin, respectively. Myosin, a molecular motor, pulls on the actin, and, due to long-range correlation of the activation of the myosin, this results in muscle contraction. The myosin and actin are packaged in periodic longitudinal units called sarcomeres, shown in figure 3.5. The myosin are tied together in the center of the sarcomere, called the M-line [90], while the actin anchoring positions are Z-lines, as in figure 3.5. The region of the sarcomere containing the myosin appears optically distinct, and is called the A-band. The myosin is also loosely bound on both sides to the Z-lines via titin, a spring-like protein,

maintaing its position in the center of the sarcomere and maintaining an equilibrium resting distance between the Z-lines. When activated, the myosin ratchets against the actin, pulling neighboring Z-lines closer together.

Myosin and actin are arrayed in hexagonally packed filaments called myofibrils [91], with the protein arranged with a characteristic spacing between myosin filaments of 40 – 50 nm [92, 93, 94, 95]. This packing is illustrated in figure 3.6. That is, the lattice vectors observed by x-ray diffraction are consistent with hexagonal Fourier amplitudes of $K_{nm} \propto a^{-1}\sqrt{(n^2+m^2+mn)^{-1}}$, where the lattice spacing is the characteristic length of a = 40–50 nm, depending on the contractile state of the fiber [94, 96, 95][1]. The hexagonal packing has also been clearly observed in TEM micrographs [91, 92]. Each myofibril is approximately 1 μm across. Myofibrils are in turn packed into myocytes, the cellular units of muscles, which are about 10 μm across [97, 92].

The myosin and actin are packed with high regularity within the myofibril, and the myofibrils are highly aligned with their neighbors [98], shown in figure 3.5, and this regularity contributes to strong production of SHG. Although both the myosin and actin fibers are highly ordered, it is known that SHG only originates from the myosin, based on complimentary staining [99, 100, 101] and on mutating myosin to reduce SHG [102, 103]. Depending on the contractile state of the muscle fibrils, the sarcomere spacing will have differing myosin spacings [100, 104, 105, 96]. The longer the sarcomeric unit, the smaller the myosin spacing [93, 96]. In addition, muscle

[1]It appears the actin are anchored to the Z-line in a square lattice, while the myosin are held at the M-line in a hexagonal lattice. So, close to the Z-line, the packing will be dominated by the square-lattice of the rigidly held actin [92, 93].

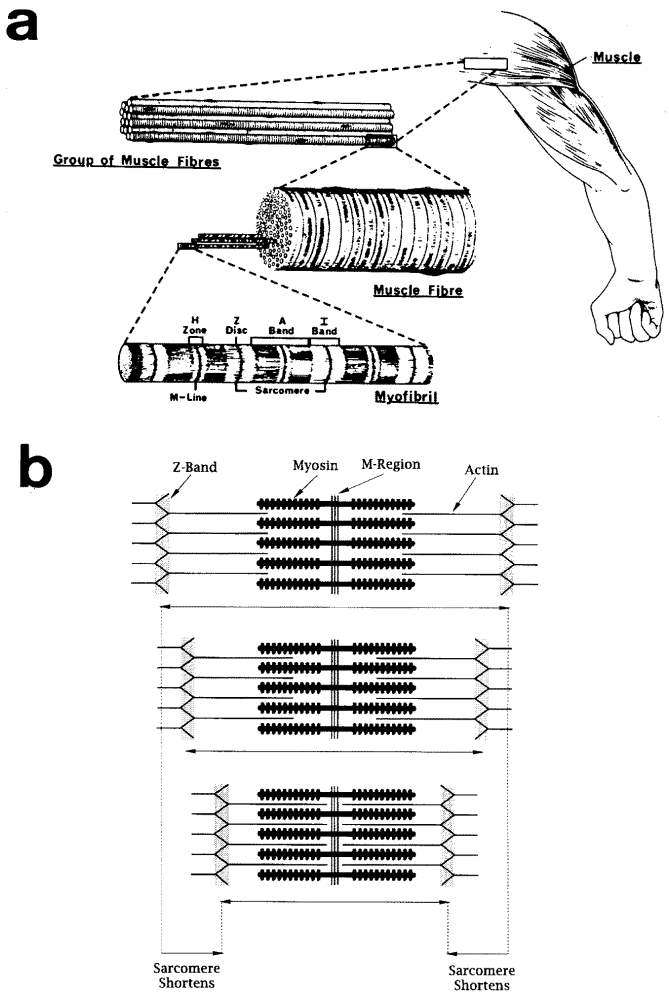

Figure 3.5: (a) A multiscale illustration of muscle organization, and (b) a cartoon of the process of muscle contraction. Missing from this cartoon is the fact that the myosin spacing grows as the sarcomere compresses [93]. Image is from [107].

contraction is driven by the conformation transition of the myosin molecular motor, which causes the relative angle of the asymmetric units to change with respect to the myofibril axis [106]. It has been hypothesized that when at rest, the myosin tails at the M-line are packed together in a way that cancels inversion asymmetry, possibly causing contraction dependent SHG [105]. These distances and angles determine the degree of the second harmonic generation, so we expect some heterogeneity in images of muscle, but they will all retain the same basic patterns.

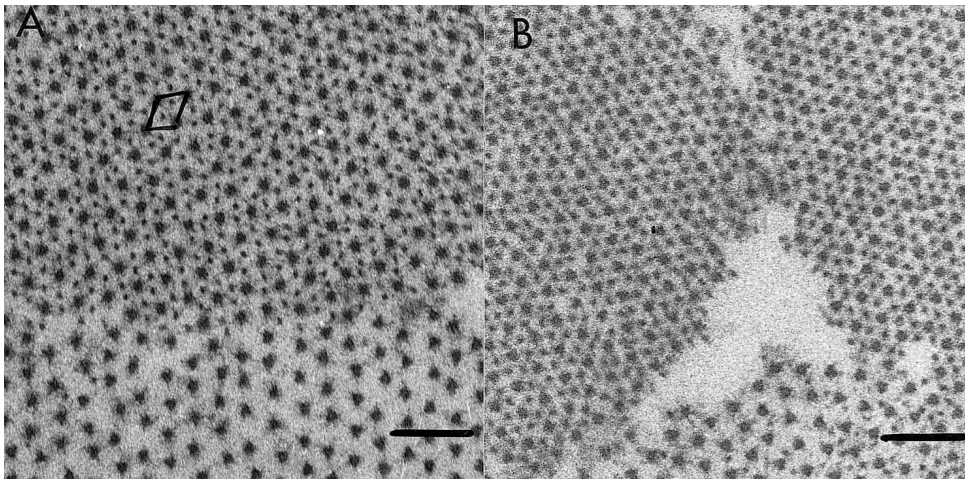

Figure 3.6: TEM micrographs of myofibril crosssection, showing hexagonal packing of myosin and actin. Myosin are the larger dots, while actin are smaller dots. (a)Relaxed fibrils. The bottom portion of both images is a portion of a fibril with only myosin, e.g., near the M-line. (b) Contracted fibrils. The scale bar is 100 nm. From [93].

3.1.2 Optical Properties of Muscle

The regularity in myofibrils carries over into its optical properties. Because of the underlying chirality of the proteins, myofibrils have well documented birefringence [108, 109, 110], meaning the muscle has a fast (ordinary) and slow (extraordinary) axis. The optical axis, e.g., the slow axis, is parallel to the myosin filaments [108]. The birefringence is defined as the difference between the refractive indices $B = n_e - n_o$, corresponding respectively to the extraordinary and ordinary axes. More specifically, observations show $B = 2 \cdot 10^{-3}$ [108, 110]. In addition, this birefringence has been observed to change systematically and approximately linearly with the length of the sarcomere or, conversely, with the density of myosin thick filaments, where birefringence increases by up to a factor of two between a relaxed sarcomere and one in contraction [108]. The birefringence has a number of origins. First, there is the underlying chirality of the protein, or more specifically, an intrinsic birefringence due to

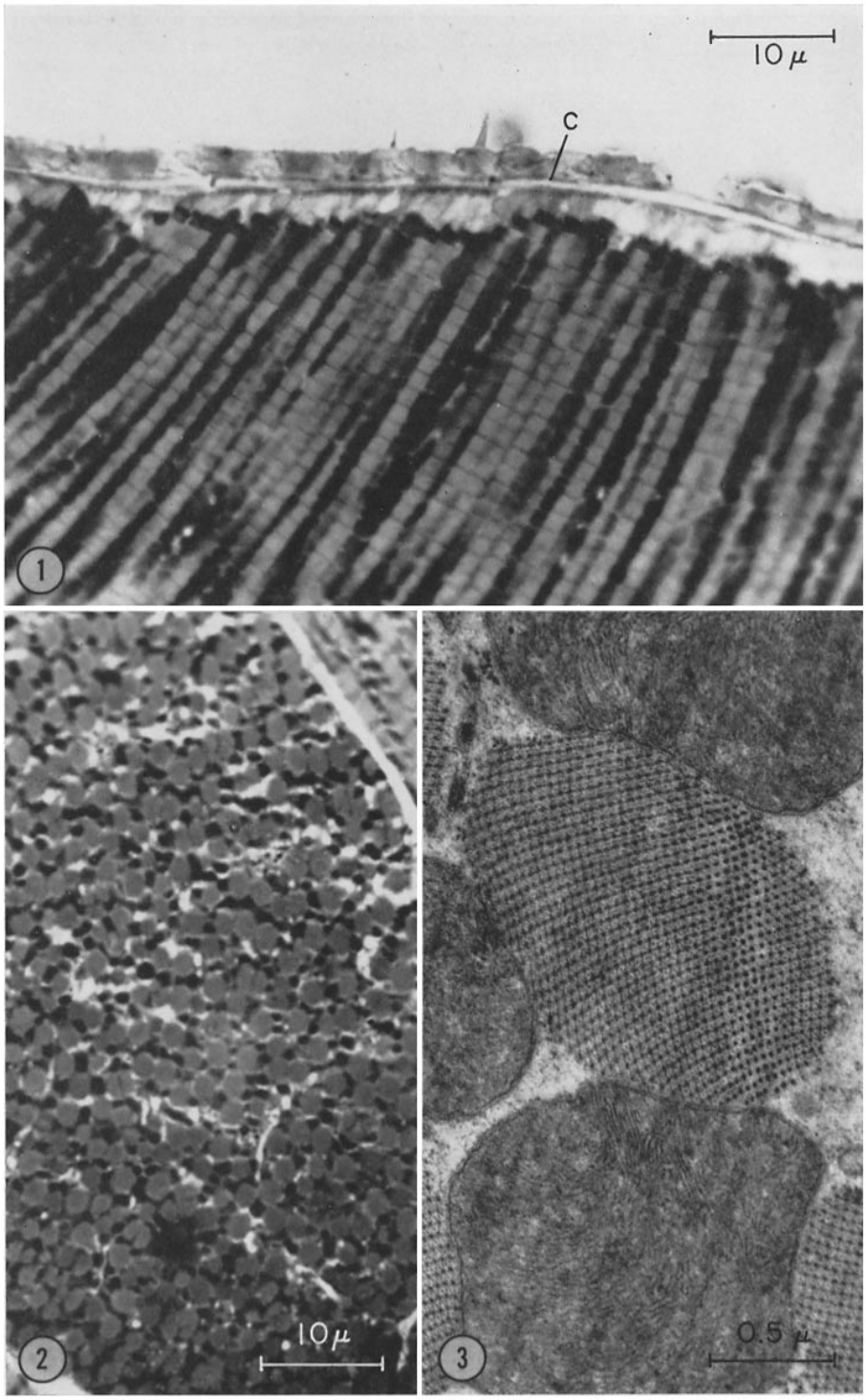

Figure 3.7: (1) A longitudinal section of muscle, showing myofibrils, light striped bands, and mitochondria (dark objects between myofibrils). The Z-lines (dark lines), and to a lesser extent, the A-band and M-lines (lighter lines) are visible. (2) A crosssection of the same muscle, showing individual myofibrils packed in a quasi-crystalline manner within the larger cell. (3) Close-up of a single myofibril, with myosin stained as dark dots. Image is from [92].

asymmetric polarizability of the underlying electrons, and a change in the underlying protein structure, such as conformational motion of the myosin heads, would alter the birefringence to some degree. Second, there is form birefringence, originating from the highly asymmetric cylindrical protein filaments. The aligned filaments cause the material to appear to have different character depending on the polarization of light, were a liquid crystal. As sarcomeres contract, their myosin filaments increase their separation (an observed conservation of volume [93]), and this drives a change in the birefringence. Both types of birefringence combine to alter the production of SHG, primarily due to spatial beam walk-off, which limits the effective interaction length of the focused laser [111, 112], and also due to coupling between the ordinary and extraordinary directions [113]. It has been estimated that form birefringence accounts for approximately 70% of the total birefringence [108]. In addition to birefringence, the order in myofibrils also gives rise to optical Bragg diffraction. This is present on the nanometer-scale, where the ordered protein can be studied by x-ray crystallography *in vivo* [95], and it is also present on the micron scale, where optical diffraction is used to study sarcomere structure [114, 115, 116]. Bragg diffraction affects phase-matching conditions, which are vital to determining the efficiency of SHG conversion, as will be shown in section 4.2.2.

A second major influence on the second harmonic generation is the wavelength-dependent index of refraction. The refractive index of tissue has been explored in a number of contexts [117, 77, 118, 79, 119, 78]. Pure protein has a refractive index of 1.5 – 1.6 [78], but myofibrils have a hexagonal lattice of tightly packed heteroge-

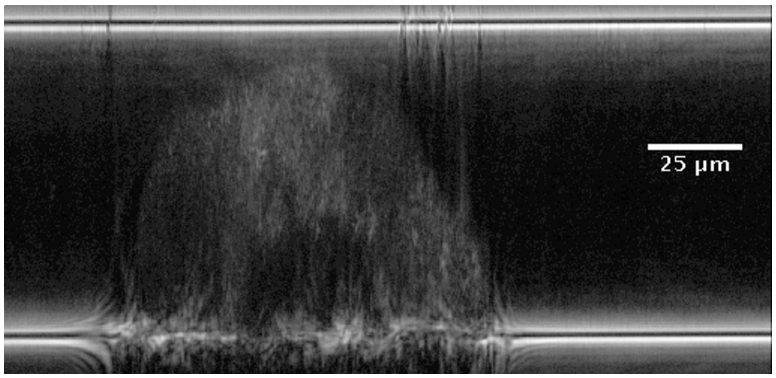

(a) Reflection intensity

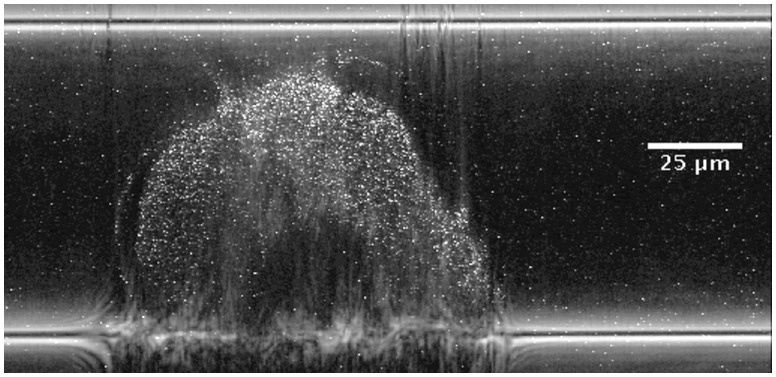

(b) Reflection intensity with endogenous fluorescence overlay

Figure 3.8: Reflection of 850 nm laser pulses indicates the optical density of the zebrafish transverse section. Laser originates from the top of the image. The refractive index heterogeneity of the zebrafish muscle and neural tube causes significant optical aberration, realized as the distorted boundary between the fish and the glass, at the bottom of the images. The top band and bottom bands are the boundary between the gel holding the section and the glass coverslips.

nous protein, and it will have an effective index that is a combination of protein and water. Techniques measuring an average index report a characteristic index of 1.4 [79, 118, 119]. Tissue-specific variations cause the index to vary by 10%. For example: epidermis is 1.44, dermis is 1.4, and the outmost layer of skin, the stratum corneum, is 1.55 at 650 nm [77, 119]. Attempts to measure the refractive index of a 5-day old zebrafish by measuring the optical thickness of the sample using the Ti-Sapphire laser [118] were stymied by the optical heterogeneity of the muscle, shown in figure 3.8. Because tissue, in particular myofibrils, has no electronic resonances in the visible wavelengths, their refractive properties obey the general relation of normal dispersion, where the refractive index increases with increasing frequency. Indeed, Ding et al. [119] and Andersen and Nir [78] find wavelength dependent refraction indices well described by the Cauchy and Lorentz-Lorenz dispersion relations, respectively. Works that investigate the polarization dependence of the refractive index of ovine and porcine muscle find results consistent with the previous birefringence mentioned above [77]. Hence, the index dependence of muscle will have a simple monotonically decreasing functional form given by the Cauchy dispersion relation. In this work, we take the wavelength-dependent refraction indexes for porcine muscle, as measured by Cheng et al. [120] and reported by Bashkatov et al. [77]. Fitting their data to a Cauchy dispersion gives an refractive index for muscle across the entire relevant spectrum:

$$n(\lambda) = \sqrt{2.116 + \frac{22.45\lambda^2}{\lambda^2 - 53.9343}}. \tag{3.1}$$

where λ is expressed in microns.

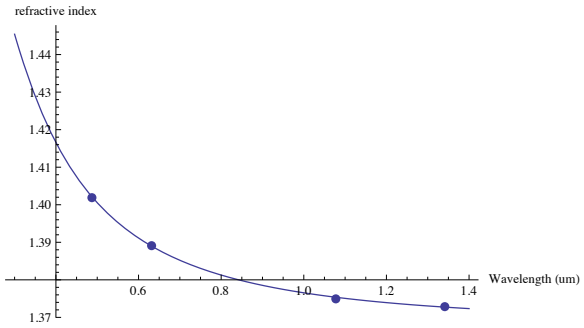

Figure 3.9: Using experimentally measured refraction index data from porcine muscle [120] (total internal reflection), we determine the refractive index across the entire spectrum. Points are experimental data, line is fit by eq. (3.1).

3.2 Methods for Measuring Second Harmonic Generation

All zebrafish, unless noted, were embedded in 1% or 2% low-melting agarose with 30% w/v Danieau buffer for imaging. After fertilization, the embryos are transferred in a petri dish to a 28 degree incubator in egg water. The fish grow for 24 hours, and then pheynl-thio-urea (PTU) is added (0.003% w/v) to inhibit pigment formation. After the desired amount of maturing time elapsed, fish were anesthetized in 0.015% tricaine. For fixing, the fish were immersed in 4% PFA at room temperature for 45 minutes. They were washed on a nutator for 20 minutes three times in Ca-Mg free PBS 1x. They were stored at 4 °C until needed. Live fish were anesthetized and immediately laterally embedded in agarose containing 0.015% tricaine.[2] Two-well #1 cover-slips (Lab-Tek, Nalge Nunc International) were used to contain the samples. Although no live samples are presented here, they do not produce SHG that is noticeably different from fixed fish.

[2]All fish preparation protocols were conducted and refined by Bill Dempsey.

Fish were oriented in the gel to maximize resulting SHG, which depended on the polarization of the microscope laser, i.e.,the laser field was oriented away from the central myosin-actin axis [121, 101]. Imaging took place at the House Ear Institute's Zeiss 710 LSM Confocor 2. The laser was a Coherent Chameleon Ultra II Ti-Sapphire 140-fs pulsed laser. Laser power was selected to be approximately 60 mW at the back aperture to the objective, which was determined by wavelength corrected power meter. Imaging was done with Zeiss objectives which were corrected for UV-VIS-IR imaging. All images were taken with the 25x LD LCI "Plan-Apochromat" 0.8 Imm Corr DIC unless noted otherwise. The correction collar was used to optimize point spread function at each wavelength, using either Dark Red Quantum Dots from NN-labs, Inc. or luminescent debris from Zebrafish skin to find point spread functions. Given 60 mW at the back aperture, this leads to average power densities of approximately 10 MW/cm^2, and peak power densities[3] of 10^{11} W/cm^2. All SHG was trans-imaged, using a 0.5 NA condenser to collect the light. The laser was filtered with a Semrock 680/SP short-pass filter, and the SHG was selected using a Semrock 417/60 bandpass filter. To obtain wavelength-corrected images, the wavelengths between 780 nm and 890 nm were used in 10 nm intervals, and the laser power was corrected to bring the power at the back aperture of the object as close to 60 mW as possible. After collection, the images were computationally corrected for objective transmission, condenser transmission, and PMT sensitivity. Images were not corrected for short-pass or bandpass filter transparency due to the small variation across the spectrum. The correction collar of the 25x was used to obtain an optimal point

[3]Reported from `http://www.coherent.com/downloads/ChameleonUltraFamily_DS_0510.pdf`.

spread function. However, the collar was not adjusted for each wavelength, primarily because manually adjusting the collar disrupted the sample alignment, and because the 0.8 NA objective had small wavelength dependent deviation in the focus, shown in figure 3.11. In addition, spectra did not differ systematically with collar adjustment.

To prepare morphant fish to recapitulate the phenotype of fish with Duchenne muscular dystrophy [122], a morpholino[4] sequence targeted to the *dmd* gene locus was injected into the yolk of zygote-stage zebrafish. The injection was 2.3 nL at a concentration $\sim$2.174 ng/μL, using a nanoject II Auto-nanoliter injector. Morphant fish which developed to 5 days were screened and prepared for imaging as above.

To visualize cell membrane and nuclei locations within the somite compartment, we used a transgenic zebrafish, which was a bistronic line coexpressing membrane-targeted cerulean fluorescent protein and a fusion H2B-Dendra2 fluorescent protein, targeted to the nucleus.[5] A founder of the line was crossed with an AB line wild-type [123]. The larvae were screened at 24 hours post fertilization for fluorescence and, if positive, prepared as above.

Laser damage proved to be the primary obstacle to optimizing images at every wavelength. As shown in figure 3.13, cells are easily damaged by two-photon laser pulses. Damage is not uniform, but it appears to be nucleated at bubbles or other optical heterogeneities. Once damage forms, the bubble grows larger and larger with each subsequent scan. Although the bubble may shrink over time, a permanent lesion

[4]Morpholinos are synthetic nucleic acid polymers designed to bind to mRNA and prevent the translation of the protein coded by specified target sequence. `http://en.wikipedia.org/wiki/Morpholino`

[5]Dempsey et alf in preparation

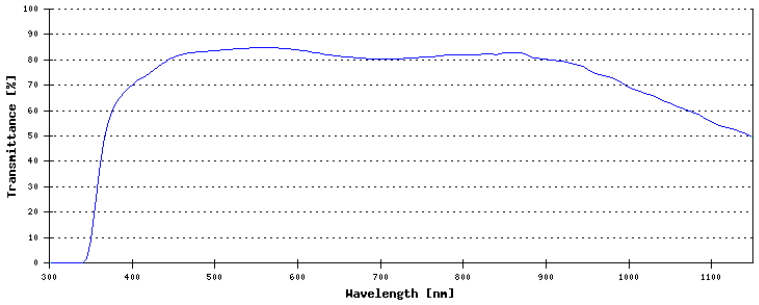

(a) Zeiss LD C-ApoChromat 25x 0.8 NA

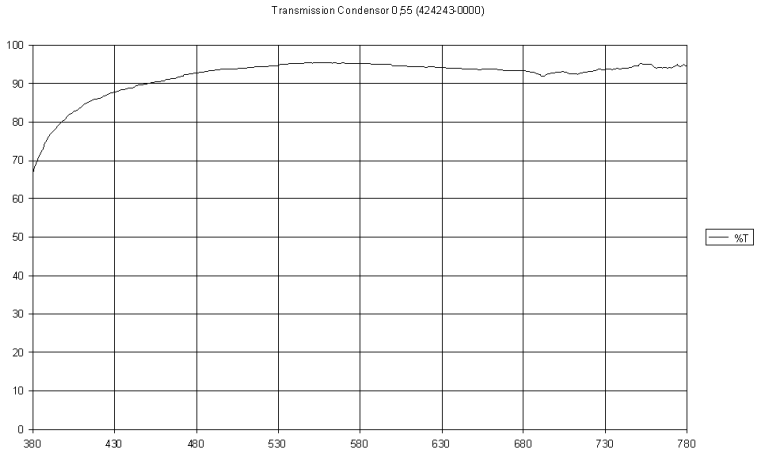

(b) Zeiss 0.5 NA Condensor

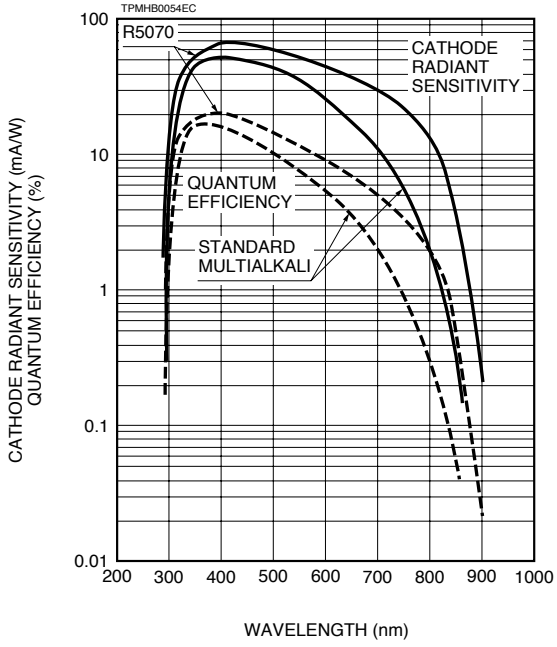

(c) Hamamatsu R5070 PMT

Figure 3.10: Each element of the imaging pathway has different wavelength dependent transmission or sensitivity. These characteristic spectra provided by the respective vendors were used to correct the signal.

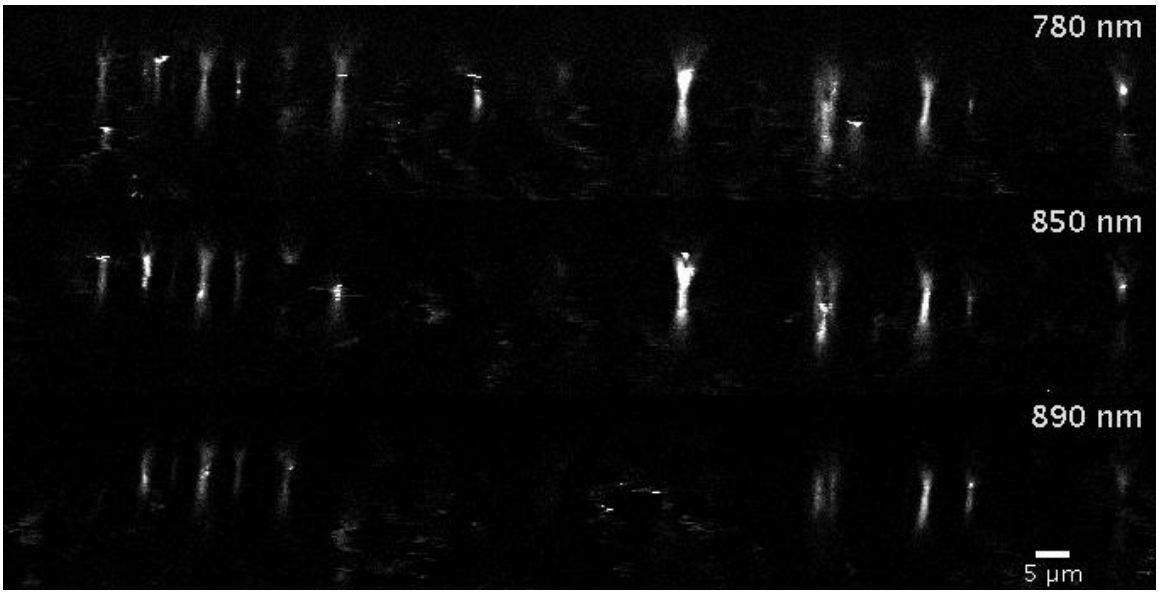

Figure 3.11: Fluorescent debris from the zebrafish were used to measure point spread functions at 790 nm, 850 nm, and 890 nm, using 25x 0.8 NA

remains.[6] Broadband emission from the damage sites is suggestive of laser-induced breakdown [124, 125] and self-steeping into supercontinuum generation [126, 127, 128]. In addition, fish need to be treated with 1-phenyl 2-thiourea (PTU) during embryogenesis to suppress the formation of pigmented cells such as melanocytes. Melanin is strongly absorbing, and irradiation leads to the formation of sufficient free radicals to initiate rapid laser damage and ablation. In addition, the broadband luminescence from pigment competes with SHG, confusing image interpretation, as shown in figure 3.12. Even with limited pigment, damage may still readily occur. As a result, power and observation times were limited.

Because of chromatic dispersion, the focus of the laser varies in depth as the

[6] Although the peak power of the laser at 25x, 0.8 NA is 10^{11} W/cm^2, self-focusing and near-field enhancements can easily elevate peak electric fields to near breakdown levels, 10^{15} W/cm^2. This is likely why damage nucleates at bubbles, lesions, and pigment (a source of free radicals). In addition, this makes imaging with 100x and other high NA objectives difficult to achieve without extreme damage to the sample.

Figure 3.12: An image of second harmonic generation from morphant zebrafish, optically sectioned along the sagittal plane. The speckling along the central neural tube is broadband luminescence from pigment cells. Lesions are evidenced by the circular outlines of luminescence. The microspeckling in the luminescence is due to rapid changes in the substrate, which are faster than the laser pixel dwell time, 1.56 μs. Scale bar is 50 microns.

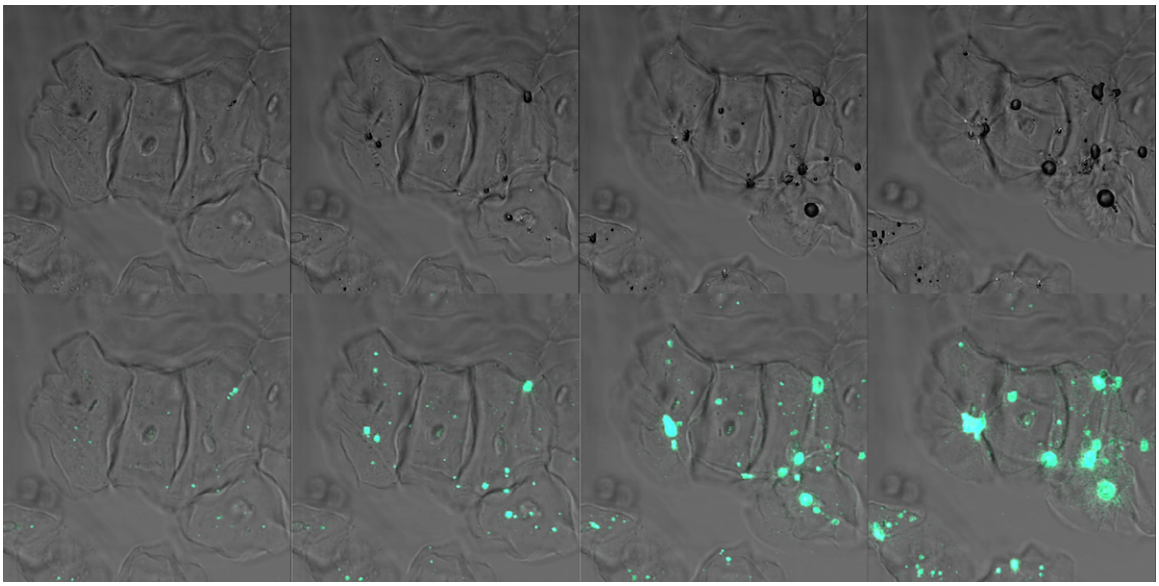

Figure 3.13: Epithelial cells accumulate damage over a 2 minute exposure to 820 nm Ti-Sapphire laser pulses, 10% power. The signature of the damage is broadband radiation, extending over the entire visible spectrum. The damage appears to be nucleated in tiny bubbles. The bubbles grow over time, ultimately tearing the cell. Upper Row: Transmitted laser light, Lower Row: Transmitted light plus false-color epidetected luminescence.

wavelength is tuned. The deviation in the depth of the focus between an image taken with the laser wavelength 780 nm and at 890 nm is over 1 μm, which is the width of a myofibril. Therefore, an image at 790 nm often contains myofibrils not in an image at 890 nm, and vice versa. To overcome this complication, images were taken in large "z-sections," or coronal slices, meaning the objective was stepped along the axis of laser propagation to image lines in multiple focal planes. Because the imaging resolution in the z-axis is well over a micron, taking 0.35 μm slices allowed all of the muscle to be captured. However, as mentioned in the last paragraph, exposure time needed to be limited to avoid complete ablation of the sample before all wavelengths could be imaged. As a result, only a 2D image was taken, with one axis in the z-direction (parallel to the laser propagation) and another axis perpendicular to the laser, chosen

to capture a region of interest but not necessarily with any specific orientation with respect to the fish or muscle. Variations in muscle fiber alignment within the somites cause there to be few preferred directions, allowing selection of planes which provide best imaging conditions.

3.3 Discussion

3.3.1 Representative Images

figure 3.15 shows a representative image of second harmonic generation from a 5-day old wildtype zebrafish. The muscle is clearly packed into chevron-shaped somites, and the dark Z-lines stand out in stark contrast with the bright A-bands. The myocytes contain highly aligned domains of tightly packed myofibrils [98], although the fish is too young for the muscles to develop to a state of full compaction. We a level of organization between the 1 μm myofibrils and the 10 μm myocytes that has not been well documented in the literature. The intensity of the SHG varies significantly across the muscle, corresponding to fluctuations in density and alignment. Although the individual myofibrils are not readily apparent, they can be recognized at the boundaries of the somites as the discrete steps, as seen on TEM in figure 3.7. Their width of approximate 1 micron is sufficient to resolve at this resolution, but their tight packing and close alignment with neighboring myofibrils makes distinguishing individuals difficult, but not impossible. Sometimes myofibrils are separated sufficiently to resolve individual fibers, even while in alignment with their neighbors, as

shown in figure 3.14. Because SHG comes from the dense myosin filaments within the sarcomeres, diagrammed in figure 3.5(a), we can interpret the dots in figure 3.14 to be myosin filaments radiating from the M-line. Because oppositely aligned myosin meets at the M-line, it is not a source of SHG, and this will be discussed further in section 4.3. The Z-lines are also dark, because they lack myosin completely. Hence, we observed the expected double lobed pattern in each sarcomere. This is a common motif observed in other studies that have isolated single myofibrils [129, 101].

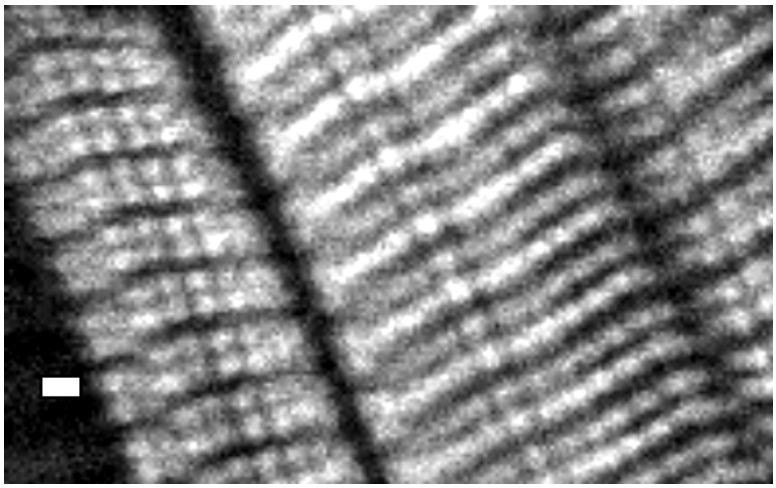

Figure 3.14: Close-up view of discrete structure of myofibrils. The Z-lines are dark, and the M-lines are dark. However, the M-lines are sandwiched between the A-bands, where myosin filaments produce SHG (see figure 3.5). Scale bar is 1 micron.

Another common motif is an interlocking herringbone pattern, as in figure 3.16. Others have observed these patterns, calling them "verniers" [99, 89] or "pitchforks" [100]. Their cause is unknown, although Recher et al. attribute them to maturing myofibrils [100]. When we look at the same muscle from two perpendicular planes, as in figure 3.7, we see these patterns appear where myocytes and small bundles of myofibrils come in close proximity. Because myosin runs parallel to the membrane, no SHG producing structures cross the membrane. However, figure 3.17

Figure 3.15: Second harmonic generation from wildtype. The section is along the sagittal plane. Scale bar is 50 microns.

shows the herringbone pattern crossing the fluorescent signal from the membrane, indicating that the herringbone pattern is an optical artifact, not a physical structure. Friedrich et al. observed a "vast increase" in vernier pattens in dystrophic mutants [89], which can be explained by the relative increase in disordered myofibrils [130], allowing more crossing within the imaging plane, leading to an apparent increase in subsequent vernier patterns. This will be more closely explained in section 4.3.

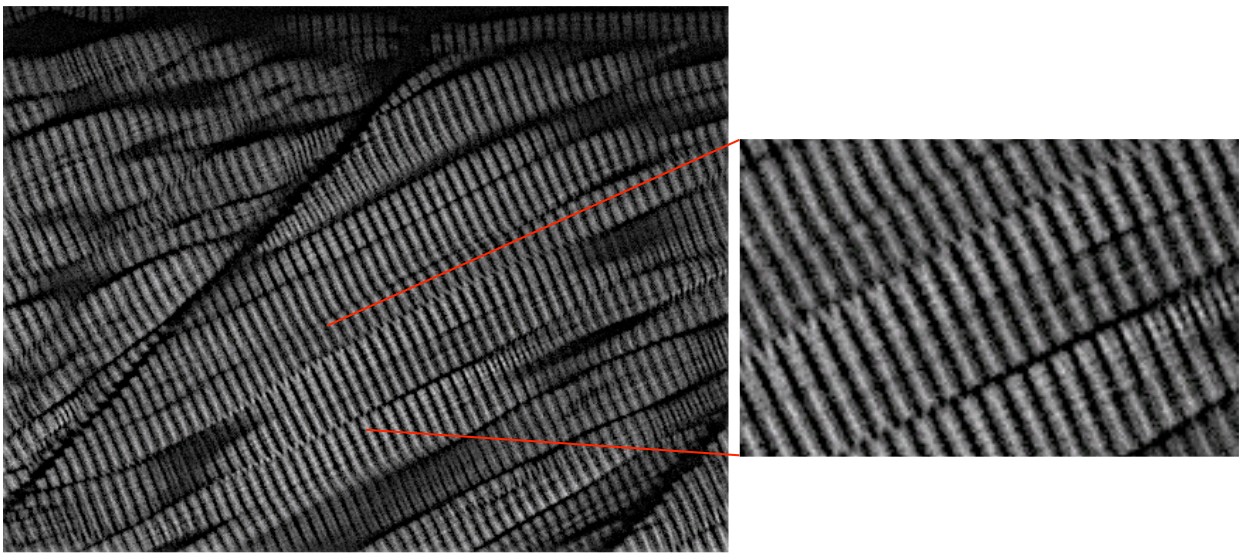

Figure 3.16: Inset shows magnified view of herringbone or "vernier" pattern from a 7 day post-fertilization zebrafish.

Morphant muscles show the same motifs as the wildtype muscles, which is to be expected because dystrophic disorders affect the structural reinforcements and anchoring components of the muscle [122, 131], and not the internal packing of the sarcomeres.[7] The myofibrils of morphant fish show significantly more flexibility and disorder, illustrated in figure 3.19. As morphants age, the myofibrils tear away from

[7]However, there is an inherent selection bias in this statement, as once the the structural integrity of the myofibrils are compromised to the point of disrupting the myosin lattice, the fish will be at or near death. We only studied live fish (or fixed live fish).

each other, losing muscle integrity due to a lack of sufficient dystrophin expression linking the interior of the muscle cells to the exterior. This work only deals with 5-day old morphants, leaving open the possibility that older morphants could differ in their SHG signature. Although this would not necessarily be useful diagnostically, because the morphant would be readily identifiable by the morphological degradation, it may help isolate the source of SHG spectra. Also, but not readily apparent from the images in this thesis, morphant SHG is substantially dimmer. Images in this work have been contrast-brightness corrected to be as easy to visualize as possible.[8] In addition, figure 3.19 shows that morphants contain disordered muscle interspersed with highly ordered muscle, leading to images with high dynamic range. figure 3.19 and figure 3.20 also reveal that myofibrils appear to be organized into larger bundles around 5 μm wide, something not well documented in the literature, but perhaps best documented by Sanger et al. [132].

3.3.2 Wavelength-Dependent SHG

Properly wavelength corrected images proved to be difficult to obtain, mostly because of the limited exposure time possible before the laser destroyed the sample. However, the protocols outlined in section 3.2 enable measuring a wide spectrum from 780 nm to 890 nm at 10 nm intervals. figure 3.21 shows representative results for a wildtype 5-day old fish. Because each point in the slice, Fig 3.21(a), has a different myofibril alignment and intensity, there are a number of ways to analyze the results. Absolute

[8]The only image alterations done on the images in this thesis were standard contrast and brightness adjustments along with cropping out regions of interest.

intensities are not reliable because too may factors alter the amount of laser power being delivered to a given point and the fraction of SHG that arrives that the detector,[9] so one approach is to normalize each pixel by the maximum intensity of that pixel in the spectrum, $I(i,j,\lambda) = I(i,j,\lambda)/\max_\lambda I(i,j,\lambda)$. This makes each pixel a value between 0 and 1, and these spectra may be averaged to produce an average normalized spectra, shown as the blue line in figure 3.21(b). The image at each wavelength is histogrammed and plotted together, giving a normalized spectrum density, which is a visual representation of the likelihood of a pixel having a normalized spectral value at any wavelength. Finally, in figure 3.21(c), we see the normalized spectra adopt a characteristic density curve. The spectra at different points are largely intensity independent, expect for those points with exceptionally low postcorrected intensities. These points appear to the eye as background, but they have a different spectra, shown in figure 3.22. These spectra are likely forward scattered autofluorescence, because they most occur in the regions between somites. Autofluorescence is not uniformly distributed throughout the fish. SHG and autofluorescence are largely mutually exclusive (see figure 3.3).

Although an equivalent slice from a morphant fish, figure 3.23(a), produces substantially less SHG than the wildtype, the overall spectra shares many characteristics with the wildtype spectra. The normalized intensities still have a substantial drop-off at 850 nm, seen in figure 3.23(b), but the spectra of the morphant have a less

[9]For example, agarose density variations will alter the transparency; The position of the fish in the sample well will affect the focusing and the resulting transmission to the detector; The condenser lens must be readjusted for each sample, and it can only focus on a single plane, reducing collection efficiency for nonoptimal planes; etc.

pronounced plateau in the wavelengths shorter than 850 nm. Because the morphant contains many morphological similarities with the wildtype, we expect the spectra to be similar, due to the phase-matching being consistent (see section 4.2.2). However, the spectra of a few points of interest plotted in figure 3.23(c) differ significantly from the trend in figure 3.21(c). These points were selected from regions with lower intensity, and therefore have a character closer to figure 3.22. A background spectrum was estimated by measuring the signal from regions outside the somites, which should be nearly SHG-free. Subtracting this spectrum gives figure 3.23(d), revealing that the morphant spectrum absent the estimated background, remains very similar to the wildtype spectrum. Based on this preliminary analysis, there is no quantifiable spectral difference between 5-day-old morphants and 5-day old wildtypes. Clear morphological differences exist, such as visible tears and significantly lower conversion efficiency due to poor alignment of the myofibrils. A future experiment with fluorescently labeled myosin (or actin) would help to determine if there is myosin in the morphant which is too disrupted to produce SHG.

To explain the difference in intensity but similarity in spectral shape between wildtype and morphant zebrafish muscle, we must construct a theoretical framework for second harmonic generation. We also have seen that there are features such as the herringbones (Figs 3.14 and 3.18) that are not observed in fluorescence microscopy, which we hope to explain as well. Ultimately, second harmonic generation proves to be a valuable tool for imaging and studying muscle development and organization *in vivo* without the need for any dyes or stains. The next chapter will explore the theo-

retical aspects to SHG from zebrafish muscle and will further address the observations revealed in the present chapter.

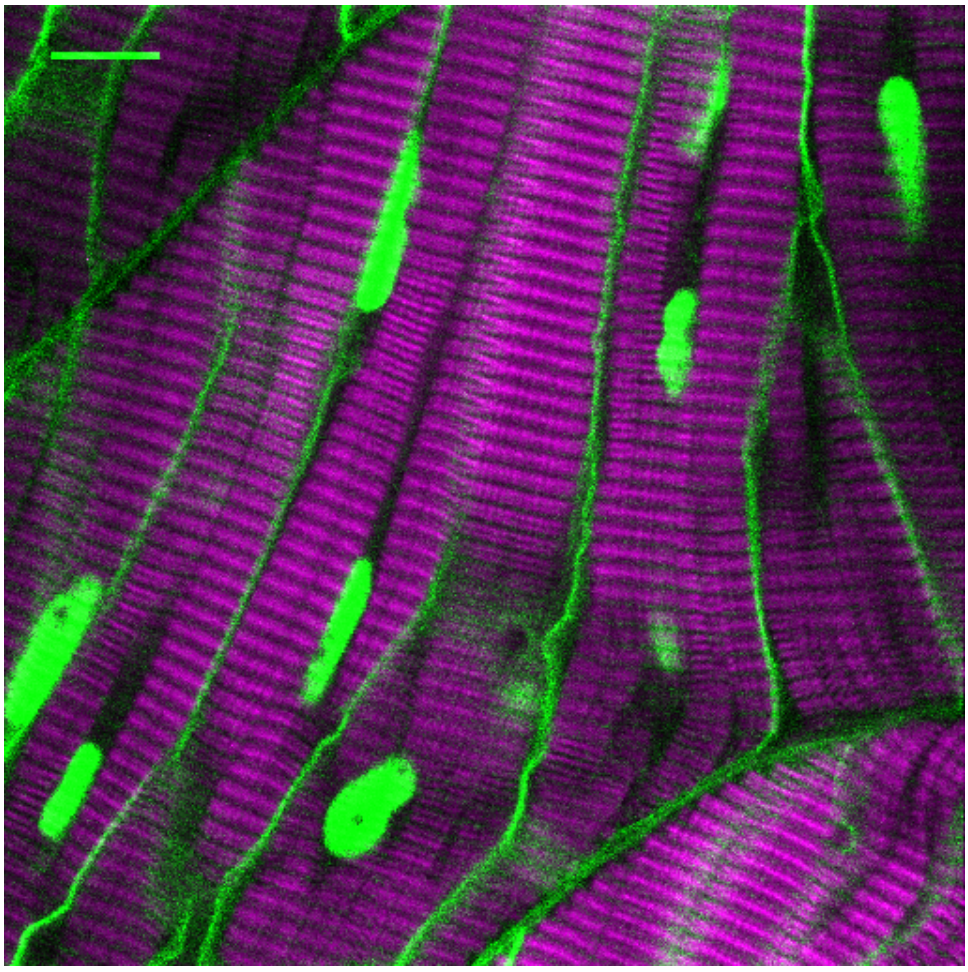

(a) sagittal plane

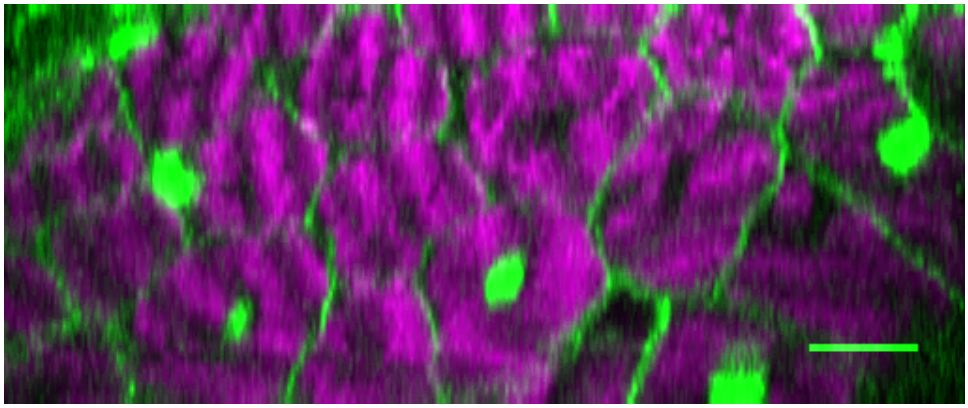

(b) transverse plane

Figure 3.17: Transgenic fish were used to visualize the interface between myofibril SHG (purple) and fluorescent-protein labeled membranes and nuclei (green). (a) Myocytes run in and out of the imaging plane, and myofibrils within a myocyte vary in their packing density and degree of contraction. (b) A perpendicular cut through the same image, showing the semi-crystalline packing of myocytes. The resolution in (b) does not allow one to resolve individual myofibrils. Scale bars are 10 μm.

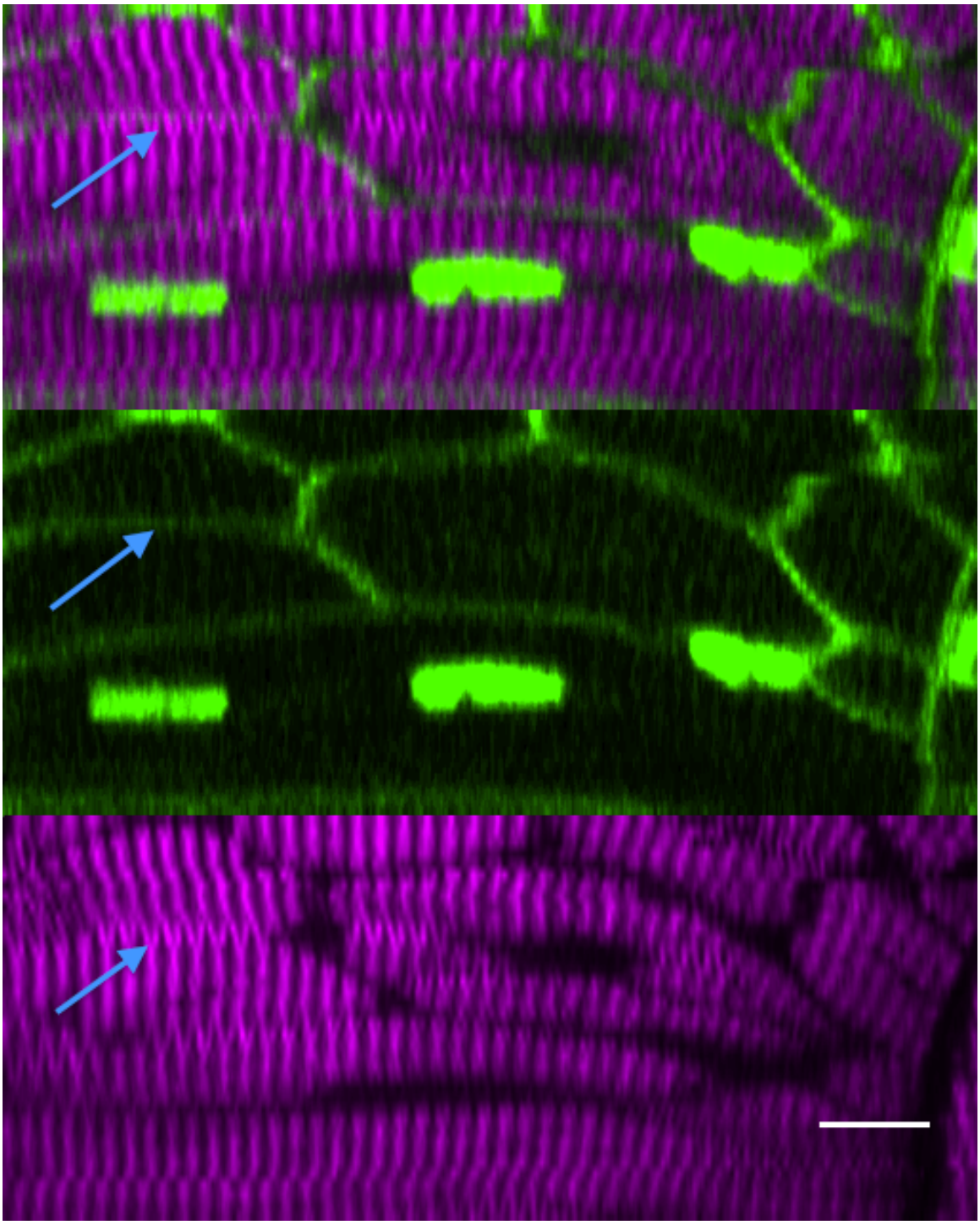

Figure 3.18: Membrane-labeled wildtype zebrafish. Bottom, SHG in purple. Middle, fluorescent membranes and nuclei in green. Top, overlay showing SHG patterns apparently crossing the membrane, which must be an optical artifact, because the myosin filaments align perpendicularly to the SHG stripes. Scale bar is 10 microns. The arrows are guides for the eye, indicating just one example where the pattern appears to cross the membrane.

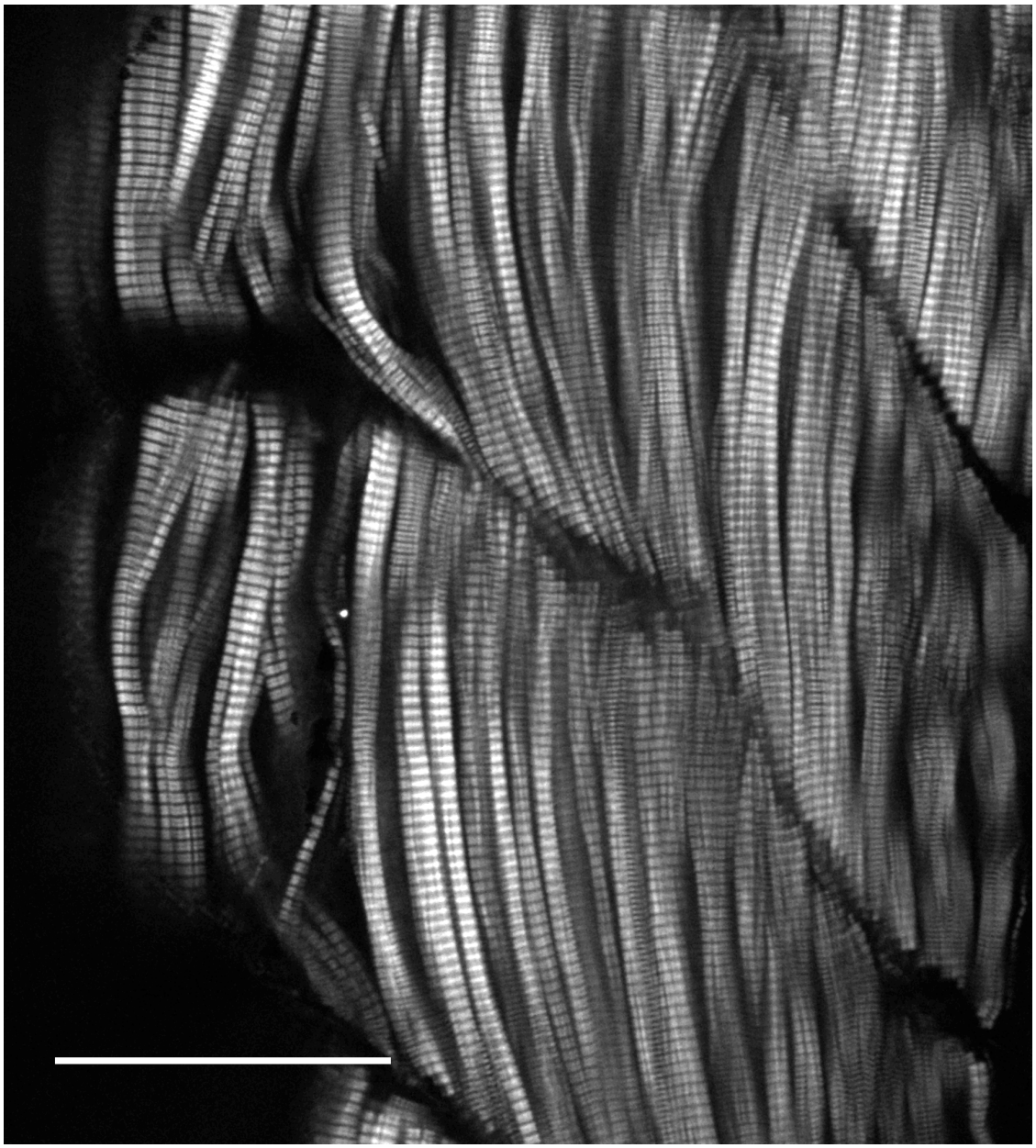

Figure 3.19: Second harmonic generation from zebrafish morphant muscle. Section along sagittal plane. The bright dot left of center appears to be a muscle fragment running perpendicular to the imaging plane, ascertained by optical sectioning (not shown). Scale bar is 50 microns

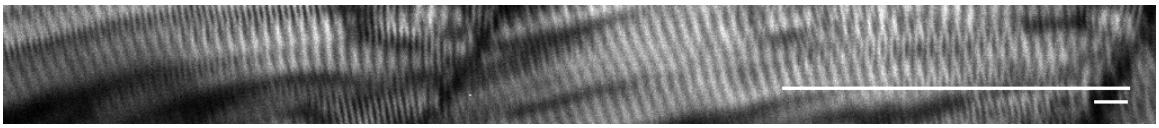

(a) wildtype

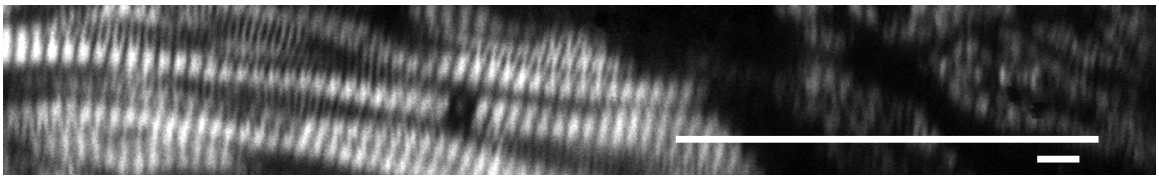

(b) morphant

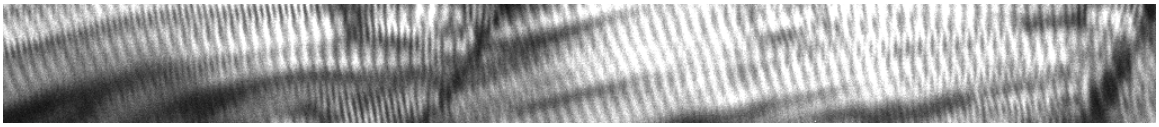

(c) wildtype - raw data

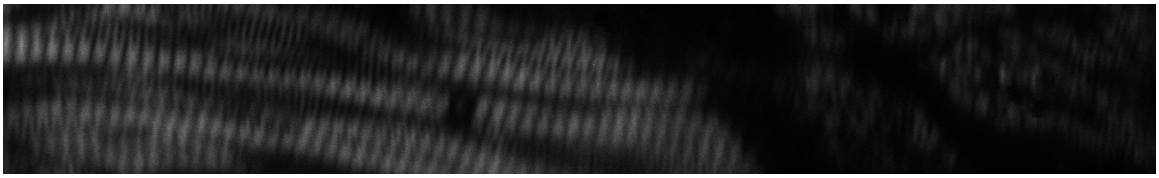

(d) morphant - raw data

Figure 3.20: Comparison of sagittal sections between (a) wildtype and (b) morphant. The morphant is much dimmer, as well as being less densely packed with muscle. Note the disrupted patterns on the right side of (b), evidence of the structural degradation due to the induced muscular dystrophy. (c) and (d) are identical images to (a) and (b), but without any brightness-contrast adjustments, to illustrate the intensity difference between the wildtype and morphant muscle. However, (a) is taken at 890 nm, while (c) and (b)/(d) are taken at 860 nm. Saturation in (c) makes visual comparison of morphology difficult. The average intensity of (c) is 18,668, including saturated pixels. The average intensity of (d) is 7,493. Long scale bar is 50 microns. Short scale bar is 5 microns.

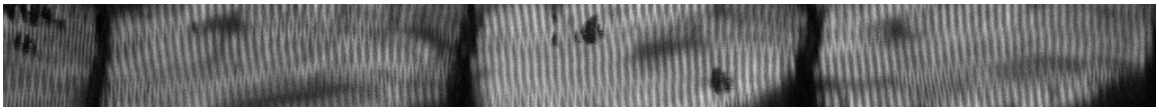

(a) 5-day wildtype coronal section

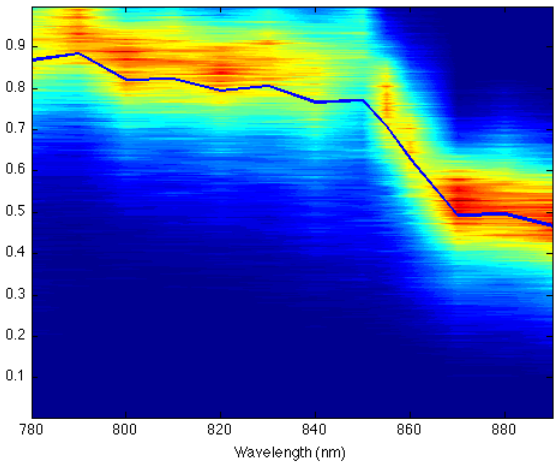

(b) SHG intensity density map

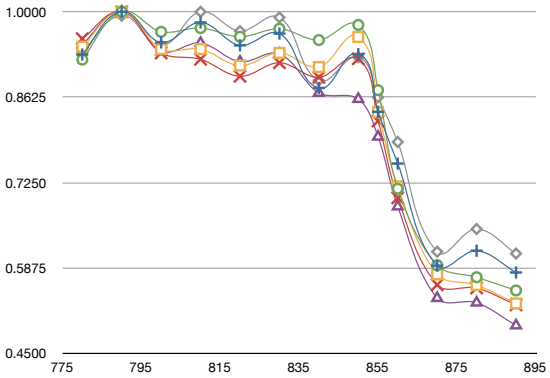

(c) Normalized spectra from representative points

Figure 3.21: The wavelength dependent SHG detected from a single sagittal plane of 5-day old zebrafish, shown in (a), shows a marked drop-off at 850 nm. (b)The density map indicates that the vast majority of spectra display a characteristic behavior. The blue line is the average of normalized spectra, and (c) sampled spectra from a few representative points illustrates their similarity. The black spots in (a) are laser ablation damage, but they do not alter the spectra of neighboring muscle.

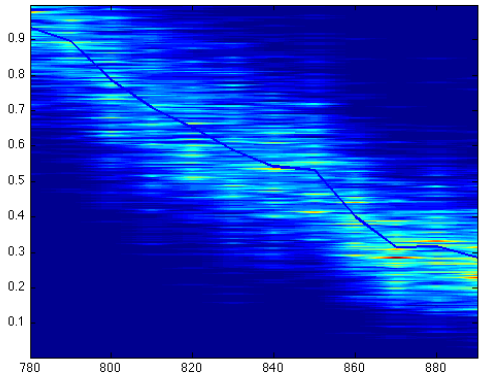

Figure 3.22: Normalized intensity spectrum density map of points from figure 3.21 of low-intensity background points.

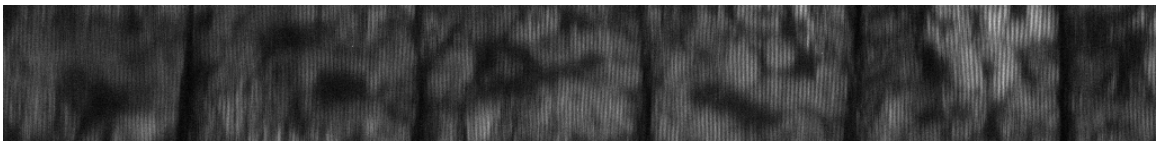

(a) 5-day morphant coronal section

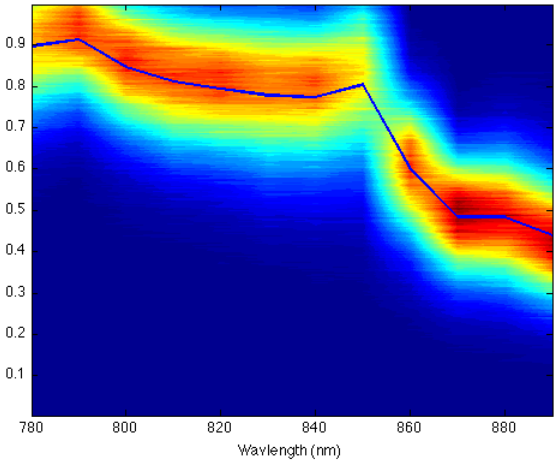

(b) SHG intensity density map

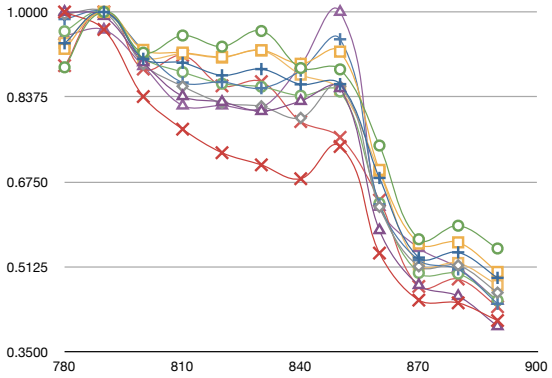

(c) Normalized spectra from representative points, both dim and bright

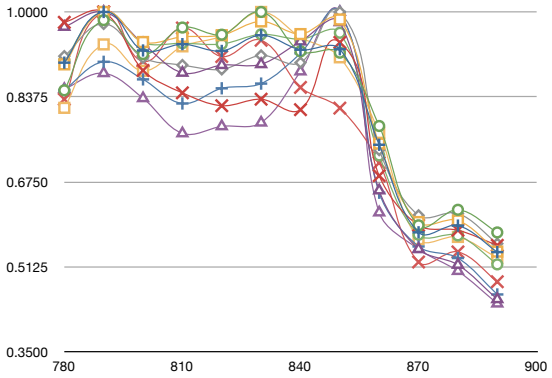

(d) Representative points with subtracted background

Figure 3.23: The wavelength dependent SHG detected from a single coronal plane of 5-day old morphant zebrafish, shown in (a), shares the drop-off at 850 nm with the wildtype spectra (figure 3.21). (b) The characteristic spectra of the morphant differs slightly. The blue line is the average of normalized spectra, and (c) sampled spectra from a few representative points. (d) The same representative points but subtracting an estimated background spectrum.

Chapter 4

Theory of Second Harmonic Generation from Zebrafish Muscle

The observations of fascinating featues of SHG from zebrafish muscle in the previous chapter may be put into context and explained by utilizing the theory of nonlinear optics. In this chapter, we will theoretically explore SHG, and, in particular, develop an understanding of the data. In addition, we suggest further experiments which could be done to validate some of the hypothesis laid out in the present chapter.

4.1 Foundations of Nonlinear Optics

Maxwell's equations, on a classical microscopic level, capture the dynamics of all free and bound charges [133]. However, because the electric field varies extremely rapidly over atomic length scales, the microscopic description loses relevance when considering macroscopic problems, such as the interaction of light with matter. The bound charges in matter react to external electrical fields by rapidly rearranging, resulting in a polarization field produced in response to the applied field. Because the bound charges' motion are constrained by their neighboring electrons and protons,

which are also moving, the material response is extremely complex in microscopic detail. Fortunately, it tends to be characteristic of the material in question. In practice, this is addressed by averaging out the variations over atomic length scales, producing the macroscopic Maxwell's equations:

$$\nabla \cdot \mathbf{D} = \rho_f \tag{4.1a}$$

$$\nabla \cdot \mathbf{B} = 0 \tag{4.1b}$$

$$\nabla \times \mathbf{E} = -\frac{\partial \mathbf{B}}{\partial t} \tag{4.1c}$$

$$\nabla \times \mathbf{H} = \mathbf{J}_f + \frac{1}{c^2}\frac{\partial \mathbf{D}}{\partial t}, \tag{4.1d}$$

where $\mathbf{D} = \epsilon_0 \mathbf{E} + \mathbf{P}$ is the displacement field, $\mathbf{E}$ is the native field due to free charges or applied external fields, $\mathbf{P}$ is the polarization field created by matter responding to $\mathbf{E}$. The magnetic field due to $\mathbf{E}$ and induced magnetization of the material due to $\mathbf{H}$ play a minimal role in this work, and the reader is referred to excellent texts such as Jackson [133] for further exploration, but we will confine ourselves to the case where $\mathbf{B} = \mu_0 \mathbf{H}$. Furthermore, this work is concerned only with how bound charges respond to externally applied fields, so we take $\rho_f = 0$ and $\mathbf{J}_f = 0$.

The wave-equation is constructed by taking the curl of eq. (4.1c) and substituting into equation 4.1d. The resulting equation, $\nabla \times \nabla \times \mathbf{E} + \frac{\partial \mathbf{D}}{\partial t} = 0$, is converting into the wave equation by employing the vector identity $\nabla \times \nabla \times \mathbf{E} = \nabla(\nabla \cdot \mathbf{E}) - \nabla^2 \mathbf{E}$, and taking $|\nabla(\nabla \cdot \mathbf{E})| \ll |\nabla^2 \mathbf{E}|$ [113]:

$$\nabla^2 \mathbf{E} - \frac{1}{c^2}\frac{\partial^2 \mathbf{E}}{\partial t^2} = \frac{1}{c^2}\frac{\partial^2 \mathbf{P}}{\partial t^2}. \tag{4.2}$$

The polarization, $\mathbf{P}$, is due to the response of the underlying matter to the applied external field, $\mathbf{E}$, which may be expanded as

$$\begin{aligned}\mathbf{P}(t)/\epsilon_0 = \mathbf{P}_0 &+ \int_{-\infty}^{\infty} \chi^{(1)}(\omega', \omega_1) : \mathbf{E}(\omega_1) e^{-i\omega' t}\, d\omega_1 \\ &+ \iint_{-\infty}^{\infty} \chi^{(2)}(\omega', \omega_1, \omega_2) : \mathbf{E}(\omega_1)\mathbf{E}(\omega_2) e^{-i\omega' t}\, d\omega_1 d\omega_2 + \cdots \\ &+ \int \cdots \int_{-\infty}^{\infty} \chi^{(n)}(\omega', \omega_1, \ldots, \omega_n) : \mathbf{E}(\omega_1) \cdots \mathbf{E}(\omega_2) e^{-i\omega' t} \prod_i^n d\omega_i \ \ldots,\end{aligned} \tag{4.3}$$

where the colon indicates a tensor product and $\mathbf{P}_0$ is the static polarization, often found at surfaces or in ferroelectrics, and $\omega' = \omega_1 + \cdots + \omega_n$, where n is the order of the term in the expansion. This is often written with the shorthand notation $\mathbf{P}(\mathbf{E}) = \epsilon_0\{\mathbf{P}_0 + \chi^{(1)}\mathbf{E} + \chi^{(2)}\mathbf{E}^2 + \ldots\}$.[1] Because polarizability also acts as a source of electric field, see eq. (4.2), we expand the frequency components of the electric field in orders, $\mathbf{E}(\omega) = \mathbf{E}^{(1)}(\omega) + \mathbf{E}^{(2)}(\omega) + \ldots$, where each order is the contribution of the n^{th}-order nonlinear process. Thus, each order of nonlinearity has a corresponding wave equation. Assuming negligible conversion from higher order modes to lower

[1] Although this power series expansion is formally correct, it is only meaningful when it can be truncated. For this to be true, the terms must rapidly vanish, and this may not be the case under some conditions, such as in laser-induced breakdown ionization [125] or even under intense near-field optics [113]. The maximum peak intensity of the incoming field correspond to to electron binding energies, $I_{atom} \sim \frac{ce}{\epsilon_0 a_0^2} \sim 10^{15}$ W/cm^2. Once the incoming laser intensities reach this order of magnitude, perturbative expansions do not capture the full flavor of the nonlinear processes.

order modes,[2] the n$^{\text{th}}$-order wave equation is given by

$$\nabla^2\mathbf{E}^{(n)}(\omega) - \frac{1}{c^2}\frac{\partial^2}{\partial t^2}\mathbf{E}^{(n)}(\omega) = \frac{1}{c^2}\frac{\partial^2}{\partial t^2}\chi^{(1)}(\omega)\mathbf{E}^{(n)}(\omega) + \frac{1}{c^2}\frac{\partial^2}{\partial t^2}\chi^{(n)}(\omega)\mathbf{E}(\omega_1)\mathbf{E}(\omega_2)\ldots$$
$$\nabla^2\mathbf{E}^{(n)}(\omega) - \frac{n_\omega^2}{c^2}\frac{\partial^2}{\partial t^2}\mathbf{E}^{(n)}(\omega) = \frac{1}{c^2}\frac{\partial^2}{\partial t^2}\chi^{(n)}(\omega)\mathbf{E}(\omega_1)\mathbf{E}(\omega_2)\ldots, \tag{4.4}$$

where n_ω^2 is the squared index of refraction, coming from $n_\omega^2 = \mu_r(1+\chi^{(1)}(\omega))$ and $\mu_r = 1$. The susceptibility's dependence on incoming frequencies has been suppressed for convenience. When the incoming radiation consists of a single monochromatic plane wave, $\mathbf{E} \propto \cos(\omega t - kx)$, we can see that the n$^{\text{th}}$-order nonlinearity will mix the positive and negative frequency components together to produce output frequencies that are both higher and lower than the fundamental. For example, in the second-order case, $P^{(2)} \propto \frac{1}{2}(\cos(2\omega t - 2kx) + 1)$, so there will be induced second harmonic generation and an optically induced dc field (optical rectification). When the two incoming fields are different frequencies, in addition to SHG and optical rectification, there will be sum frequency generation ($\omega' = \omega_1 + \omega_2$) and difference frequency generation ($\omega' = \omega_1 - \omega_2$). At higher orders, even more combinations are possible, leading to an entire catalog of possible nonlinear optical effects [134].

Returning to the example of second harmonic generation from monochromatic plane waves, the second-order nonlinear wave equation becomes

$$\nabla^2\mathbf{E}^{(n)}(\omega) - \frac{n_\omega^2}{c^2}\frac{\partial^2\mathbf{E}^{(n)}(\omega)}{\partial t^2} + cc = -\frac{2\omega_1^2}{c^2}\chi^{(2)}E_0^2 e^{-2i(\omega_1 t - k_\omega x)} + cc, \tag{4.5}$$

[2]This is true within the scope of the present work, but not in general.

where cc stands for the complex conjugate of the preceding terms. Because of the linearity of the equation, we have $\omega = 2\omega_1$, and a solution of the form $E(2\omega_1, x) = A(x)e^{-i(2\omega_1 t - k_{2\omega_1} x)} + cc$. This leads to

$$\frac{\partial^2}{\partial x^2}A(x) - ik_{2\omega_1}\frac{\partial}{\partial x}A(x) + cc = -\frac{2\omega_1^2}{c^2}\chi^{(2)}E_0^2 e^{i\Delta k x} + cc, \tag{4.6}$$

where $\Delta k = 2k_{\omega_1} - k_{2\omega_1} = 2\omega(n_{\omega_1} - n_{2\omega_1})/c$. Δk is the deviation from perfect phase-matching. When $\Delta k \neq 0$, the fundamental and harmonic waves do not travel at the same speed, so the harmonic waves being to interfere with themselves. Taking $A(0) = \partial_x A(0) = 0$, meaning $A(x)$ represents the amplitude of the SHG produced after the fundamental mode is incident on a uniform slab of SHG-producing material, eq. (4.6) has a solution given by

$$A(x) = \frac{2\omega_1^2}{c^2}\chi^{(2)}E_0^2\frac{k_{2\omega_1}(1 - e^{i\Delta k x}) - \Delta k(1 - e^{-ik_{2\omega_1}x})}{\Delta k k_{2\omega_1}(\Delta k + k_{2\omega_1})}.$$

The intensity of the resulting SHG is given by $n_{2\omega_1}(\epsilon_0/\mu_0)^{\frac{1}{2}}|A(x)|^2/2$, so, assuming $\Delta k \ll k_{2\omega_1}$, we obtain [134, 113]

$$I_{2\omega_1}(x) = \frac{\omega_1^2}{4c^3\epsilon_0}\frac{|\chi^{(2)}(\omega_1)|^2}{n_{\omega_1}^2 n_{2\omega_1}}I_{\omega_1}^2\, x^2 \mathrm{sinc}^2(\Delta k x/2), \tag{4.7}$$

where sinc is $\sin(x)/x$. This relationship illustrates the importance of phase-matching in creating SHG. As shown in figure 4.1, the size of the underlying SHG-active material makes a significant contribution to the overall SHG production efficiency.[3] However,

[3]We recover the interesting relationship that SHG production is only significant when $x\Delta k < \pi$,

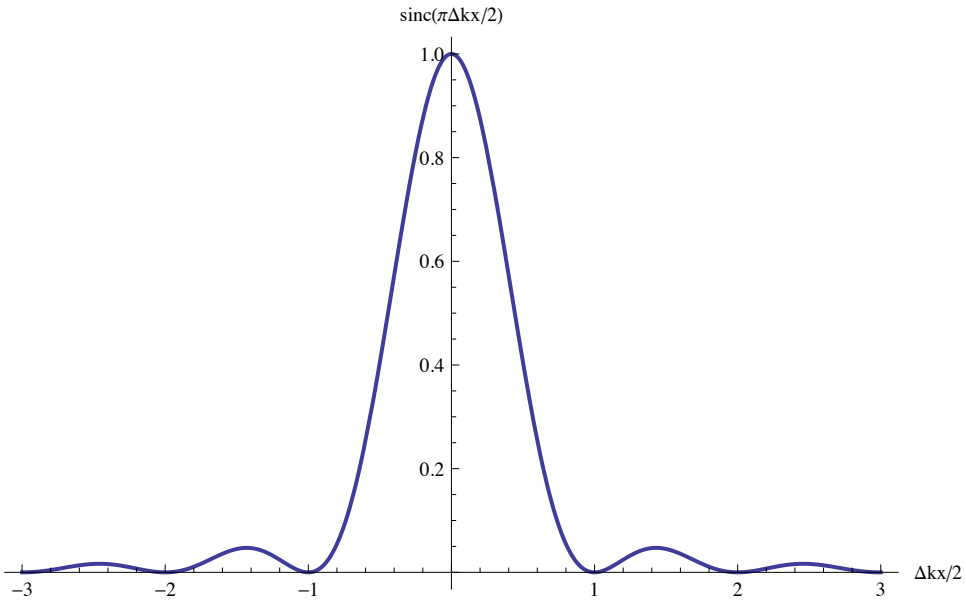

Figure 4.1: Second harmonic generation production efficiency depends on the magnitude of the phase-matching, Δk, determined by eq. (4.7). Absent perfect phase-matching, corresponding to $\Delta k = 0$, SHG can only be produced across a distance constrained by $\Delta k \Delta x < 2\pi$.

eq. (4.7) only holds for monochromatic plane waves. In practice, our experiments employ focused beams, which can significantly alter the phase-matching relations, and this will be more thoroughly explored in Section 4.2.

4.2 SHG Phase-Matching with Focused Light

Muscle fibers are significantly larger than the wavelength of light, as shown in figure 3.7, and the myofibrils are on order one wavelength. From eq. (4.7), only media much smaller than the wavelength of light escape the effects of phase-matching.

an analogy to the Heisenberg uncertainty principle, $\Delta x \Delta p > \hbar/2$, although the current result originates from harmonic analysis. Given this analogy, we can explore the concept that SHG production is limited by the conservation of momentum mismatch resulting from the fusion of two photons into one. In the absence of perfect phase-matching, the outgoing photon will not conserve momentum. However, over very short distances, there is sufficient uncertainty in momentum to compensate for this. In addition, conceptually, vibrational quanta created by periodic order in the material can contribute or withdraw momentum to assist with momentum conservation.

However, focused light has a Guoy phase, an extra twist of phase that occurs at the focus [113]. In addition, focused light approaches the focus from different angles, giving more possible combinations for phase-matching. These effects can significantly alter the total phase-matching balance, a crucial factor to include in any theory of wavelength dependent SHG microscopy.

The susceptibility tensor for myosin, $\chi^{(2)}_{ijk}$, has a number of restrictions due to the underlying symmetry of the protein structures [129], leaving only two independent terms, $\chi^{(2)}_{xxy} = \chi^{(2)}_{xyx} = \chi^{(2)}_{zyz} = \chi^{(2)}_{zzy} = \chi^{(2)}_{yzz} = \chi^{(2)}_{yxx}$ and $\chi^{(2)}_{yyy}$. Experiments have determined $\chi^{(2)}_{yyy} < \chi^{(2)}_{yxx}$. However, we leave analyses of the tensor components to previous works [121, 106, 101, 129, 86]. In general, we will not need to consider the tensor nature of SHG, because the area of interest, the laser focus, is so small. In addition, we have chosen the alignment of the fish with the laser to be such that the SHG power is large. Taking the myosin to run along the y-axis, we set the polarization to be approximately perpendicular to y. Because the light is propagating in the z-direction, and therefore has minimal vector components in z, we have essentially set up the experiment to probe a single tensor component, $\chi^{(2)}_{yxx}$.

4.2.1 The Paraxial Approximation of the Wave Equation

Consider the wave equation, $(\nabla^2 - \frac{n^2}{c^2}\partial_t^2)\mathbf{E} = 0$. The electric field is fundamentally a vector, which evolves in magnitude and orientation over space and time. Represent the electric field propagating in the $\hat{k}$ direction as $\mathbf{E}(\mathbf{r}) = \mathbf{A}(\mathbf{r})\exp(-i\omega t + i\mathbf{k}\cdot r)$. After decomposing the Laplacian into a transverse component and a radial component,

$\nabla^2 = \nabla^2_{\hat{k}} + \nabla^2_T$, we substitute both expressions into the wave equation, obtaining the quantity

$$\nabla^2 \mathbf{A}(\mathbf{r}) \exp(i\mathbf{k}\cdot\mathbf{r}) = \exp(i\mathbf{k}\cdot\mathbf{r}) \left(\nabla^2_T \mathbf{A}(\mathbf{r}) + 2i\mathbf{k}\cdot\mathbf{r}\, \nabla_{\hat{k}} \mathbf{A}(\mathbf{r}) + \nabla^2_{\hat{k}} \mathbf{A}(\mathbf{r}) \right).$$

If $|\mathbf{k}\cdot\mathbf{r}\, \nabla_{\hat{k}} \mathbf{A}(\mathbf{r})| \gg |\nabla^2_{\hat{k}} \mathbf{A}(\mathbf{r})|$, meaning the envelope of the electric field varies slowly over the scale of a wavelength in the direction of propagation, the second-order term may be neglected, which is called the paraxial approximation [133]. This approximation is well suited for focused light, but it begins to break down when the NA exceeds approximately 1 [135, 136, 137]. Although, the paraxial approximation has been shown to be lacking in accuracy for the angular radiation pattern of SHG [135], it has performed well for predicting the total power produced [138, 139, 140].

Given the paraxial approximation, one may describe a focused laser, propagating in the z-axis, using a Gaussian envelope,

$$A(r,z) = \frac{A_0}{1+i\xi} \exp\left[-\frac{r^2}{w_0^2(1+i\xi)} \right], \tag{4.8}$$

where we have adopted the notation of [113], and we define $\xi = 2z/b$, where b is the confocal parameter, $b = kw_0^2$, and w_0 is the radius of the beam at the focus. The nonlinear wave equation for SHG under the paraxial approximation gives

$$2ik_2 \frac{\partial A_2}{\partial z} + \nabla^2_T A_2 = -2\pi \frac{\omega^2}{c^2} \chi^{(2)} A(r,z) e^{-i\Delta k z}, \tag{4.9}$$

where ω is the fundamental frequency, A_2 is the resulting SHG mode, k_2 is the wavenumber at 2ω, $k_2 = 2n_{2\omega}\omega/c$, and the phase mismatch is $\Delta k = 2\frac{\omega}{c}(n_\omega - n_{2\omega})$. The solution to eq. (4.9) is given by

$$A_2(r,z) = i\frac{2\omega}{n_{2\omega}c}\chi^{(2)}A_0^2 J_2(\Delta k, z_0, z)\frac{\exp\left[-2\frac{r^2}{w_0^2(1+i\xi)}\right]}{1+i\xi}, \tag{4.10}$$

where

$$J_2(\Delta k, z_0, z_f) = \int_{z_0}^{z_f} \frac{e^{i\Delta k z'}}{1+2iz'/b}\, dz', \tag{4.11}$$

where z_0 is the z-coordinate of the beginning of the SHG medium, relative to the focus at $z = 0$ [113, 141]. This integral, which reduces to the identical form of eq. (4.7) when $z_0 - z_f \ll b$, determines the altered phase-matching conditions of the focused beam. As the limits of the integral in eq. (4.11) expand to infinity, J_2 takes the asymptotic form $J_2 = \{0, \Delta k \leq 0; \frac{b}{2}\exp(-b\Delta k/2), \Delta k > 0\}$ [113]. Even when the bounds are well short of the asymptotic limit, the integral is very sensitive to Δk and to the width of the medium, shown in figure 4.2.

4.2.2 SHG from Periodic Media

Derivations such as eq. (4.8) assign no explicit spatial dependence to the SHG susceptible medium. Most crystals are uniform at super-atomic lengths, but muscles, as described in section 3.1, are packed into multiscale structures, interleaving SHG and nonSHG active regions. Hence, it would be most appropriate to describe the

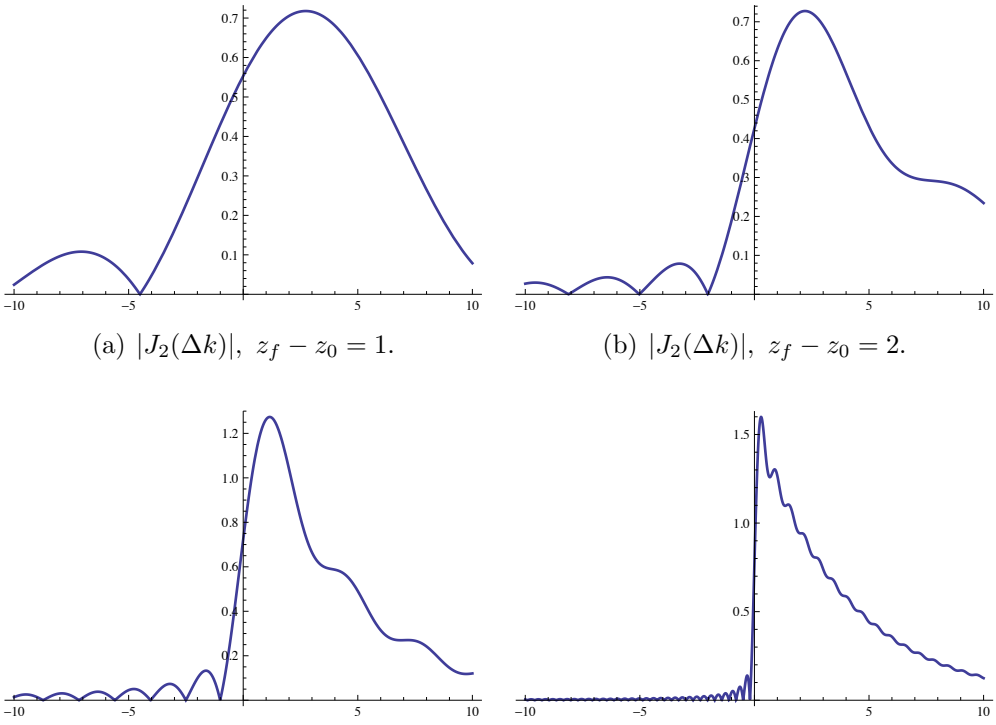

(a) $|J_2(\Delta k)|,\ z_f - z_0 = 1.$ (b) $|J_2(\Delta k)|,\ z_f - z_0 = 2.$

(c) $|J_2(\Delta k)|,\ z_f - z_0 = 4.$ (d) $|J_2(\Delta k)|,\ z_f - z_0 = 20.$

Figure 4.2: With a focused beam, the conversion efficiency is very sensitive to the magnitude and sign of the phase-matching, Δk, as well as the width of the medium, $z_f - z_0$. $b = 0.5$

susceptibility with some sort of spatial regularity, i.e.,$\chi^{(2)}(r)$.[4] We insert $\chi^{(2)}(\mathbf{r})$ into the nonlinear wave equation and expand in a Fourier series:

$$\begin{aligned}\nabla^2 A_2 - \frac{n_{2\omega}^2}{c^2}\frac{\partial^2}{\partial t^2}A_2 &= -2\pi\frac{\omega^2}{c^2}A^2(r,z)\chi^{(2)}(r)e^{-i\Delta kz} \\ &= -2\pi\frac{\omega^2}{c^2}A^2(r,z)\chi_0^{(2)}\sum_{lmn}G_{lmn}e^{-i(\Delta k+K_{lmn})\cdot\mathbf{r}}, \end{aligned} \tag{4.12}$$

where $\mathbf{K}_{lmn}$ are the reciprocal lattice vectors of the SHG photonic crystal, G_{lmn} is the complex amplitude of each Fourier component, and $l, m,$ and n are integers [142]. eq. (4.12) demonstrates that periodicity alters the phase-matching relationship into $\Delta\mathbf{k}' = \Delta\mathbf{k} + \mathbf{K}_{lmn}$. The resulting quasi-phase-matching allows multiple radiation directions, for each solution of

$$\mathbf{k}_2 = 2\mathbf{k}_1 - \mathbf{K}_{lmn}, \tag{4.13}$$

which is consistent with the model that the periodic structure can add or subtract phonons to conserve momentum [143, 144]. The resulting angle will be given by

$$\cos\theta_{lmn} = 2\frac{k_1}{k_2} + \frac{\hat{k}_1\cdot\mathbf{K}_{lmn}}{k_2} \tag{4.14}$$

$$= \frac{n_\omega}{n_{2\omega}} + \frac{\lambda}{2n_{2\omega}a}\hat{k}_1\cdot\mathbf{K}'_{lmn}, \tag{4.15}$$

[4]Muscle is not merely periodic in its SHG susceptibility, but protein has a different index of refraction than water. Thus, there is a second spatial component, $n_{2\omega} = \sum N_{lmn}\exp(-\mathbf{K}_{lmn}\cdot\mathbf{r})$, which has identical lattice vectors. However, the difference in refractive index is small, while the difference in SHG susceptibility is large, so we may neglect the former.

where θ_{mn} is the angle formed between k_1 and k_2, $\hat{k}_1$ is the unit vector oriented in the direction of propagation of the fundamental wave, and a is the characteristic length scale of the periodic structure.

For example, in a 2D-hexagonal crystal of circular rods, which has only two indices, m and n, the lattice is defined by two vectors, $(0, a)$ and $(\sqrt{3}a/2, a/2)$, where a is the spacing between neighboring elements. These two vectors form a parallelogram outlining the unit cell, shown in figure 3.6, and have the Fourier components given by [145]:

$$G_{mn} = \frac{2r}{a\sqrt{m^2+n^2+mn}} J_1\left(\frac{4\pi r}{\sqrt{3}a}\sqrt{m^2+n^2+mn}\right), \text{ and} \tag{4.16}$$

$$\mathbf{K}_{mn} = \frac{2\pi}{a}\left(\frac{1}{\sqrt{3}}(m+2n), m\right), \tag{4.17}$$

where r is the radius of the circular rod and J_1 is the first Bessel function. Assuming the laser enters the crystal at an angle ϕ, so $\hat{k}_1 = (\cos\phi, \sin\phi)$, eq. (4.14) becomes

$$\cos\theta_{mn} = \frac{n_\omega}{n_{2\omega}} + \frac{\lambda}{2n_{2\omega}a}\left(m\cos\phi + \frac{1}{\sqrt{3}}(m+2n)\sin\phi\right). \tag{4.18}$$

Sometimes no phase-matching conditions are readily apparent. However, it may be the case that phase-matching may be obtained by the outgoing SHG having a angular distribution that cannot be readily derived by the paraxial approximation. To account for this, and to study nontrivial geometries, we turn to a Green's function approach to calculating SHG. Because the nonlinear polarization acts as a source term in the wave equation, we sum the contribution from each point in the SHG

medium [146]

$$\mathbf{E}_{2\omega}(\mathbf{r}) = \int G(\mathbf{r},\mathbf{r}')\mathbf{P}_{NL}(\mathbf{r}')\,d\mathbf{r}' \tag{4.19}$$

$$= \int G(\mathbf{r},\mathbf{r}')\sum_{jk}\chi^{(2)}_{ijk}(\mathbf{r}')E_j(\mathbf{r}')E_k(\mathbf{r}')\,d\mathbf{r}', \tag{4.20}$$

where $G(\mathbf{r},\mathbf{r}')$ is the Green's function, which, technically, depends on the specific boundary conditions. Although this is a very general expression, we are only really concerned about radiation in the far field, and, because only light collected by the condenser reaches the detector, we are concerned with the angular dependence of the radiation intensity. This simplifies the expression of the Green's function to be approximately independent of near-field boundary conditions [133], and eq. (4.20) at a far-field distance R becomes [147, 140]

$$\mathbf{E}_{2\omega}(\Omega,\mathbf{r}_0) = \left[\hat{\theta},\hat{\phi}\right]\cdot\frac{\omega^2}{c^2}\frac{e^{ik_{2\omega}R}}{4\pi R}\sum_{jk}\int\chi^{(2)}(\mathbf{r}')E_j(\mathbf{r}'-\mathbf{r}_0)E_k(\mathbf{r}'-\mathbf{r}_0)e^{-ik_{2\omega}\mathbf{r}'\cdot\hat{\mathbf{r}}}\,d\mathbf{r}', \tag{4.21}$$

where the spherical unit vectors are given by

$$\hat{\theta} = \cos\theta\cos\phi\hat{\mathbf{x}} + \cos\theta\sin\phi\hat{\mathbf{y}} - \sin\theta\hat{\mathbf{z}} \tag{4.22a}$$

$$\hat{\phi} = -\sin\phi\hat{\mathbf{x}} + \cos\phi\hat{\mathbf{y}} \tag{4.22b}$$

$$\hat{\mathbf{r}} = \sin\theta\cos\phi\hat{\mathbf{x}} + \sin\theta\sin\phi\hat{\mathbf{y}} + \cos\theta\hat{\mathbf{z}}, \tag{4.22c}$$

meaning the $\hat{\theta}$ and $\hat{\phi}$ components contain the angular dependence of the radiated SHG, while $\hat{\mathbf{r}}$ is the unit vector directed toward the detector at the specified solid

angle, Ω. The laser is centered at $\mathbf{r}_0$ and radiating in the z-axis, meaning $\hat{k}_\omega = \hat{\mathbf{z}}$. We will take the electric field to be polarized in an arbitrary $\hat{\mathbf{u}}$ direction and to be a Gaussian mode,

$$\mathbf{E}_\omega = \hat{\mathbf{u}} E_0 \frac{\exp\left[-\frac{x^2+y^2}{w_0^2(1+i\xi)}\right]}{1+i\xi} e^{ik_\omega z}.$$

Because we normalized the incoming total power, we have $E_0 = \sqrt{\mathcal{P}/(n_\omega^2 b)}$, where $\mathcal{P}$ is the power detected at the back aperture of the objective. Using the Gaussian mode, we may further specify our expression for angular SHG to

$$\mathbf{E}_{2\omega}(\Omega, \mathbf{r}_0) = \left[\hat{\theta}, \hat{\phi}\right] \cdot \frac{\omega^2}{c^2} \frac{e^{ik_{2\omega}R}}{4\pi R} \sum_{jk} \hat{\mathbf{x}}_j \cdot \hat{\mathbf{u}}\, \hat{\mathbf{x}}_k \cdot \hat{\mathbf{u}} \int \chi^{(2)}(\mathbf{r}') \times \frac{\mathcal{P}}{n_\omega^2 b} \exp\left[-2\frac{(x-x_0)^2+(y-y_0)^2}{w_0^2\,(1+2i(z-z_0)/b)}\right] \frac{e^{i2k_\omega(z-z_0)-ik_{2\omega}\mathbf{r}'\cdot\hat{\mathbf{r}}}}{(1+2i(z-z_0)/b)^2}\, d\mathbf{r}', \qquad (4.23)$$

where $\hat{\mathbf{x}}_j \cdot \hat{\mathbf{u}}$ is the projection of the polarization vector onto the various Cartesian unit vectors.

From this point on, we will assume the incoming light is purely polarized in $\hat{\mathbf{x}}$ and perpendicular to the long axis of the myosin fibers. This means there is only one nonzero tensor component, χ_{yxx}, so the output light is $\hat{\mathbf{y}}$ polarized, which leads the $\hat{\theta}$ and $\hat{\phi}$ components to be proportional to $\cos\theta \sin\phi$ and $\cos\phi$, respectively. The power per unit solid angle will be proportional to $(\cos^2\theta \sin^2\phi + \cos^2\phi)|\int \cdots|^2$, and the total power detected is found by integrating the power density over all ϕ and the range of θ which is contained within the condenser optic's acceptance angle, namely $\theta_{\max} \sim \sin^{-1}(0.55/1.4) \sim 20^\circ$.[5]

[5]The condenser has a numerical aperture of 0.55. Numerical aperture is defined as $NA = n\sin\theta$, where n is the refractive index of the immersion medium (air for the condenser). The SHG originates

Although eq. (4.23) may be integrated directly, for some geometries it is more convenient to work in the conjugate space. Consider the Fourier transform pair of $\chi(x)$:

$$\chi^{(2)}(\mathbf{q}) = \int \tilde{\chi}^{(2)}(\mathbf{r}) e^{-i\mathbf{q}\cdot\mathbf{r}}\, d\mathbf{r}$$
$$\chi^{(2)}(\mathbf{r}) = \frac{1}{(2\pi)^3} \int \tilde{\chi}^{(2)}(\mathbf{q}) e^{i\mathbf{q}\cdot\mathbf{r}}\, d\mathbf{q}.$$

Substituting the latter expression into eq. (4.23) gives the relation

$$\mathbf{E}_{2\omega}(\Omega, \mathbf{r}_0) \propto [\cos\theta \sin\phi, \cos\phi] \cdot \frac{\omega^2}{c^2} \chi_{yxx} \iint \tilde{\chi}^{(2)}(\mathbf{q}) \times \frac{1}{n_\omega^2 b} \exp\left[-2\frac{(x-x_0)^2 + (y-y_0)^2}{w_0^2\,(1 + 2i(z-z_0)/b)}\right] \frac{e^{i2k_\omega(z-z_0)}}{(1+2i(z-z_0)/b)^2} e^{-i(k_{2\omega}\hat{\mathbf{r}} - \mathbf{q})\cdot\mathbf{r}'}\, d\mathbf{r}'\, d\mathbf{q}, \tag{4.24}$$

where we have dropped factors that will not contribute any wavelength dependence.

Having interchanged the order of integrals, we see the spatial integral is equivalent to a Fourier transform of the incoming Gaussian waveform, given by

$$\begin{aligned}
&\int \frac{1}{n_\omega^2 b} \exp\left[-2\frac{(x-x_0)^2 + (y-y_0)^2}{w_0^2\,(1 + 2i(z-z_0)/b)}\right] \frac{e^{i2k_\omega(z-z_0)}}{(1+2i(z-z_0)/b)^2} e^{-i(k_{2\omega}\hat{\mathbf{r}} - \mathbf{q})\cdot\mathbf{r}'}\, d\mathbf{r}' \\
&\quad = \int \frac{1}{n_\omega^2 b} \exp\left[-2\frac{s_x^2 + s_y^2}{w_0^2\,(1 + 2is_z/b)}\right] \frac{e^{i2k_\omega s_z}}{(1+2is_z/b)^2} e^{-i\mathbf{Q}\cdot\mathbf{r_0}} e^{-i\mathbf{Q}\cdot\mathbf{s}} d\mathbf{s} \\
&\quad = \frac{\pi^2}{2} \frac{b}{n_\omega^2 k_\omega} e^{-\frac{1}{2}b(Q_z + 2k_\omega)} \Theta\left[Q_z - \frac{Q_x^2 + Q_y^2 - 8k_\omega^2}{4k_\omega}\right] e^{-i\mathbf{Q}\cdot\mathbf{r_0}},
\end{aligned} \tag{4.25}$$

within the fish muscle, with a refractive index of 1.4. The boundary between muscle/agarose and air will cause the outgoing light to be further bent, so we need to calculate the angle of emission in the agarose corresponding to the maximum acceptance angle in air. Therefore, Snell's law gives $n_{agar} \sin\theta_{\max} = n_{air} \sin\theta = NA$, and, thus we have $\theta_{\max} = \sin^{-1}(0.55/1.4)$. Because the refractive index is wavelength dependent, $\theta_{\max}$ will also have wavelength dependence.

where $\mathbf{Q} = k_{2\omega}\hat{\mathbf{r}} - \mathbf{q}$, and $\Theta[\cdot]$ is the unit-step function, $\Theta(x) = \int_{-\infty}^{x} \delta(u)du$. Expanding, we get

$$
\begin{aligned}
&= \frac{\pi^2}{2}\frac{b}{n_\omega^2 k_\omega}\exp\big[-\frac{1}{2}b(2k_\omega - k_{2\omega}\cos\theta + q_z) \\
&\qquad +i(r_{0z}(q_z - k_{2\omega}\cos\theta) + r_{0x}(q_x - k_{2\omega}\cos\phi\sin\theta) + r_{0y}(q_y - k_{2\omega}\sin\phi\sin\theta))\big]\times \\
&\qquad\quad \Theta\left[-q_z + k_{2\omega}\cos\theta + \frac{-8k_\omega^2 + (q_x - k_{2\omega}\cos\phi\sin\theta)^2 + (q_y - k_{2\omega}\sin\phi\sin\theta)^2}{4k_\omega}\right],
\end{aligned}
\tag{4.26}
$$

which we will abbreviate as $\tilde{\mathcal{G}}(\mathbf{q}, \mathbf{r}_0, \Omega)$. The outgoing electric field can now be written as

$$
\mathbf{E}_{2\omega}(\Omega, \mathbf{r}_0) = [\cos\theta\sin\phi, \cos\phi] \cdot \frac{\omega^2}{c^2}\chi_{yxx}\int \tilde{\chi}^{(2)}(\mathbf{q})\tilde{\mathcal{G}}(\mathbf{q}, \mathbf{r}_0, \Omega)\, d\mathbf{q}. \tag{4.27}
$$

We see that phase-matching is still vital, but the conditions have relaxed, because there is an overall prefactor of $\exp[-\frac{1}{2}b(2k_\omega - k_{2\omega}\cos\theta)]$, shown in eq. (4.26). There may be outgoing directions which provide satisfactory conditions if conventional forward propagation of SHG is poorly matched. This result also explains a common observation of conical radiation in SHG radiation

Myofibrils are very long compared to the focal width of the Gaussian beam, so we can take them to be effectively infinite in extent in the y-direction. In addition, muscles consist of many repeating units. For example, myofibrils are packed full of myosin filaments in a hexagonal fashion. If we take each filament to be a cylinder of radius r_0, denoted as $\Theta(r_0^2 - x^2 - z^2)$, then the entire filament would be a sum of

these cylinders, given by

$$\chi^{(2)}(\mathbf{r}) = \sum_{mn} \Theta(r_0^2 - (x - \Delta x_{mn})^2 - (z - \Delta z_{mn})^2), \tag{4.28}$$

and the corresponding Fourier transform[6] is

$$\tilde{\chi}^{(2)}(\mathbf{q}) = 2\pi r_0 \delta(q_y) \frac{J_1(r_0\sqrt{q_x^2 + q_z^2})}{\sqrt{q_x^2 + q_y^2}} \sum_{mn} e^{-i(\Delta x_{mn} q_x + \Delta z_{mn} q_z)}, \tag{4.29}$$

which reduces to $\tilde{\chi}^{(2)}(\mathbf{q}) = 2\pi r_0 \delta(q_y) \frac{J_1(r_0\sqrt{q_x^2+q_z^2})}{\sqrt{q_x^2+q_y^2}}$ for a single filament. From above, we know $\Delta x_{mn} = n\frac{\sqrt{3}}{2}a$ and $\Delta z_{mn} = (m - n/2)a$.

4.3 Explaining Patterns in Muscle Structure

Second harmonic generation is fundamentally different from fluorescence due to the phase coherence in the harmonic beam, while fluorescent light is incoherent. This primarily influences the radiation direction of second harmonic generation, compared to the isotropic emission in fluorescence. For example, figure 3.3 shows epi-collected fluorescence, i.e.,returning toward the laser source, versus second harmonic, which radiates almost entirely in trans, i.e.,in the same direction as the laser. This phase coherence has additional impact on imaging. Fluorescent signal scales linearly with the number of excited fluorescent molecules in the focus. In contrast, second harmonic generation scales as the square of the number of phase-coherent SHG sources in

[6]Due to the cylindrical symmetry of the geometry, this type of transform is often referred to as a Hankel transform instead of a Fourier transform.

the focus, and SHG produced away from the focus adds coherently to the signal in focus.[7] This phase coherence leads to two prominent motifs in muscle SHG images, as described in section 3.3.1. First, there are the discrete dots, as in figure 3.14. Second, there are the "verniers," or herringbone patterns, as in figure 3.16 and readily apparent in figure 3.18, although they common in almost every image.

To investigate, we first consider a numerical simulation of the SHG microscopy. Consider a numeric map of the susceptibility, simplified for the purposes of the calculation, given by $M(x, z)$, where $\hat{z}$ is the direction of propagation. The value taken on by $M(x, z)$ denotes a effective scalar susceptibility, either 1, 0, or -1 [113]. To construct a hypothetical muscle, we map out myofibrils as discrete rectangles of myosin, whose size and shape mirror the A-bands of sarcomeres. The myosin blocks are arranged in rows, representing myofibrils, depicted in figure 4.3(a). Because myosin thick filaments project from the M-line, which is at the center of the sarcomere, each half sarcomere has oppositely signed susceptibilities,[8] represented by the different colors in figure 4.3(a). The hypothetical myofibrils are arranged in parallel and in phase, building up a myocyte. A second myocyte, placed 180° out of phase is constructed adjacent to the first.

More specifically, let $Sq(x, d)$ be a square wave with period 2π and duty cycle $d\%$, then if $\Delta z < z < \Delta z + w_s$, where $\Delta z = 0.1$ μm is the spacing between sarcomeres

[7] This may have a significant impact on SHG confocal microscopy, because signal produced away from the focus propagates in a Gaussian mode with an identical focus as the fundamental beam, and cannot be excluded with a pinhole. Thus, the success of SHG confocal microscopy is likely explained by the fact that light is fundamentally quantized, and, for biological samples, SHG efficiency drops off sufficiently away from the focus that zero photons are produced.

[8] A fundamental property of second-order nonlinear susceptibility is inversion due to change of parity: $\chi^{(2)}(-x) = -\chi^{(2)}(x)$. If the underlying material possess inversion symmetry, such as at the M-line, we must have $\chi^{(2)} = 0$.

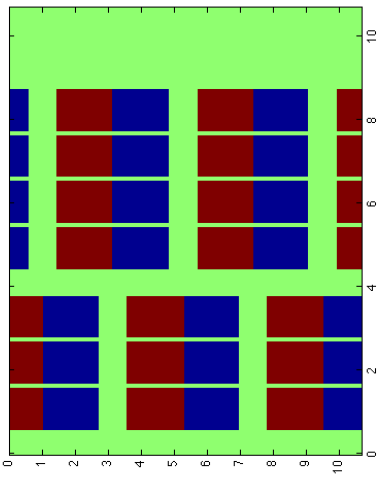

(a) Scheme of two adjacent myofibrils. Color indicates the chirality of the myosin filaments, and the boundary between them is the M-line.

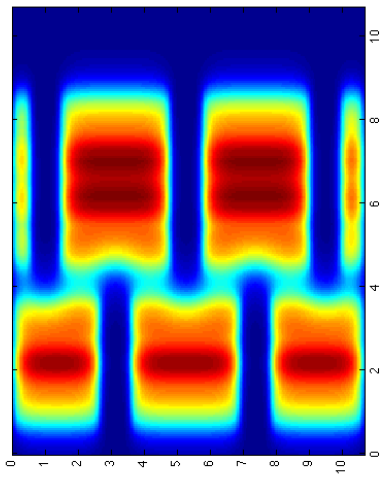

(b) two-photon fluorescence from Only myosin is shown.

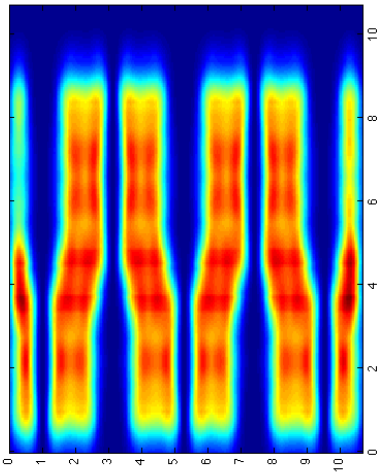

(c) SHG from myosin.

Figure 4.3: Theoretical calculations illustrate the qualitative difference between SHG and two-photon fluorescence. Two hypothetical myofibrils touch, one slightly out of phase with the other. If the myosin were labeled with a fluorescent dye, one would measure discrete points of light, with little or no signal joining the myofibrils. However, the coherent nature of SHG causes the appearance of a contiguous, single myofibril, with a "vernier." In these images, the laser comes propagates vertically, corresponding to an image such as figure 3.18.

and $w_s = 1$ μm is the width of the sarcomere,

$$M(x,z) = \max\left[Sq(2\pi x/p, d), 0\right] Sq(2\pi x/p, d/2), \tag{4.30}$$

where $p = 5$ μm is the length of the sarcomere, and $d = 80\%$. This maps out the susceptibility of a single myocyte, as in figure 4.3(a), assigning each point a susceptibility of 1, -1, or 0. For the second set of fibrils, a phase factor of π is added.

Many biological experiments use fluorescent stains, so we calculate what would be observed if the muscle represented by $M(x,z)$ were imaged using a two photon microscope. The incoming beam is a Gaussian, given by

$$E(x,z) = \frac{\exp\left[-\frac{x^2}{w_0^2(1+i\xi)}\right]}{1+i\xi} e^{ik_\omega z}, \tag{4.31}$$

where w_0, Δk, and ξ are the focal radius, phase mismatch, and normalized Rayleigh distance, as defined in section 4.2.1, evaluated using $\lambda = 0.850$ μm and NA= 0.8. To construct the image, the absolute value of eq. (4.31) is squared and then convolved with the absolute value of $M(x,z)$. The square of this result is proportional to the intensity of fluorescence incident on the detector, and is pictured in figure 4.3(b).

To calculate the SHG produced by this image, we employ the Green's function approach, taken from eq. (4.23). In this case, we only care about the field collected by the detector, so, for an incoming Gaussian, the effective Green's function for SHG on-axis ($\theta = 0$) is

$$E(x,z) = \frac{\exp\left[-2\frac{x^2}{w_0^2(1+i\xi)} + i\Delta k z\right]}{(1+i\xi)^2}, \tag{4.32}$$

where the parameters are determined in the previous two-photon case. The Green's function is convolved with $M(x, z)$. The absolute value of the result squared gives the intensity of the SHG produced at each point, shown in figure 4.3(c). Notice that SHG is detected from the regions free of any myosin. This is due to the Gouy phase of the laser, where the phase of light switches by π through the focus. Because the neighboring fibers are out of phase by π, the combination with the Gouy phase produces constructive interference when the focus of the laser is between two fibers. A close look at figure 4.3(c) will reveal bright nodes within the SHG stripes, corresponding to the dots in figure 3.14 which appear when imaging through a sagittal plane.

Comparison with the image of $M(x, z)$, in Fig 4.3(a). will show that no SHG originates from from the M-line, the boundary between $M = 1$ and $M = -1$ in our simulation. This is due to the inversion symmetry where the myosin fibers project in opposite directions. This results in the appearance of doublets in the SHG image, two bright points for each sarcomere. When the sarcomere contracts, some authors observe that the doublets are replaced by a single wide bright spot [105, 101]. One explanation is that uneven contractile forces disrupt the boundary at the M-line [100]. Although this explanation may be correct, our simulations show that the doublet disappearance may simply be due to the fibers rotating in and out of plane. Adjusting the laser angle in the simulation by less than 20° causes the doublets to disappear, replicating what appears to be observed in experiments, as in figure 4.4(d). Symmetry at the M-line only exists with respect to the inversion along the axis of the sarcomere. When the laser is perpendicular to the axis of the sarcomere, one observes

the doublets. Once out of alignment, the Gouy phase of the laser causes constructive interference between the myosin on either side M-line, and SHG is observed where none was before.[9] Contraction increases this effect, because sarcomeric volume conservation [93, 96] increases the width of the sarcomere, giving the laser more myosin to interact with, shown in figure 4.4.

The effects demonstrated here arise from the coherence of SHG, demonstrating how the specific spatial arrangement of SHG-active material can enhance or quench the resulting SHG. Because the focusing properties, refractive index, and phase-matching are wavelength dependent, we also anticipate that coherence will produce a spectral signature specific to the underlying crystallinity of the SHG media.

4.4 Wavelength Dependence of SHG

To understand the wavelength dependent SHG spectra measured in Figs. 3.21 and 3.23, we have to account for possible sources of wavelength dependence. As described in section 3.2, the data was corrected to remove instrument-dependent wavelength sensitivities. This leaves phase-matching and the nonlinear susceptibility, $\chi^{(2)}(\omega)$, as sources of dispersion. As with the index of refraction, the nonlinear susceptibility will be far from any resonances. Away from absorption resonance, the wavelength dependent portion of the susceptibility may be expressed in terms of first-order optical

[9] In fact, Plotnikov et al. observe "[When the myofibril contracts,] some changes of SHG intensity were observed at ends of myofibrils that moved out of the plane of section." [101] Thus, it appears it would not be unusual for a dynamic fibril to squirm out of alignment by a few degrees and cause the doublets to disappear.

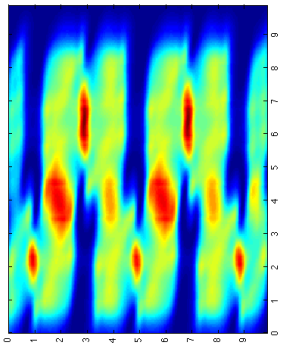

(a) 5 μm sarcomere

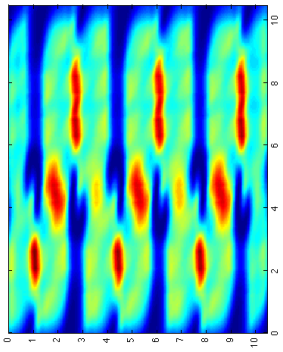

(b) 4 μm sarcomere

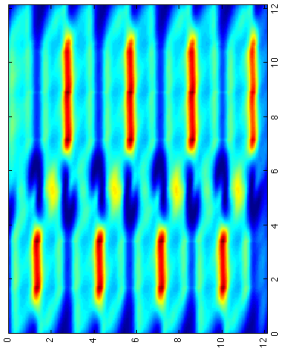

(c) 3 μm sarcomere

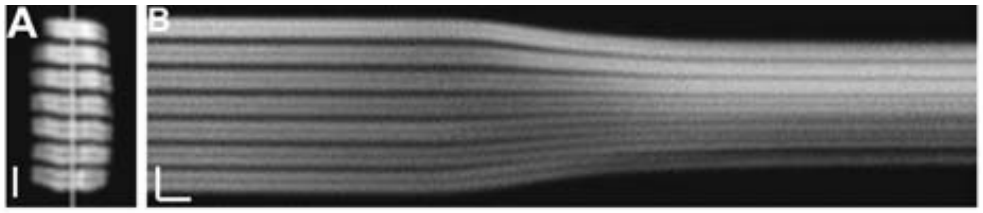

(d) Experiment [101]

Figure 4.4: Using the same schematic as figure 4.3(a), when the laser is tilted by 20°, the doublets disappear. (a)-(c) When accompanied by contracting sarcomeres, the effect is even more pronounced. (d) Compare to the experimentally observed time lapse of a contracting myofibril, adapted from [101]. A snapshot of the myofibril is labeled A (scale bar 2.5 μm, and a space-time diagram of the recorded contraction is labeled B (vertical scale, 2.5 μm; horizontal scale, 0.5 s). Note that the experimental image is in a perpendicular plane to the simulation.

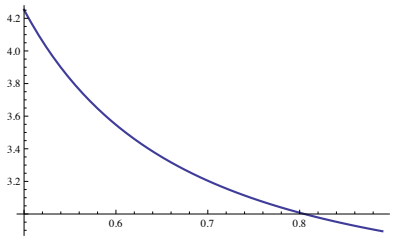

Figure 4.5: The nonlinear susceptibility of muscle, $\chi^{(2)}(\omega)$, based on Miller's rule.

properties using Miller's rule [148, 149, 150]:

$$\begin{aligned}\chi^{(2)}(\omega) &\propto \chi^{(1)}(2\omega)\chi^{(1)}(\omega)^2 \\ &\propto (n_{2\omega}^2 - 1)(n_{\omega}^2 - 1)^2. \end{aligned} \tag{4.33}$$

Because the refractive index decreases monotonically with increasing wavelength, the SHG susceptibility monotonically decreases with wavelength (or increases with frequency) in the wavelength range of concern, as plotted in figure 4.5. It does not contain the steep drop-off observed in the experimental data. This leaves phase-matching as the remaining factor to explain Figs. 3.21 and 3.23.

If we treat the entire muscle as a uniform block of amorphous SHG-active material, we would find the spectrum would vary with depth [151, 67, 141]. Similarly, we would also expect the intensity to vary significantly with depth [71]. Neither is observed.[10] Instead, the spectrum is nearly uniform from edge to edge, as is the intensity, up to the expected effects of field attenuation (see figure 3.8). This implies that the SHG is originating only from the focus. In two-photon fluorescence microscopy, this is an advertised feature, but numerous experiments have demonstrated significant

[10]I'm not saying such a dependence does not exist, just that other SHG efficiency-altering factors prevent observing any systematic variation of this type.

SHG production away from the focus in phase-matched crystals [152, 139]. Although the effective production of SHG would be limited to the focus if the SHG were to produced noncollinearly (i.e.,with some walk-off angle due to birefringence), walk-off angles tend to be very small – only a few degrees [153, 111], which for our optical setup would be of little consequence compared to the size of the focus.[11] Two possible explanations remain: the quasi-crystalline nature of the muscle fibers on either side of the focus can cause the SHG to pick up phase errors, reducing the effective phase-matching [154], making SHG coherent only near the focus. Or, the SHG efficiency is so low that photons are only produced near the focus.

I have taken two approaches to using theory to understand the wavelength dependence. First, to calculate the SHG conversion, we combine quasi-phase-matching with a focused Gaussian beam. This approach requires guessing at the underlying superstructure of the muscle fibers, and it provides us with an insight into hidden correlation length-scales. Second, using the Green's function approach, we calculate the contribution of the wavelength dependence due to changes in collection efficiency.

[11] The effective aperture length for SHG production due to walk-off is $\ell_a = \sqrt{\pi} w_0/\rho$, while the effective length of the focus is $\ell_f = \pi b/2 = \pi k w_0^2/2$ [152]. Thus, walk-off will limit SHG production if $\ell_f/\ell_a = \pi^{3/2} n w_0 \rho/\lambda = \pi^{1/2}\rho/\mathrm{NA} > 1$. NA = 0.8, so walk-off will not be an issue for $\rho \sim 1$ degree (0.02 radians), which is a generous estimate for the spatial walk-off angle for muscle.

4.4.1 Wavelength Dependence Due to Myofibril Packing

Under the paraxial approximation, the SHG conversion due to periodic packing of myofibrils is given by

$$F(\Delta k, z_0, z_f) = \int_{z_0}^{z_f} \sum_{mn} G_{mn} \frac{\exp\left[i(\Delta k z + K_{mn} z)\right]}{1 + i\xi}\, dz, \tag{4.34}$$

where the focus of the laser is at $z = 0$, and z_0 and z_f are the boundaries of the SHG active area. The laser passes through many layers of sarcomeres as it images, and these layers are arranged in a quasi-crystalline manner. The fibers are arranged in a multitude of orientations, states of contraction (sarcomere length), and relative alignment. Thus, the final value results must not be so sensitive to these parameters as to only apply in unrealistically rigid conditions. Because of the drop-off around 850 nm is due to phase-matching, we can interpret the spectra to be reporting some sort of quasi-phase-matching which is only effective up to 850 nm. Thus, we consider the critical lengths created by the phase mismatch, $\ell_c = |\lambda/(2(n_{2\omega} - n_\omega))|$, plotted in figure 4.7. The better the phase-matching, the longer the critical length, but the only truly predictable length scale is the sarcomere length, which is around 2-3 μm. However, the randomness of the orientations mean there will be some effective length that can be used as a fitting parameter.

The structure of muscle was represented using a 1-D function to mimic the density

of sarcomeres,

$$M(z,p) = ((4 - \sin[\pi\frac{z}{2p}]^4 \cos[\pi\frac{z}{p}]4(1 + \cos[2\pi\frac{z}{p}])^2)/2)^4, \tag{4.35}$$

which produces a periodic structure of finite bandwidth, diagrammed in figure 4.6(a). To create a spatial map of the susceptibility, $\chi_M^{(2)}$, $M(x,p)$ is transformed with a square wave with half of the period,

$$\chi_M^{(2)} = M(z,p)Sq(2\frac{x}{p}), \tag{4.36}$$

which is shown in figure 4.6(b). Instead of decomposing $\chi_M^{(2)}$ into its inherent Fourier components, integration was carried out directly. That is,

$$F(\Delta k, z_0, z_f) = \int_{z_0}^{z_f} \chi_M^{(2)}(z,p)\frac{\exp[i\Delta k z]}{1 + i\xi}\, dz. \tag{4.37}$$

To fully account for wavelength dependence, we include the wavelength dependence of the power density (eq. (4.7)) and susceptibility (eq. (4.33)), and fitted p to the representative spectra in figure 3.21(c) and taking $z_0 = -100, z_f = 100$ μm.

The resulting fit is shown in figure 4.8. The fit produced $p = 5$, approximately the same as the alignment of bundles of myofibrils, as seen in figure 3.20. Although 5 μm is a bit too large for ordinary sarcomeric structure, it suggests a stronger inter-myofibril alignment. Further experiments on isolated myofibrils will be essential to separate any further wavelength dependence not due to myofibril alignment. The

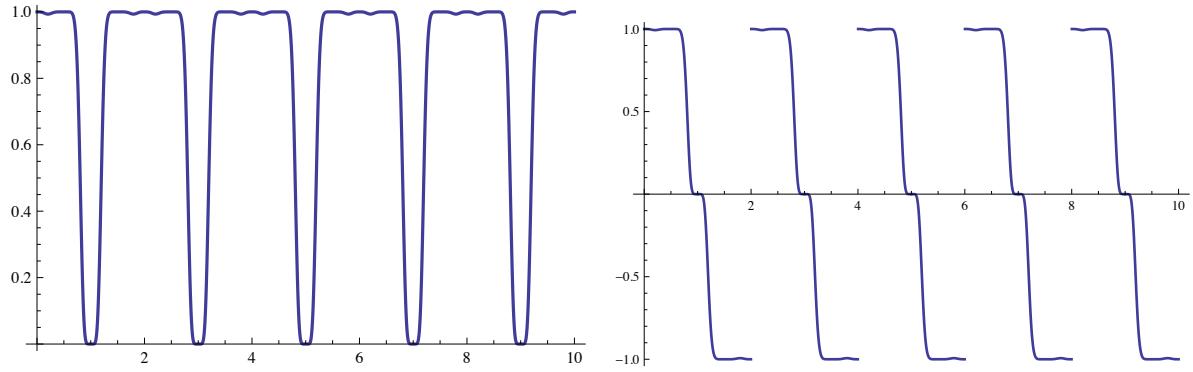

(a) $M(x, p = 1)$ (b) $\chi_M^{(2)}(x, p = 1)$

Figure 4.6: Plot of SHG susceptibility map. Here, $p = 2$.

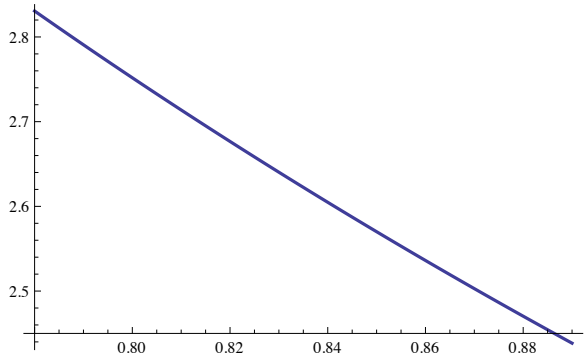

Figure 4.7: ℓ_c as a function of wavelength for the refractive index defined in Eq 3.1. All units are μm.

fit required the use of an experimentally observed refractive index that was larger concave down, instead of more commonly observed concave up shape [79]. Although myofibrils are highly aligned with the immediate neighbors, visual inspection (such as figure 3.17(a)) show there is a scale of structure between a full myocyte and a single myofibril. This work suggests that a length scale of 5 μm appears to be an as yet uncharacterized length-scale of importance within zebrafish muscle.

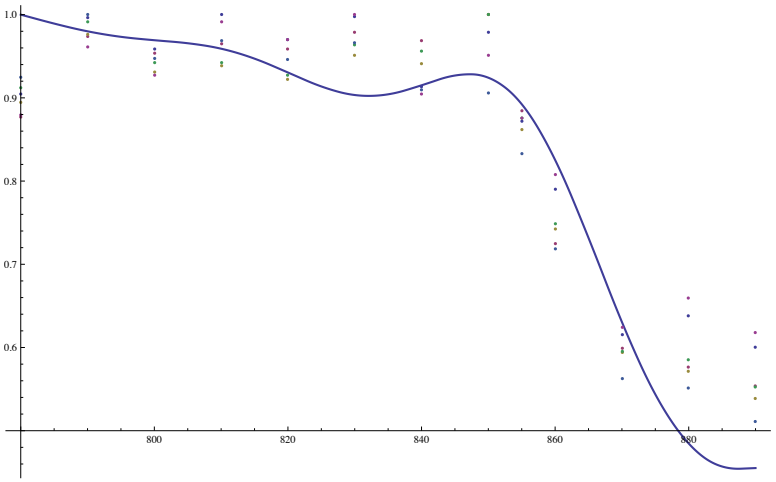

Figure 4.8: Fit of eq. (4.37) using the quasi-phase-matching structure in eq. (4.36), with $p = 5$ μm. The experimental data are from figure 3.21. The x-axis is wavelength in nanometers, and the y-axis normalized intensity.

4.4.2 Wavelength Dependence Due to Collection Efficiency

As stated in section 4.2.2, only SHG emitted with in a limited angular cone will be detected. The cutoff angle is given by $\theta_{\max} = \sin^{-1}(0.55/n_{2\omega})$. Because the cutoff angle varies with wavelength, we expect the collection efficiency to systematically vary. The SHG emission angles also vary with wavelength, as shown in figure 4.9, and this will contribute as well.

The energy detected by the microscope is given by

$$I(\lambda, \mathbf{r}_0) \propto \int_0^{\theta_{\max}(\lambda)} d\theta \int_0^{2\pi} d\phi \mathbf{E}^*_{2\omega}(\Omega, \mathbf{r}_0)\mathbf{E}_{2\omega}(\Omega, \mathbf{r}_0), \tag{4.38}$$

where $\mathbf{E}_{2\omega}(\Omega, \mathbf{r}_0)$ is given by eq. (4.27). Because light is quantized, SHG photons only appear, statistically, from a limited region around the focus. The size of this region depends on the wavelength of light and the intensity of the incoming laser. Using a Green's function approach to calculating the emitted SHG, we find the wavelength

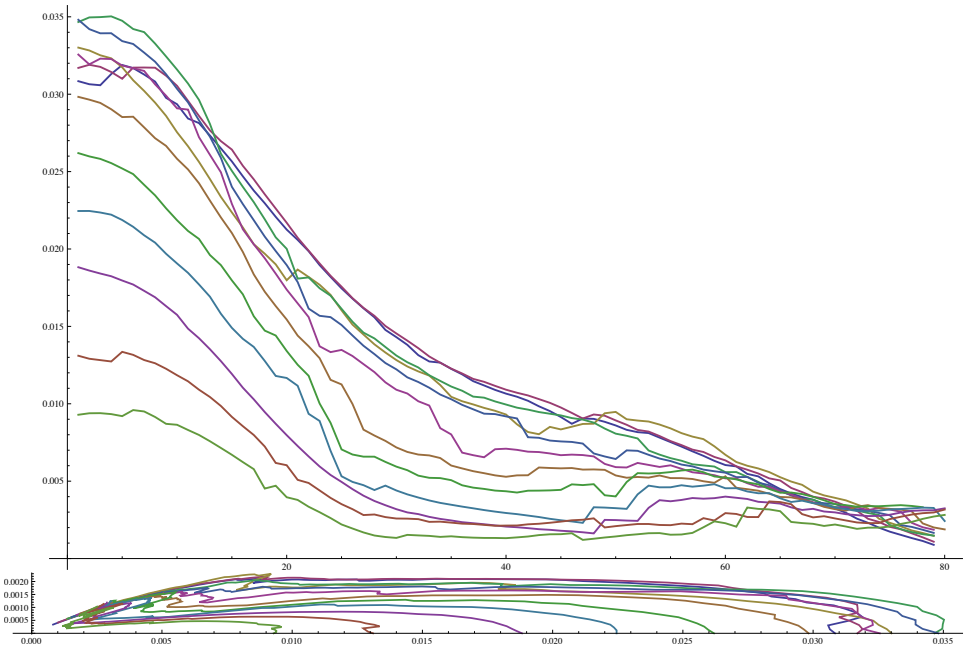

Figure 4.9: SHG emission intensity is angle dependent. (top) SHG intensity as a function of emission angle, the degrees. (bottom) Polar plot of SHG emission. Input wavelength varies from 790 nm to 890 nm, ordered from the bottom up. This plot is not corrected for other wavelength dependent factors. Each curve ends at the maximum angle for collection.

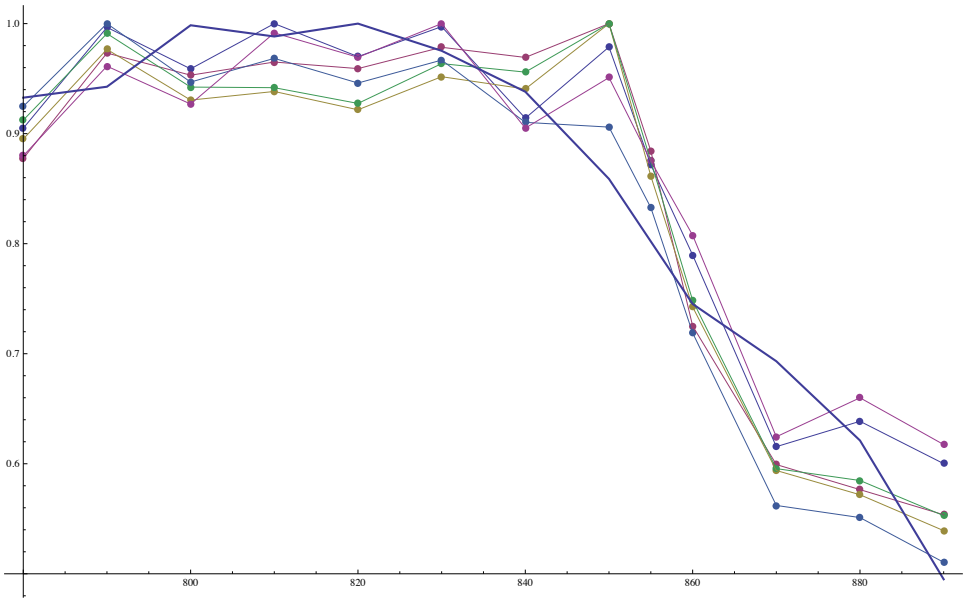

Figure 4.10: The wavelength dependent SHG may also be due to the variation of the size of the laser focus. Here, the SHG active region was constrained to a box extending $5.2b$ along the z-axis and $1.9w_0$ along the x- and y-axis.

dependent intensity aligns well with the data, shown in figure 4.10.

The collection efficiency has a noticeable effect on SHG production from a myocyte. By calculating how collection efficiency and the size of the SHG production volume vary with wavelength, we show the promise of the Green's function approach to capture effects that are beyond the reach of the paraxial approximation. Further work, such as varying the laser intensity to alter the size of the SHG production volume, will allow the Green's function approach to refine our conclusion from the previous section, which were based on the paraxial approximation. Because the kink occurs around 850 nm, we can reasonably hypothesize that part of the effect we see in the wavelength dependence of the SHG from zebrafish myosin is due to wavelength dependent collection efficiency.

4.5 Conclusion

Through the last two chapters, we have experimentally and theoretically analyzed the nonlinear optical properties of zebrafish muscle. Although other works have done an excellent job characterizing the susceptibility of myosin, none has considered the wavelength dependence or closely examined how SHG images differ from fluorescence images. We have determined that the crystalline structure of muscle fibers alters the wavelength dependence away from the inherent susceptibility of an isolated myosin protein. This informs us about the underlying packing of the myocytes. Future experiments which capture not just the intensity of the resulting SHG but also the spatial dependence of the far-field SHG radiation pattern will permit full inversion to find the underlying structural detail. For now, we inferred our results by fitting the data to a hypothetical myocyte.

By calculating the expected patterns produced from the highly structured packing of sarcomeres, we have provided some surprising results, such as explaining the disappearance of the doublets and origin of the herringbone pattern lines as not necessarily being biological in origin, but a fundamental feature of coherent SHG imaging. Because SHG is a coherent process, it produces microscopy images that require closer consideration than fluorescence. With fluorescence, the intensity of a pixel is proportional to the amount of dye in the focal volume, but with SHG, as the present results show, the intensity of a pixel is not a nontrivial correspondence to the microscopic arrangement of SHG susceptible material.

Further work, such as studying a single myofibril, comparing the SHG from dif-

ferent organisms, and repeating a similar analysis on collagen, will help to confirm the predictions made here. Time resolved imaging of muscle development may cast further light onto newly identified organized length scale of 5 μm. More detailed calculation, made without the strong assumptions implicit in the paraxial approximation, will also allow further refinement of our interpretations of the SHG images produced here.

Chapter 5

Microscopic Structure and Dynamics of Air/Water Interface by Computer Simulations and Comparison with Sum-Frequency Generation Experiments

The hydrogen (H) bonded structure of water at the air/water interface [155, 156, 157, 158, 159] is of fundamental interest because it determines the properties of aqueous interfaces and their reactivity. Certain atmospheric reactions [160], such as those involved in ozone depletion, are known to be catalyzed by the ice surface on cloud particles. Study of the air/water interface is also important for understanding more complicated organic/water interfaces [159] that have recently begun to attract interest for its potential for rate acceleration [161] of organic reactions and green chemistry in emulsions. For example, interest in catalytic effects of dangling OHs has also been extended to their role in catalysis of different organic reactions by metal oxides enriched in surface OH groups [162].

The first molecular structure of water at the air/water interface using the surface-

specific vibrational sum-frequency generation (SFG) technique was reported by Du et al. [163] in 1993 [155, 164] In that work, using the titration of dangling OH groups with methanol and hence the complete suppression of the peak of the free OH SFG signal, it was found that about 25% of surface water molecules have one dangling OH bond that is not H-bonded to other water molecules. It is thereby free, and protrudes out of the water phase, confirming earlier predictions from computations [165]. Roughly the same picture of the existence of the free OH bonds at the interface has since been consistently observed in SFG experiments by Richmond [159], Eisenthal [166], Allen [167], and Gan et al. [168], and also in computer simulations [157, 169, 170, 171, 172, 173] The structure of water at the hydrophobic organic/water interfaces was shown to be similar to that at the air/water interface [163, 174, 175]. In the process of understanding the air/water interface, different interpretations were also made in terms of details of the air/water interface using both experiments and computations [155, 176, 177, 178]. Although previous work has made significant progress toward explaining the observed SFG spectra using theory and simulation [159, 159, 179, 180, 181], a complete picture of how rapid motion averages out the SFG has not been presented. In the present chapter, we make a quantitative comparison between multiple experimental observables, going beyond the comparison of ratios. In addition, by utilizing independent experimental results, coupled with molecular dynamics simulation of the air/water interface, the present work has as a goal a better understanding of motional averaging in SFG. This study was prompted by the recent on-water catalysis experiments [161] and our interpretation in terms of

the role of dangling OH groups at the wateroil emulsion interface [182].

The orientation of free OH bonds at the air/water interface has been deduced from several SFG experiments to be nearly perpendicular to the surface plane [163, 168, 183]. An SFG interpretation [183] assumed a step-like distribution for the tilt angles (θ_{OH}) between the free OH bonds and the surface normal, suggesting them to be in the interval $0^\circ \leq \theta_{OH} \leq 51^\circ$, yielding an average tilt angle $\theta_{OH} \approx 35^\circ$. A more recent SFG experiment [168] yielded a similar average tilt angle, $\theta_{OH} \approx 30^\circ$, with a narrow distribution width of $\leq 15^\circ$, assuming a Gaussian distribution model. In contrast to these distributions and average orientations of free OH bonds, however, previous molecular dynamics simulations [157, 169, 159, 171, 172, 184] with various water models consistently predicted widths of the orientational distribution much broader than those assumed in the previous interpretations of SFG experiments [155, 163, 168, 183]. We address this discrepancy by considering the nature of free OH bonds on the surface, and, in a procedure detailed below, selectively removing those that would likely not contribute to the SFG, allowing a direct comparison between our calculations and experimental measurements.

5.1 Methods

The theoretical treatment we use in this chapter to calculate the effective SFG nonlinear susceptibilities originated from the one previously developed in the literature [163, 183] to extract the orientation information of interfacial molecules from SFG experiments. Previous reviews have provided details of the treatment [185, 186].

Here, we summarize the assumptions and key expressions, for completeness, and implement the expressions to obtain the forms that are suitable for numerical calculations of the mode amplitudes by explicit integrals, rather than the more simplified fast and slow approximations [183].

The SFG signal is proportional to the square of the effective nonlinear susceptibility, $\chi^{(2)}_{\text{eff}}(\omega)$, which is a sum of resonant, $\chi^{(2)}_{\text{R,eff}}(\omega)$, and nonresonant, $\chi^{(2)}_{\text{NR,eff}}(\omega)$, contributions [155]:

$$\chi^{(2)}_{\text{eff}}(\omega) = \chi^{(2)}_{NR,eff} + \chi^{(2)}_{R,eff} = \chi^{(2)}_{NR,eff} + \sum_q \frac{A_{q,\text{eff}}}{\omega - \omega_q + i\Gamma_q}, \tag{5.1}$$

where ω is the incident infrared, ω_q is the q^{th} vibrational frequency, $A_{q,\text{eff}}$ is the mode amplitude, and Γ_q is the damping constant for the q^{th} vibrational mode. The sum-frequency spectra are obtained by scanning the IR frequencies that probe the vibrational normal modes, using the IR-visible SFG method. The susceptibility originates at the air/water interface, caused by the symmetry breaking at the boundary. The bulk of the fluid has inversion symmetry and so does not contribute to techniques generating second-order nonlinear polarization.

SFG is approximated to be dipolar in origin, and we neglect any quadrupolar contribution that could emanate from the bulk [163]. In this paper we focus on the free OH stretching mode of water molecules at the air/water interface, $\omega_q = 3698$ cm^{-1}. This stretching frequency corresponds to the water configuration where one OH bond is free while the other OH bond of the same parent water molecule is still H-bonded to neighboring water molecules (so-called "single-donor" configuration). The spectra

for the *ssp*, *ppp*, and *sps* combinations of polarization, labeled in the order of the sum frequency output, visible input, and infrared input fields, are obtained in SFG experiments.

The A_{eff}'s in eq. (5.1) can be related to the intrinsic tensor components via the Fresnel factors, i.e., via the macroscopic local field corrections, L_{ii} [185],

$$A_{\text{eff}}(ssp) = L_{yy}(\omega_s)L_{yy}(\omega_1)L_{zz}(\omega_2)\sin\beta_2 A_{yyz} \tag{5.2a}$$

$$\begin{aligned} A_{\text{eff}}(ppp) = &- L_{xx}(\omega_s)L_{xx}(\omega_1)L_{zz}(\omega_2)\cos\beta_s\cos\beta_1\sin\beta_2\, A_{yyz} \\ &- L_{xx}(\omega_s)L_{zz}(\omega_1)L_{xx}(\omega_2)\cos\beta_s\sin\beta_1\cos\beta_2\, A_{yzy} \\ &+ L_{zz}(\omega_s)L_{xx}(\omega_1)L_{xx}(\omega_2)\sin\beta_s\cos\beta_1\cos\beta_2\, A_{zyy} \\ &+ L_{zz}(\omega_s)L_{zz}(\omega_1)L_{zz}(\omega_2)\sin\beta_s\sin\beta_1\sin\beta_2\, A_{zzz} \end{aligned} \tag{5.2b}$$

$$A_{\text{eff}}(sps) = L_{yy}(\omega_s)L_{zz}(\omega_1)L_{yy}(\omega_2)\sin\beta_1\, A_{yzy}, \tag{5.2c}$$

where β_s, β_1, and β_2 are the reflected or incident angles of sum frequency output, visible input, and infrared input, respectively. For an azimuthally isotropic air/water interface and assuming the visible frequency (ω_1) and the sum frequency (ω_s) are far removed from electronic resonances, there are only three independent nonvanishing components, $A_{xxz} = A_{yyz}$, $A_{xzx} = A_{yzy} = A_{zxx} = A_{zyy}$, and A_{zzz} [185]. The ω_2 is the infrared input light source, and he L_{ii}'s are defined in terms of the frequency-dependent effective dielectric constant of the interfacial layer, $\epsilon(\omega)$, an air/water interface in our case. For the air/water interface, $\epsilon(\omega_s) = \epsilon(\omega_1) = 1.31$ and $\epsilon(\omega_2) = 1.2$ were estimated [183] from a three-layer model. The numerical values of all these

variables can be found in Table 1 of ref. [183]. The A_{ijk}'s are intrinsic (macroscopic) properties of the interface, whereas the experimental observables, A_{eff}'s, are affected by the frequency-dependent dielectric response of the interface medium as described above and by the experimental conditions. Therefore, using Eq 5.2 we obtain A_{eff}'s from the calculated A_{ijk}'s.

The A_{ijk}'s in eq. (5.2) are the resonant components of macroscopic susceptibility tensor, and can be represented at a molecular level as an ensemble average of the molecular hyperpolarizability in the body fixed frame, $\beta_{q,\lambda\mu\nu}$ (corresponding to the hyperpolarizabililty A_q of Du et al. [163]), of the interfacial water molecules in the lab frame (denoted by *ijk*), where q corresponds to the IR resonant mode of the free OH bond. The derivation begins with the Fourier-Laplace transform of the classical SFG response function: related references are [180, 183, 187, 188, 189, 190].

$$\begin{aligned} A_{q,ijk} &\equiv (\omega_2 - \omega_q + i\Gamma_q)\chi^{(2)}_{ijk} \\ &= -(\omega_2 - \omega_q + i\Gamma_q)\frac{i\omega_2}{k_b T}\int_0^\infty e^{i\omega_2 t}\langle \alpha_{ij}(0)\mu_k(t)\rangle \, dt, \end{aligned} \tag{5.3}$$

where α_{ij} is the quantum mechanical instantaneous polarizability tensor of the entire surface, and μ_k is the in instantaneous dipole moment vector of the surface. eq. (5.3) must be converted to be applicable to classical MD simulations. Because we are considering a mode directly on resonance, we introduce the two resonant states of the full basis set, $|0\rangle$ and $|1\rangle$, where, $|1\rangle$ represents the first excited vibrational mode of the free OH-bond at 3700 cm^{-1}. This contributes a factor $\langle 0|\mu(t)\rangle|1\rangle \propto \exp(-i\omega_q t)$. Because the integral in eq. (5.3) will be dominated by the resonance term, we replace

ω_2 with ω_q, the value at the peak. We take the remaining QM expressions to their classical limit [191]. In particular, the orientations of the surface bonds will be given by their classical values, so we may expand eq. (5.3) as

$$A_{q,ijk} = -(\omega_2 - \omega_q + i\Gamma_q)\frac{i\omega_q}{k_b T}\sum_{\lambda\mu\nu}\alpha_{\lambda\mu}\mu_\nu \times \int_0^\infty e^{i(\omega_2-\omega_q)}\left\langle \sum_n^{N_{OH}(t)}\sum_m^{N_{OH}(t)} D^n_{i\lambda}(0)D^n_{j\mu}(0)D^m_{k\nu}(t)\right\rangle, \tag{5.4}$$

where the sum of λ, μ, or ν is over $\hat{u}$, $\hat{v}$, or $\hat{w}$, the basis of the body-fixed molecular reference frame. Similarly, $i = \hat{x}, \hat{y}, \hat{z}$, the laboratory frame basis, and the same holds for the j and k. The double sum in eq. (5.4) includes the n^{th} and m^{th} free surface OH bonds at times 0 and t, respectively. At time t there are $N_{OH}(t)$ free OH bonds. $D^n_{i\lambda}$, $D^n_{j\mu}$ and $D^m_{k\nu}$ are the time-dependent direction cosine matrix elements of the n^{th} and m^{th} free surface OH bonds, defined as $D_{xu} = \hat{x}\cdot\hat{u}$. Thus, $\alpha_{\lambda\mu}$ and μ_ν are the mean per-bond body-centered reference frame polarizability and dipole, respectively. eq. (5.4) is a generalization of equations in Wei and Shen [183], and it can be shown to reduce to corresponding approximations of slow and fast orientational dynamics. However, eq. (5.4) also explicity incorporates spatial correlations between water molecules, unlike those in Wei and Shen, who employed a mean-field approximation,[1].

Inspection of eq. (5.3) shows that we may substitute in the bond hyperpolariz-

[1]The mean-field approximation is very common in SFG analysis. Most texts, such as Shen's [190] state that the total susceptibility is N times the susceptibility of a single molecule. Although it may make sense to construct an average susceptibility per molecule, it does not necessarily follow that the average susceptibility is the same as the susceptibility of a single, isolated molecule

ability, $\beta_{q,\lambda\mu\nu}$, giving

$$A_{q,ijk} = -(\omega_2 - \omega_q + i\Gamma_q) \sum_{\lambda\mu\nu} i\beta_{q,\lambda\mu\nu} \times \int_0^\infty e^{i(\omega_2-\omega_q)} \left\langle \sum_n^{N_{OH}(t)} \sum_m^{N_{OH}(t)} D^n_{i\lambda}(0) D^n_{j\mu}(0) D^m_{k\nu}(t) \right\rangle . \tag{5.5}$$

We approximate the hyperpolarizability of H_2O at $\omega_2 = \omega_1 = 3698\ \mathrm{cm}^{-1}$ by the "bond hyperpolizability" of the free OH bond with cylindrical symmetry. This assumption accomplishes two things. First, this simplifies eq. (5.5) by converting it to a form that can be evaluated using the experimentally observed bond hyperpolarizability. Second, it allows us to exclusively account for the orientation of the free OH bounds, the quantities that are produced by the simulation. Under this assumption, $\beta_{q,\lambda\mu\nu}$ has only two unique nonvanishing values, $\beta_{\perp,\perp,\parallel}$ and $\beta_{\parallel,\parallel,\parallel}$, where $\perp$ and $\parallel$ denote the body-fixed axes along and perpendicular to the free OH bond direction. To explain this restriction, we consider how the incoming lasers interact with the underlying symmetry of the cylindrical bond. The bond has broken symmetry along its axis, from the O to the H, but it is symmetric under rotation around the OH axis. When the third component of the hyperpolarizability tensor, which represents the IR beam, is perpendicular to the axis, $\perp$, the IR laser interacts with the part of the bond that is symmetric under rotation and centrosymmetric, so the intrinsic susceptibility from the IR is 0. When the IR beam is parallel, $\parallel$, it is interacting with the noncentrosymmetric part of the cylindrical bond, so it has nonzero value. The visible beam is far off resonance, so the bond has nearly zero coupling, hence the bond looks symmetric

from all directions. This means the visible laser cannot drive the SFG on its own, so the IR beam must be $\|$, giving $\beta_{,,\perp} = 0$. Because the frequency of the visible laser is chosen to be far from any electronic resonances, the susceptibility at ω_1, the incoming visible laser frequency, and $\omega_s = \omega_1 + \omega_q$, the outgoing SFG frequency, are nearly identical, because the susceptibility has small variance far away from resonance. Hence, we have $\chi_{ijk}(\omega_s, \omega_1, \omega_w) = \chi_{jik}(\omega_1, \omega_s, \omega_2) \approx \chi_{jik}(\omega_s, \omega_1, \omega_2)$. This is called Kleinman's symmetry [113], and it means that first and second components of the hyperpolizability must be identical. Thus, the only nonzero components correspond to $\beta_{\perp,\perp,\|}$ and $\beta_{\|,\|,\|}$. Using Raman and IR measurements, these values have been measured [163, 183]:

$$\beta_\| \equiv \beta_{\|,\|,\|} = \beta_{www} = 2.88 \times 10^{-27} \ \frac{\mathrm{m}^5}{\mathrm{Vs}}, \text{ and}$$
$$\beta_\perp \equiv \beta_{\perp,\perp,\|} = \beta_{uuw} = \beta_{vvw} = 0.32\beta_\|.$$

Therefore, the sum over (λ, μ, ν) only has three nonvanishing combinations: $(\hat{u}, \hat{u}, \hat{w})$, $(\hat{v}, \hat{v}, \hat{w})$, and $(\hat{w}, \hat{w}, \hat{w})$.

The time-dependent direction cosine matrix is $D_{\ell\zeta} = \hat{\ell} \cdot \hat{\zeta}$, with $\hat{\ell} = (\hat{x}, \hat{y}, \hat{z})$ the fixed lab coordinates and $\hat{\zeta}(t) = (\hat{u}, \hat{v}.\hat{w})$ are the time-dependent molecular coordinates of the free OH bond. The water surface normal is along the z-axis of the laboratory coordinates, and a free OH bond forms an angle $\theta(t)$ with the surface normal at time t. The angle $\theta(t)$ lies in the interval $[0, \pi]$, and the angle with respect to $\hat{x}$ in the $\hat{x}.\hat{y}$ plane, $\phi(t)$ is in the interval $[0, 2\pi]$. The the full expression of the

molecular coordinates in terms of laboratory coordinates is

$$\hat{u} = \cos\phi\cos\theta\,\hat{x} + \sin\phi\cos\theta\,\hat{y} - \sin\theta\,\hat{z} \tag{5.6a}$$

$$\hat{v} = -\sin\phi\cos\theta\,\hat{x} + \cos\phi\cos\theta\,\hat{y} - \sin\theta\,\hat{z} \tag{5.6b}$$

$$\hat{w} = \cos\phi\sin\theta\,\hat{x} + \cos\phi\cos\theta\,\hat{y} + \cos\theta\,\hat{z}. \tag{5.6c}$$

$$\tag{5.6d}$$

To evaluate the error introduced by finite simulation snapshot time interval, three MD simulations with different snapshot time intervals were used for the calculations, as described below.

In the MD simulations, 1264 water molecules were placed in a rectangular box of dimension $30\times30\times70$ Å^3 where the water section is sandwiched between two sections of vapor along the z-axis. Periodic boundary conditions were used in all directions, but, along the z-axis, we sandwiched the water slab with two slabs of vacuum. Water molecules were modeled by the DL_POLY 2 program [192] as rigid and nonpolarizable, using the TIP3P potential commonly used for molecular mechanics [193]. The Nosé-Hoover thermostat [194, 195] was used to perform the constant NVT MD simulations at T = 298 K, and the SHAKE algorithm [196] was used to constrain the degrees of freedom of rigid water molecules. The time step for integrating Newtons equations is always 1 fs, but it is unnecessary to record the results of each step. Instead, we recorded the instantaneous orientation of all free OH bonds in discrete snapshots, evolving the simulation between snapshots without recording the individual steps. In

this work, we saved all of the configurations for the snapshot time interval of 1 fs, and every 10 configurations for a time interval of 10 fs, and every 100 configurations for 100 fs. After adequate equilibration of a random initial configuration, simulated with a time step of 1 fs, three individual simulations each with a different snapshot time interval of either 1 fs, 10 fs, or 100 fs were performed. In the three cases, to generate a total of 40,000 configurations, the total simulation time was 40 ps, 400 ps, and 4 ns, respectively. The correlation functions were calculated using a time average,

$$C(t) = \langle \alpha(0)\mu(t) \rangle = \frac{1}{N+1} \sum_{n=0}^{N} \alpha(n\delta t)\mu(t + n\delta t),$$

where $N = (T - t)/\delta t$. T is the total length of the simulation, and δt is the time step of the simulation results.[2] The results are shown in figure 5.3.

For sampled configurations of the water/vacuum interface, it is essential to select only the free OH bonds on the water surface that respond to the laser beams in real SFG experiments. Only the free OH bonds at the surface will break the inversion symmetry necessary for an SFG signal. Previous simulation studies [157, 169, 159, 171, 172] identified surface free OH bonds as those positioned above a certain cutoff in the z-direction. However, as can be seen in figure 1, the water surface in the model fluctuates appreciably, and an arbitrary cutoff unavoidably includes the OH bonds in the bulk. Although isotropy due to random orientation of the free OH bond in the bulk will provide a natural surface selection effect, the local field corrections relevant

[2]This time average is equivalent to the ensemble average on the limit $T \to \infty$. If the simulation were to not fully explore the phase space, the correlation function can develop artifacts due to over representation of some simulation behavior. If an ensemble average is used, the solution is to add more simulations.

to calculating A_{eff}'s only apply to the free OH bonds directly on the surface [197]. The correct selection procedure would be to select only those free OH bonds that are both on the surface and those that do not contribute to bulk inversion symmetry. This aspect led us to exclude surface free OH bonds oriented toward the bulk and keep those oriented toward the vapor. Two experimental quantities, the surface density of free OH bonds [198], $N_s = 2.8 \times 10^{18}$ m^2, and their average tilt angle [163, 168, 183] of about 35°, guided us in determining free surface OH bonds that affect the SFG results. In this study, the following three criteria were combined to select the free surface OH bonds which lead to agreement with the above two experimental quantities. First, an OH bond is considered on the surface if no oxygen atoms are inside the open cylindrical space above the hydrogen atom with a radius of 1.5 Å(roughly the length of an OH bond). Second, the OH bond is not H-bonded with any oxygen atoms. An OH bond is considered H-bonded with another oxygen atom if the interoxygen distance is less than 3.5 Å(first coordination shell) and simultaneously the $\text{O} - \text{H} \cdots \text{O}$ angle is less than 30° (approximate librational wagging amplitude of the H-bonds) [199]. Because of approximations in the dielectric model, some free OH bonds may be inappropriately included. If the bond is oriented with a large angle to the surface normal, in reality it would have a high probability to be effectively canceled out by another OH bond pointing in the opposite direction. Our selection method must produce an orientation ensemble that reflects this potential inversion symmetry. To address this feature, we used a single free parameter in the calculations, a free OH cutoff angle. Bonds with θ_{OH} greater than the cutoff angle were not included in the calculations.

A snapshot of the free surface OH bonds is shown in figure 5.1(b). Clearly, the free surface OH bonds in the model are sparse and their oxygen atoms do not form a uniform monolayer. The distribution of the cosine function of the tilt angle θ with respect to the surface normal is plotted in figure 5.2. As expected, the three snapshot intervals do not yield a large difference in the cosine distribution, because of the equilibrating prior to the simulation. Because a cutoff of 60° was applied to the tilt angle, $\cos\theta_{OH}$ cannot be smaller than 0.5, as observed in figure 5.2. The plurality of free OH bonds is oriented along the surface normal.

With the surface free OH bonds determined, the A_{eff}'s were calculated using Eqs. (5.3) – (5.4). Because the experimentally determined values of the A_{eff}'s were determined by fitting the observed spectra to Lorentzians [183], the spectra calculated with the simulation results were also fit to Lorentzians. That is, after calculating the correlation functions, by using eq. (5.4), we calculate the Fourier-Laplace transforms at all ω_2 to obtain a spectral response. These Fourier-Laplace transforms are then corrected to account for local field corrections, as in eq. (5.2), leading to the frequency-dependent susceptibilities $\chi_{ssp}(\omega)$, $\chi_{ppp}(\omega)$, and $\chi_{sps}(\omega)$. To arrive at the A_{eff}'s, we take the absolute value of the susceptibilities, as these are the quantities measured in the experiments. The spectra are fit to Lorentzians, $a^2/((\omega-\omega_q)^2+\gamma^2)$, thereby extracted a and γ. The constant a is the correlation function $\langle\alpha(0)\mu(t)\rangle - \langle\alpha\mu\rangle_{\text{final}}$ evaluated at $t=0$, where $\langle\alpha\mu\rangle_{\text{final}}$ is the baseline of the plot. The value of a is determined only by the equilibrium properties and is insensitive to the detailed dynamics, while the dynamics lie in Γ_q (and γ).

The γ which is extracted from our simulation cannot be the same as Γ_q. First, a brief consideration of the correlation functions in figure 5.3 shows the decay times are on order 0.1 picoseconds, while experimentally observed decay times are closer to 1 picosecond, differing by two orders of magnitude. This discrepancy is due to the binary classification of free surface OH bonds. Bonds may appear and disappear extremely rapidly. In reality, the bond's ω_q would drift in concert with its exposure, equaling 3698 cm^{-1} when free and moving smoothly and continuously to other frequencies as it form bonds with its neighbors. Thus, the experimentally observed bonds will have a much longer correlation time. Even so, we expect the amplitude, a, to be unaffected by the this binary selection procedure, as we successful capture the equilibrium properties. Hence, as expected, a correlation time that is too small corresponds to a spectral width that is far too wide.

Therefore, what we are calculating is not A_{ijk} but a quantity better labeled as A_{MD}, originating from $\chi^{(2)}_{MD}$. We define $\alpha = A_{ijk}/A_{MD}$. Because we have defined the spectrum of $\chi^{(2)}_{MD}$ to have a peak at ω_q, and because we observe it to be largely Lorentzian in nature, we know

$$\begin{aligned} \alpha^2 &= \frac{A^2_{ijk}}{A^2_{MD}} \\ &= \frac{\Gamma_q \int |\chi^{(2)}_{ijk}(\omega)|^2}{\gamma \int |\chi^{(2)}_{MD}(\omega)|^2}. \end{aligned} \tag{5.7}$$

We can see in eq. (5.7) that the relative areas under the curve in the spectra determine the final value of α. By Parseval's Theorem, $\int_{-\infty}^{\infty} |\chi^{(2)}_{ijk}(\omega)|^2 d\omega = \int_{-\infty}^{\infty} \delta C^2_{ijk}(t) dt$, where

$\delta C(t)$ is the mean-subtracted correlation function. Because the mean-subtracted correlation function is also the impulse response function, the integrals are the total power produced following a delta-function input pulse. We assume that the two powers produced are identical.[3] Therefore, $\alpha = \sqrt{\Gamma_q/\gamma}$, which we will use as a correction factor. We then have

$$A_{\text{eff}} = \sqrt{\frac{a}{\Gamma_q \gamma}}.$$

We divided by Γ_q to account for the fact that its built into the β_{ijk}, which comes from an experimental measurement. The resulting corrected amplitudes are shown in Table 5.2. All ratios of the calculated mode amplitudes are nearly within the measured error of the experimental ratios $A_{\text{eff}}(ssp)\colon A_{\text{eff}}(ppp)\colon A_{\text{eff}}(sps) = 1\colon 0.28 \pm 0.04\colon 0.05 \pm 0.02$.

The largest amplitudes in Table 5.2, the $A_{\text{eff}}(ssp)$ and $A_{\text{eff}}(ppp)$, correspond to the incident IR laser being p-polarized. In p-polarization, the electric field vector is parallel to the plane of incidence and therefore probes free OHs that are nearer to the surface normal, and these free OHs are those with the most orientational anisotropy. The $A_{\text{eff}}(ssp)$ is about three times larger than the $A_{\text{eff}}(ppp)$, perhaps reflecting the factor of three difference between $\beta_\perp$ and $\beta_\parallel$. The $A_{\text{eff}}(sps)$ is smaller than the other two, presumably because with the incident s-polarization, the IR tends to probe free OHs that are closer to being flat on the surface.

[3]This is a major assumption. One way to justify it may be as follows: Let's assume the simulation fully captures the rotational dynamics and the symmetry breaking at the surface. Because this is the symmetry breaking responsible for the SFG, we can assume it to be independent of the other modes we have neglected. Effects such as motional narrowing, which may be particularly strong at the surface due to rapid change in electric field, may have the effect of slowing down surface dynamics without altering the total time-averaged asymmetry.

5.2 Results and Discussion

The detailed information of the microscopic structure and dynamics of water/vacuum interface provided by the computer simulations provide some insight into the physical meaning of the three experimental observable mode amplitudes, the average orientation, and free OH bond surface density. Our results, shown in Table 5.2 achieve good agreement with observed ratios, and they are also within an order of magnitude of experimentally measured results. Because the 1 fs snapshot interval led to a total integration time of 40 ps, which may be too short to adequately generate statistics (others have used multiple nanoseconds [187]), those results would expectedly differ from the longer simulation times. Although Wei and Shen obtained agreement in the calculated ratios of $A_{\text{eff}}(ssp) : A_{\text{eff}}(ppp)$ by assuming the rotational dynamics of θ_{OH} are very fast compared to the vibrational lifetime, they arrived at precisely $A_{\text{eff}}(sps) = 0$ [183]. Our calculations produce a small but nonzero $A_{\text{eff}}(sps)$, which we plan to investigate more fully comparing the slow approximation limit of the present equations. We will determine this further in future calculations. Although Gan et al. [168] suggest the free OH bonds rarely orient perpendicularly to the surface, their results assumed the distribution of angles to be Gaussian, with a width of about 15 degrees, instead of using a distribution similar to the one calculated in figure 5.2. By calculating the distribution of the bonds and employing a cutoff, we obtain good agreement in the ratio of effective susceptibilities. We also show that not all free OH bonds are necessarily SFG active, and this may be a source of discrepancy between theoretical measurements of bond orientations and the narrower results from exper-

iments [168]. As expected, $A_{\text{eff}}(ssp)$ is the largest component because it represents the IR laser coupling directly to the component of the free OH bond oriented perpendicularly to the surface, the orientation with the largest anisotropy. Future work will reveal more information when we extend the overall results and compare them with the slow and fast approximations of the present equations. Based on the present MD simulations of the air/water interface with the TIP3P empirical water model, the amplitudes and their ratios of the effective nonlinear susceptibilities (A_{eff}s) were calculated for different polarization combinations and compared with sum-frequency generation (SFG) experiments. Free surface OH bonds are selected as the OH bonds (1) which are not hydrogen-bonded to other oxygen atoms; (2) whose title angles with respect to the surface normal are smaller than 60°; and (3) no oxygen atoms are above the hydrogen atom. With this definition of free surface OH bonds, the calculated average surface density and average tilt angle closely match the experimental values. The calculated absolute values of the experimental observable mode amplitudes differ, while the ratios are relatively similar. The water model presented here was utilized to capture the dynamic orientational distribution of surface free OH bonds. Although the present water model, TIP3P, may be satisfactory for predicting dangling surface OH bonds, there are indications from unpublished work that it predicts too many dangling OHs in bulk water, compared with experiments for nonbonded OH bonds. Measurements of nonbonded OHs in bulk water have been reported by Eaves et al. [200]. For studies of bulk reaction dynamics, an alternative to the TIP3P model should be explored. We are investigating how the SPC/E model [201], which has

been used for bulk water structure, will alter the calculated susceptibilities. Due to the SPC/E model being better at predicting bulk water properties, we expect the enhanced correlation to bring the susceptibilities even closer to experimental results. We have not considered the effects of capillary fluctuations on the calculated effective susceptibilities, and this will be investigated in a future publication on SFG. In addition, future simulations calculating ensemble averages of correlation functions, instead of effective time averages, may reduce artifacts leading to variations in the calculated susceptibilities between snapshot lengths. This simulation study adds to the theoretical insight into the microscopic structure of the vacuum/water interface, and the present results provide useful information in supporting the recent theory of on-water heterogeneous catalysis [182].

5.3 Conclusion

In summary, we have formulated the SFG equations in a form where molecular dynamics (MD) calculated quantities can be directly compared with hyperpolarizability (polarizability-dipole) coefficients, A_{eff}, extracted from the experimental data for different types of polarization combinations of the infrared, visible, and reflected light. Preliminary MD results were obtained and the extracted information compared with the experimental data, both in the comparison of ratios of A_{eff}s and also for comparison with their absolute values. The SFG results were interpreted in terms of physical concepts, for use in exploring other issues and with additional water models. Data from independent sources, infrared and Raman experiments, has been used, in

Table 5.1: Average number of free surface OH bonds, $\langle N_{OH} \rangle$, and average orientation angle, $\langle \theta_{OH} \rangle$, of free surface OH bonds calculated from three MD simulations with different snapshot time intervals

Snapshot interval	$\langle N_{OH} \rangle$	$\langle \theta_{OH} \rangle$
1 fs	26	38°
10 fs	26	38°
100 fs	26	38°

conjunction with SFG theory, to calculate the SFG susceptibility coefficients. In this way, the overall SFG problem was divided into two parts, rather than calculating *ab initio* the quantum mechanical values of the dipole moment and polarizability derivative. They, in practice, can be computed separately or, as above, evaluated from independent experimental data.

Table 5.2: Results of fitting the calculated spectrum to a Lorentzian and correcting for experimental width.

Mode Amplitudes (10^{-9} m^2 V^{-1}s^{-1})	1 fs	10 fs	100 fs	Experiment
$A_{\text{eff}}(ssp)$	3.19	1.23	2.95	1.7
$A_{\text{eff}}(ppp)$	0.96	0.38	0.9	0.48
$A_{\text{eff}}(sps)$	0.05	0.02	0.026	0.09
$ssp : ppp : sps$	1:0.30:0.02	1:0.31:0.02	1:0.30:0.01	1:0.28±0.04:0.05±0.02

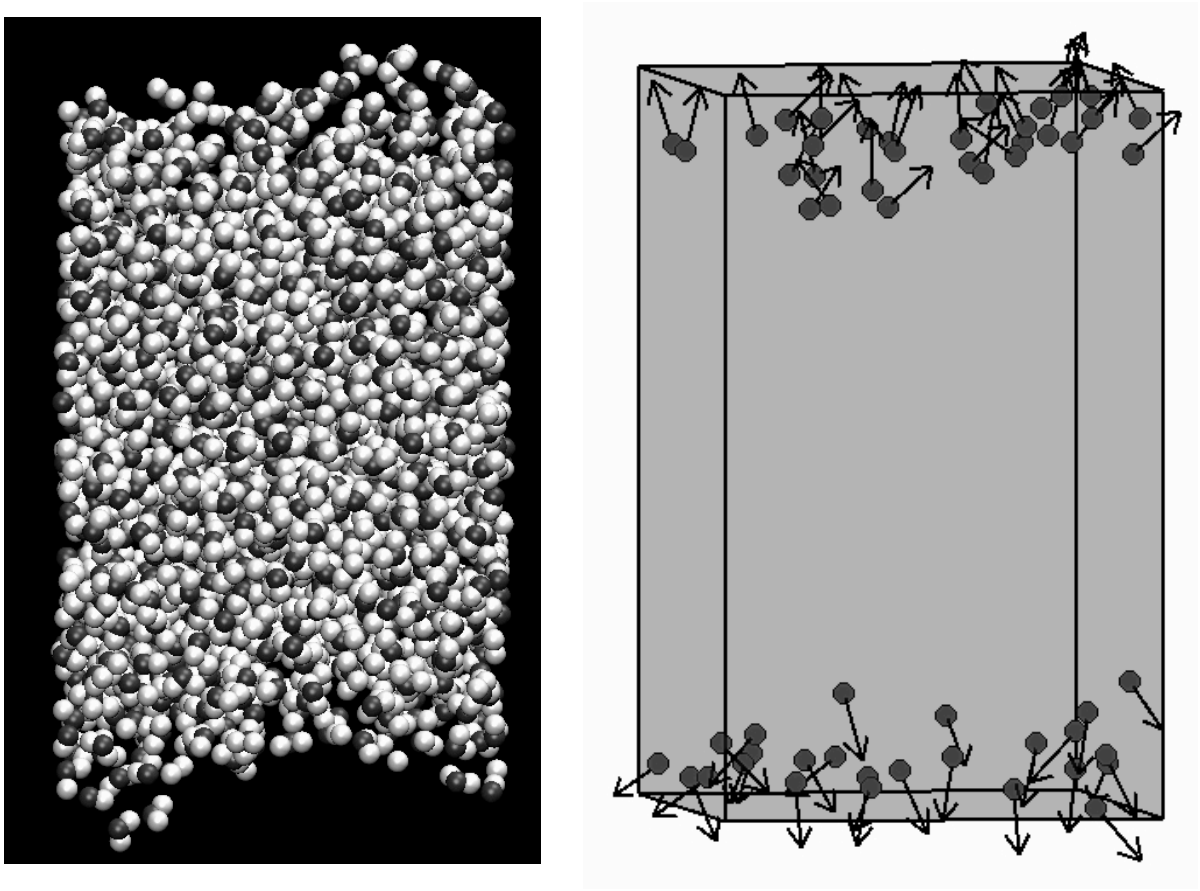

(a) (b)

Figure 5.1: (a) Snapshot of the simulated water/vacuum interfaces. Black spheres represent oxygen atoms, and white ones represent hydrogen atoms. (b) Snapshot of the chosen free surface OH bonds. Black spheres represent oxygen atoms and the vectors point from oxygen atoms to the bound hydrogen atoms. The vectors are elongated for clearer illustration.

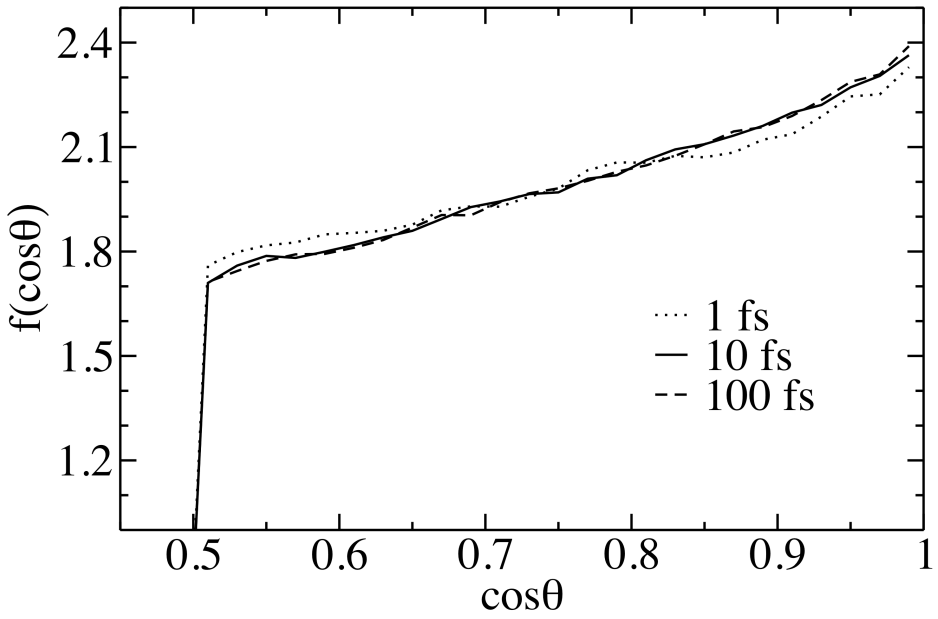

Figure 5.2: Probability density of the cosine of the tilt angle with respect to the surface normal, using a cutoff angle of 60°. The three MD simulations with different snapshot intervals of 1, 10, and 100 fs, respectively, result in very similar cosine angle distributions.

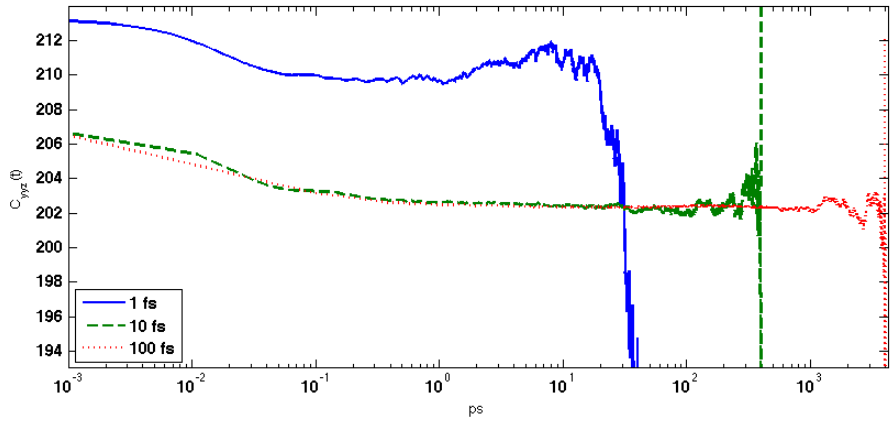

(a) $C_{yyz}(t)$

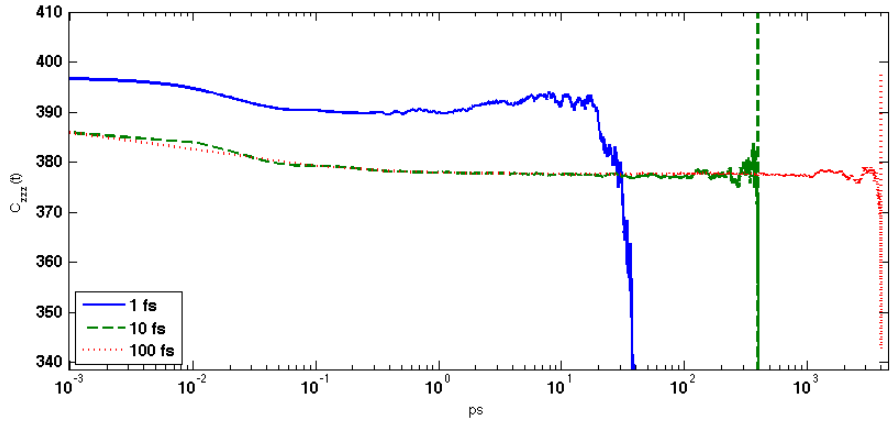

(b) $C_{zzz}(t)$

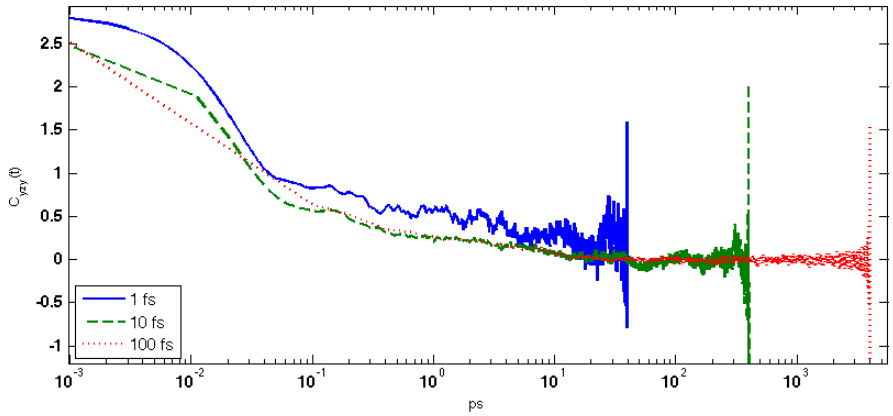

(c) $C_{yzy}(t)$

Figure 5.3: Correlation functions of free OH bonds produced by simulation, using three different snapshot times, 1 , 10 , and 100 fs. Note the semi-log x-axis, which is in picoseconds.

Bibliography

[1] Y. Wang, N. O. Hodas, Y. Jung, and R. A. Marcus, "Microscopic structure and dynamics of air/water interface by computer simulations—comparison with sum-frequency generation experiments," *Phys. Chem. Chem. Phys.*, vol. 13, no. 12, p. 5388, 2011.

[2] T. M. Squires and S. R. Quake, "Microfluidics: Fluid physics at the nanoliter scale," *Rev Mod Phys*, vol. 77, pp. 977–1026, 2005.

[3] W. Coffey, Y. Kalmykov, and J. Waldron, *The Langevin equation: with applications to stochastic problems in physics, chemistry, and electrical engineering.* 2004.

[4] E. R. Kay, D. A. Leigh, and F. Zerbetto, "Synthetic molecular motors and mechanical machines," *Angew Chem Int Edit*, vol. 46, no. 1-2, pp. 72–191, 2007.

[5] R. Field and F. Schneider, "Oscillating Chemical-Reactions and Nonlinear Dynamics," *J Chem Educ*, vol. 66, no. 3, pp. 195–204, 1989.

[6] P. Y. Placais, M. Balland, T. Guerin, J. F. Joanny, and P. Martin, "Spontaneous Oscillations of a Minimal Actomyosin System under Elastic Loading," *Phys Rev Lett*, vol. 103, no. 15, p. 158102, 2009.

[7] Y. Gao, W. Yang, R. Marcus, and M. Karplus, "A model for the cooperative free energy transduction and kinetics of ATP hydrolysis by F-1-ATPase," *P Natl Acad Sci Usa*, vol. 100, no. 20, pp. 11339–11344, 2003.

[8] D. Helbing and S. Lämmer, "Network-induced oscillatory behavior in material flow networks and irregular business cycles," *Phys Rev E*, vol. 70, p. 6, nov 2004.

[9] S. Green, J. Bath, and A. Turberfield, "Coordinated Chemomechanical Cycles: A Mechanism for Autonomous Molecular Motion," *Phys Rev Lett*, vol. 101, p. 238101, dec 2008.

[10] K. Svoboda, P. P. Mitra, and S. M. Block, "Fluctuation analysis of motor protein movement and single enzyme kinetics," *P Natl Acad Sci Usa*, vol. 91, pp. 11782–11786, dec 1994.

[11] R. Lipowsky and S. Liepelt, "Chemomechanical Coupling of Molecular Motors: Thermodynamics, Network Representations, and Balance Conditions," *Journal of Statistical Physics*, vol. 130, p. 39, 2008.

[12] M. Lindén, "Decay times in turnover statistics of single enzymes," *Phys Rev E*, vol. 78, no. 1, p. 010901, 2008.

[13] N. van Kampen, *Stochastic processes in physics and chemistry*. 2007.

[14] T. Schmiedl and U. Seifert, "Stochastic thermodynamics of chemical reaction networks," *J Chem Phys*, vol. 126, no. 4, p. 044101, 2007.

[15] G. Strang, "Linear algebra and its applications," *Harcourt, Brace, Jovanovich*, vol. 3rd Ed., 1988.

[16] J. Schnakenberg, "Network Theory of Microscopic and Macroscopic Behavior of Master Equation Systems," *Rev Mod Phys*, vol. 48, no. 4, pp. 571–585, 1976.

[17] J. Heron, "The Kinetics of Linear Systems with Special Reference to Periodic Reactions," *Bulletin of Mathematical Biophysics*, vol. 15, pp. 121–141, 1953.

[18] F. Karpelevich, "On the characteristic roots of matrices with nonnegative elements," *Eleven papers translated from the Russian*, p. 79, 1989.

[19] H. Ito, "A new statement about the theorem determining the region of eigenvalues of stochastic matrices," *Linear Algebra and Its Applications*, vol. 267, pp. 241–246, 1997.

[20] R. Kellogg and A. Stephens, "Complex Eigenvalues of a Non-Negative Matrix with a Specified Graph," *Linear Algebra and Its Applications*, vol. 20, no. 2, pp. 179–187, 1978.

[21] A. Z. Ivanović, Ž. D. Čupić, M. M. Janković, L. Z. Kolar-Anić, and S. R. Anić, "The chaotic sequences in the Bray–Liebhafsky reaction in an open reactor," *Phys. Chem. Chem. Phys.*, vol. 10, no. 38, p. 5848, 2008.

[22] L. Morelli and F. Jülicher, "Precision of Genetic Oscillators and Clocks," *Phys Rev Lett*, vol. 98, no. 22, p. 228101, 2007.

[23] H. Qian, S. Saffarian, and E. Elson, "Concentration fluctuations in a mesoscopic oscillating chemical reaction system," *P Natl Acad Sci Usa*, vol. 99, no. 16, pp. 10376–10381, 2002.

[24] P. Gaspard, "The correlation time of mesoscopic chemical clocks," *J Chem Phys*, vol. 117, no. 19, pp. 8905–8916, 2002.

[25] T. J. Xiao, Z. Hou, and H. Xin, "Entropy production and fluctuation theorem along a stochastic limit cycle," *J Chem Phys*, vol. 129, no. 11, p. 114506, 2008.

[26] D. Andrieux and P. Gaspard, "Fluctuation theorem and mesoscopic chemical clocks," *J Chem Phys*, vol. 128, no. 15, p. 154506, 2008.

[27] D. Gonze, J. Halloy, and P. Gaspard, "Biochemical clocks and molecular noise- Theoretical study of robustness factors," *J Chem Phys*, vol. 116, no. 24, pp. 10997–11010, 2002.

[28] P. Egleston, T. Lenker, and S. Narayan, "The nonnegative inverse eigenvalue problem," *Linear Algebra and Its Applications*, vol. 379, pp. 475–490, 2004.

[29] G. Baldini, F. Cannone, and G. Chirico, "Pre-unfolding resonant oscillations of single green fluorescent protein molecules," *Science*, vol. 309, no. 5737, pp. 1096–1100, 2005.

[30] G. Baldini, F. Cannone, G. Chirico, M. Collini, B. Campanini, S. Bettati, and A. Mozzarelli, "Evidence of discrete substates and unfolding pathways in green fluorescent protein," *Biophys J*, vol. 92, no. 5, pp. 1724–1731, 2007.

[31] F. Cannone, M. Collini, G. Chirico, G. Baldini, S. Bettati, B. Campanini, and A. Mozzarelli, "Environment effects on the oscillatory unfolding kinetics of GFP," *Eur Biophys J Biophy*, vol. 36, no. 7, pp. 795–803, 2007.

[32] F. Cannone, M. Caccia, S. Bologna, A. Diaspro, and G. Chirico, "Single molecule spectroscopic characterization of GFP-mut2 mutant for two-photon microscopy applications," *Microsc. Res. Tech.*, vol. 65, no. 4-5, pp. 186–193, 2005.

[33] G. Baldini, "Pre-Unfolding Resonant Oscillations of Single Green Fluorescent Protein Molecules," *Science*, vol. 309, no. 5737, pp. 1096–1100, 2005.

[34] D. Morre, P. Chueh, J. Pletcher, X. Tang, L. Wu, and D. Morre, "Biochemical basis for the biological clock," *Biochemistry-Us*, vol. 41, no. 40, pp. 11941–11945, 2002.

[35] D. J. Morre, Z. Jiang, M. Marjanovic, J. Orczyk, and D. M. Morre, "Response of the regulatory oscillatory behavior of copper(II)-containing ECTO-NOX proteins and of (CuCl2)-Cl-II in solution to electromagnetic fields," *J Inorg Biochem*, vol. 102, no. 9, pp. 1812–1818, 2008.

[36] J. Pleiss and F. Jähnig, "Collective vibrations of an alpha-helix. A molecular dynamics study," *Biophys J*, vol. 59, pp. 795–804, apr 1991.

[37] J. A. McCammon, "Protein Dynamics," *Rep. Prog. Phys.*, vol. 47, no. 1, pp. 1–46, 1984.

[38] N. Agmon, "Kinetics of switchable proton escape from a proton-wire within green fluorescence protein," *J. Phys. Chem. B*, vol. 111, no. 27, pp. 7870–7878, 2007.

[39] C. Camilloni, A. G. Rocco, I. Eberini, E. Gianazza, R. A. Broglia, and G. Tiana, "Urea and Guanidinium Chloride Denature Protein L in Different Ways in Molecular Dynamics Simulations," *Biophys J*, vol. 94, pp. 4654–4661, mar 2008.

[40] B. Bennion and V. Daggett, "The molecular basis for the chemical denaturation of proteins by urea," *P Natl Acad Sci Usa*, vol. 100, no. 9, pp. 5142–5147, 2003.

[41] F. Vanzi, B. Madan, and K. Sharp, "Effect of the protein denaturants urea and guanidinium on water structure: A structural and thermodynamic study," *J Am Chem Soc*, vol. 120, no. 41, pp. 10748–10753, 1998.

[42] F. Cannone, M. Collini, G. Chirico, G. Baldini, S. Bettati, B. Campanini, and A. Mozzarelli, "Environment effects on the oscillatory unfolding kinetics of GFP," *Eur Biophys J*, vol. 36, pp. 795–803, aug 2007.

[43] A. Saxena, J. Udgaonkar, and G. Krishnamoorthy, "Protein dynamics control proton transfer from bulk solvent to protein interior: A case study with a green fluorescent protein," *Protein Science*, vol. 14, no. 7, pp. 1787–1799, 2005.

[44] K. Brejc, T. Sixma, P. Kitts, S. Kain, R. Tsien, M. Ormo, and S. Remington, "Structural basis for dual excitation and photoisomerization of the Aequorea victoria green fluorescent protein," *P Natl Acad Sci Usa*, vol. 94, no. 6, pp. 2306–2311, 1997.

[45] Schrödinger, LLC, "The PyMOL Molecular Graphics System, Version 1.3r1." PyMOL The PyMOL Molecular Graphics System, Version 1.3, Schrödinger, LLC., aug 2010.

[46] M. S. Titushin, Y. Feng, G. A. Stepanyuk, Y. Li, S. V. Markova, S. Golz, B. C. Wang, J. Lee, J. Wang, E. S. Vysotski, and Z. J. Liu, "NMR-derived Topology of a GFP-photoprotein Energy Transfer Complex," *Journal of Biological Chemistry*, vol. 285, pp. 40891–40900, dec 2010.

[47] Z. Liu, S. Markova, F. LA, G. Stepanyuk, E. Vysotski, J. Rose, and W. BC, "PDB ID: 2HPW."

[48] B. FC, T. Koetzle, G. Williams, E. Meyer Jr, M. Brice, J. Rodgers, O. Kennard, T. Shimanouchi, and M. Tasum, "The Protein Data Bank: A Computer-based Archival File For Macromolecular Structures," *J. of. Mol. Biol*, vol. 112, p. 535, 1977.

[49] S. Abbruzzetti, E. Grandi, C. Viappiani, S. Bologna, B. Campanini, S. Raboni, S. Bettati, and A. Mozzarelli, "Kinetics of acid-induced spectral changes in the GFPmut2 chromophore," *J Am Chem Soc*, vol. 127, no. 2, pp. 626–635, 2005.

[50] M. Bailyn, "Carnot and the Universal Heat Death," *Am J Phys*, vol. 53, no. 11, pp. 1092–1099, 1985.

[51] A. Xie, L. Kelemen, J. Hendriks, B. White, K. Hellingwerf, and W. Hoff, "Formation of a new buried charge drives a large-amplitude protein quake in photoreceptor activation," *Biochemistry-Us*, vol. 40, no. 6, pp. 1510–1517, 2001.

[52] K. Itoh and M. Sasai, "Dynamical transition and proteinquake in photoactive yellow protein," *P Natl Acad Sci Usa*, vol. 101, no. 41, pp. 14736–14741, 2004.

[53] N. Agmon, "Proton Pathways in Green Fluorescence Protein," *Biophys J*, vol. 88, pp. 2452–2461, jan 2005.

[54] K. Modig, E. Kurian, F. Prendergast, and B. Halle, "Water and urea interactions with the native and unfolded forms of a beta-barrel protein," *Protein Science*, vol. 12, no. 12, pp. 2768–2781, 2003.

[55] G. Chirico, F. Cannone, S. Beretta, A. Diaspro, B. Campanini, S. Bettati, R. Ruotolo, and A. Mozzarelli, "Dynamics of green fluorescent protein mutant2 in solution, on spin-coated glasses, and encapsulated in wet silica gels," *Protein Science*, vol. 11, no. 5, pp. 1152–1161, 2002.

[56] D. P. Aalberts and N. O. Hodas, "Asymmetry in RNA pseudoknots: observation and theory," *Nucleic Acids Research*, vol. 33, pp. 2210–2214, apr 2005.

[57] C. Bustamante, J. Marko, and E. Siggia, "Entropic elasticity of lambda-phage DNA.," *Science (New York*, 1994.

[58] D. Mathews, J. Sabina, M. Zuker, and D. Turner, "Expanded sequence dependence of thermodynamic parameters improves prediction of RNA secondary structure," *Journal of Molecular Biology*, vol. 288, no. 5, pp. 911–940, 1999.

[59] P.-g. De Gennes, *Scaling Concepts in Polymer Phyics*. Cornell University Press, 1979.

[60] S. Cocco, J. F. Marko, and R. Monasson, "Theoretical models for single-molecule DNA and RNA experiments: from elasticity to unzipping," *arXiv*, vol. cond-mat.soft, jun 2002.

[61] M. Fixman and J. Kovac, "Polymer Conformational Statistics .3. Modified Gaussian Models of Stiff Chains," *J Chem Phys*, vol. 58, no. 4, pp. 1564–1568, 1973.

[62] M. Carrion-Vazquez, A. Oberhauser, S. Fowler, P. Marszalek, S. Broedel, J. Clarke, and J. Fernandez, "Mechanical and chemical unfolding of a single protein: A comparison," in *Proc Natl Acad Sci Usa*, (Mayo Clin & Mayo Fdn, Dept Physiol & Biophys, Rochester, MN 55905 USA), pp. 3694–3699, Mayo Clin & Mayo Fdn, Dept Physiol & Biophys, Rochester, MN 55905 USA, 1999.

[63] J. Bridgewater, P. Boykin, and V. Roychowdhury, "Statistical mechanical load balancer for the web," *Phys Rev E*, vol. 71, p. 046133, apr 2005.

[64] A. Shreim, P. Grassberger, W. Nadler, B. Samuelsson, J. Socolar, and M. Paczuski, "Network Analysis of the State Space of Discrete Dynamical Systems," *Phys Rev Lett*, vol. 98, p. 4, may 2007.

[65] A. Mckane and T. Newman, "Predator-Prey Cycles from Resonant Amplification of Demographic Stochasticity," *Phys Rev Lett*, vol. 94, p. 218102, jun 2005.

[66] D. Wu, K. Ghosh, M. Inamdar, H. J. Lee, S. Fraser, K. Dill, and R. Phillips, "Trajectory Approach to Two-State Kinetics of Single Particles on Sculpted Energy Landscapes," *Phys Rev Lett*, vol. 103, p. 50603, jul 2009.

[67] J. Kaneshiro, S. Kawado, H. Yokota, Y. Uesu, and T. Fukui, "Three-dimensional observations of polar domain structures using a confocal second-harmonic generation interference microscope," *J Appl Phys*, vol. 104, no. 5, p. 054112, 2008.

[68] S. Zhuo, J. Chen, X. Jiang, S. Xie, R. Chen, N. Cao, Q. Zou, and S. Xiong, "The layered–resolved microstructure and spectroscopy of mouse oral mucosa using multiphoton microscopy," *Phys. Med. Biol.*, vol. 52, pp. 4967–4980, aug 2007.

[69] J. A. Palero, H. S. de Bruijn, A. van der Ploeg Van Den Heuvel, H. J. C. M. Sterenborg, and H. C. Gerritsen, "Spectrally Resolved Multiphoton Imaging of In Vivo and Excised Mouse Skin Tissues," *Biophys J*, vol. 93, pp. 992–1007, may 2007.

[70] M. Kobayashi, K. Fujita, O. Nakamura, and S. Kawata, "Time-gated imaging for multifocus second-harmonic generation microscopy," *Rev. Sci. Instrum.*, vol. 76, no. 7, p. 073704, 2005.

[71] P. Stoller, P. Celliers, and K. Reiser, "Quantitative second-harmonic generation microscopy in collagen," *Appl Optics*, 2003.

[72] P. Stoller, K. Reiser, P. Celliers, and A. Rubenchik, "Polarization-modulated second harmonic generation in collagen," *Biophys J*, vol. 82, no. 6, pp. 3330–3342, 2002.

[73] R. Gauderon and P. Lukins, "Simultaneous multichannel nonlinear imaging: combined two-photon excited fluorescence and second-harmonic generation microscopy," *Micron*, 2001.

[74] B. Kim, J. Eichler, and L. Da Silva, "Frequency doubling of ultrashort laser pulses in biological tissues," *Appl Optics*, vol. 38, no. 34, pp. 7145–7150, 1999. Good sample of SHG active biological tissues.

[75] I. Freund and M. Deutsch, *Optical second-harmonic microscopy, crossed-beam summation and small-angle scattering in rat-tail tendon.* Biophys J, 1986.

[76] S. Fine and W. Hansen, "Optical second harmonic generation in biological systems," *Appl Optics*, vol. 10, no. 10, p. 2350, 1971.

[77] A. N. Bashkatov, E. A. Genina, and V. V. Tuchin, "Optical Properties of Skin, Subcutaneous, and Muscle Tissues: a Review," *J. Innov. Opl. Health Sci.*, vol. 4, no. 1, pp. 9–38, 2011.

[78] M. Andersen and S. Nir, "Van der Waals parameters, refractive indices and dispersion equations of spectrin, actin and other mammalian proteins," *Polymer*, vol. 18, pp. 867–870, 1977.

[79] F. Bolin, L. Preuss, R. Taylor, and R. J. Ference, "Refractive index of some mammalian tissues using a fiber optic cladding method," *Appl Optics*, pp. 2297–2303, 1989.

[80] F. Boman, M. Musorrafiti, J. Gibbs, B. Stepp, A. Salazar, S. Nguyen, and F. Geiger, "DNA single strands tethered to fused quartz/water interfaces studied by second harmonic generation," *J Am Chem Soc*, vol. 127, no. 44, pp. 15368–15369, 2005.

[81] A. J. Moad, C. W. Moad, J. M. Perry, R. D. Wampler, G. S. Goeken, N. J. Begue, T. Shen, R. Heiland, and G. J. Simpson, "NLOPredict: Visualization and data analysis software for nonlinear optics," *J. Comput. Chem.*, vol. 28, pp. 1996–2002, sep 2007.

[82] W. Williamson III, Y. Wang, S. Lee, and H. Simon, "Observation of optical second harmonic generation in wet-spun films of Na-DNA," *Spectroscopy ...*, 1993.

[83] YassineMrabet, "584px-Human_anatomy_planes.png by YassineMrabet. Wikimedia Commons." Wikimedia Commons, apr 2011.

[84] R. LaComb, O. Nadiarnykh, S. Townsend, and P. Campagnola, "Phase matching considerations in second harmonic generation from tissues: Effects on emission ...," *Optics Communications*, 2008.

[85] I. Asselberghs, C. Flors, L. Ferrighi, E. Botek, B. Champagne, H. Mizuno, R. Ando, A. Miyawaki, J. Hofkens, M. V. d. Auweraer, and K. Clays, "Second-Harmonic Generation in GFP-like Proteins," *J Am Chem Soc*, vol. 130, pp. 15713–15719, nov 2008.

[86] T. A. Theodossiou, C. Thrasivoulou, C. Ekwobi, and D. L. Becker, "Second Harmonic Generation Confocal Microscopy of Collagen Type I from Rat Tendon Cryosections," *Biophys J*, vol. 91, pp. 4665–4677, dec 2006.

[87] X. Deng, E. Williams, E. Thompson, X. Gan, and M. Gu, "Second-harmonic generation from biological tissues: Effect of excitation wavelength," *Scanning*, vol. 24, no. 4, pp. 175–178, 2002.

[88] K. E. Davies and K. J. Nowak, "Molecular mechanisms of muscular dystrophies: old and new players," *Nat Rev Mol Cell Biol*, vol. 7, pp. 762–773, sep 2006.

[89] O. Friedrich, M. Both, C. Weber, S. SchUrmann, M. D. H. Teichmann, F. von Wegner, R. H. A. Fink, M. Vogel, J. S. Chamberlain, and C. Garbe, "Microarchitecture Is Severely Compromised but Motor Protein Function Is Preserved in Dystrophic mdx Skeletal Muscle," *Biophys J*, vol. 98, pp. 606–616, feb 2010.

[90] I. Agarkova and J.-C. Perriard, "The M-band: an elastic web that crosslinks thick filaments in the center of the sarcomere," *Trends in Cell Biology*, vol. 15, pp. 477–485, sep 2005.

[91] P. Luther, P. Munro, and J. M. Squire, "Three-dimensional structure of the vertebrate muscle A-band* 1:: III. M-region structure and myosin filament symmetry," *Journal of Molecular Biology*, vol. 151, pp. 704–730, 1981.

[92] S. Shafiq, "Electron microscopic studies on the indirect flight muscles of Drosophila melanogaster," *The Journal of cell biology*, 1963.

[93] B. Millman, "The filament lattice of striated muscle," *Physiological reviews*, 1998.

[94] J. Harford and J. Squire, ""Crystalline" myosin cross-bridge array in relaxed bony fish muscle. Low-angle x-ray diffraction from plaice fin muscle and its interpretation," *Biophys J*, vol. 50, pp. 145–155, jul 1986.

[95] T. Irving, S. Bhattacharya, I. Tesic, and J. Moore, "Changes in myofibrillar structure and function produced by N-terminal deletion of the regulatory light chain in Drosophila," *Journal of Muscle ...*, 2001.

[96] T. Irving, J. Konhilas, and D. Perry, "Myofilament lattice spacing as a function of sarcomere length in isolated rat myocardium," *American Journal of ...*, 2000.

[97] L. Peachy, "Sarcoplasmic Reticulum and Transverse Tubules of Frogs Sartorius," *J Cell Biol*, vol. 25, pp. 209–231, 1965.

[98] M. Ö. Raeker, F. Su, S. B. Geisler, A. B. Borisov, A. Kontrogianni-Konstantopoulos, S. E. Lyons, and M. W. Russell, "Obscurin is required for the lateral alignment of striated myofibrils in zebrafish," *Dev. Dyn.*, vol. 235, no. 8, pp. 2018–2029, 2006.

[99] M. Both, M. Vogel, O. Friedrich, F. v. Wegner, T. Künsting, R. H. A. Fink, and D. Uttenweiler, "Second harmonic imaging of intrinsic signals in muscle fibers in situ," *J. Biomed. Opt.*, vol. 9, no. 5, p. 882, 2004.

[100] G. Recher, D. Rouede, P. Richard, A. Simon, J.-J. Bellanger, and F. Tiaho, "Three distinct sarcomeric patterns of skeletal muscle revealed by SHG and TPEF Microscopy," *Opt Express*, vol. 17, no. 22, pp. 19763–19777, 2009.

[101] S. V. Plotnikov, A. C. Millard, P. J. Campagnola, and W. A. Mohler, "Characterization of the Myosin-Based Source for Second-Harmonic Generation from Muscle Sarcomeres," *Biophys J*, vol. 90, pp. 693–703, jan 2006.

[102] C. Greenhalgh, N. Prent, C. Green, and R. Cisek, "Influence of semicrystalline order on the second-harmonic generation efficiency in the anisotropic bands of myocytes," *Applied . . .*, 2007.

[103] P. J. Campagnola, A. C. Millard, M. Terasaki, P. E. Hoppe, C. J. Malone, and W. A. Mohler, "Three-Dimensional High-Resolution Second-Harmonic Genera-

tion Imaging of Endogenous Structural Proteins in Biological Tissues," *Biophys J*, vol. 82, pp. 493–508, jan 2002.

[104] J. Squire, "Architecture and function in the muscle sarcomere," *Current Opinion in Structural Biology*, 1997.

[105] N. Prent, C. Green, C. Greenhalgh, and R. Cisek, "Intermyofilament dynamics of myocytes revealed by second harmonic generation microscopy," *Journal of Biomedical ...*, 2008.

[106] V. Nucciotti, C. Stringari, L. Sacconi, F. Vanzi, L. Fusi, M. Linari, G. Piazzesi, V. Lombardi, and F. S. Pavone, "Probing myosin structural conformation in vivo by second-harmonic generation microscopy," *Proceedings of the National Academy of Sciences*, vol. 107, pp. 7763–7768, apr 2010.

[107] J. Harford and J. Squire, "Time-resolved diffraction studies of muscle using synchrotron radiation," *Rep. Prog. Phys.*, vol. 60, no. 12, pp. 1723–1787, 1997.

[108] A. V. Smolensky, "Length-dependent filament formation assessed from birefringence increases during activation of porcine tracheal muscle," *The Journal of Physiology*, vol. 563, pp. 517–527, dec 2004.

[109] S. Baylor and H. Oetliker, "The optical properties of birefringence signals from single muscle fibres.," *The Journal of Physiology*, vol. 264, pp. 163–198, 1977.

[110] D. Taylor, "Quantitative studies on the polarization optical properties of striated muscle. I. Birefringence changes of rabbit psoas muscle in the transition

from rigor to relaxed state.," *The Journal of cell biology*, vol. 68, pp. 497–511, 1976.

[111] J. Zondy, "Comparative theory of walkoff-limited type-II versus type-I second harmonic generation with Gaussian beams," *Optics Communications*, 1991.

[112] G. Boyd, A. Ashkin, J. M. Dziedzic, and D. Kleinman, "Second-Harmonic Generation of Light with Double Refraction," *Physical Review*, vol. 137, pp. 1305–1320, 1965.

[113] R. W. Boyd, *Nonlinear Optics*. Academic Press, 2nd ed., 2003.

[114] S. Ishiwata and N. Okamura, "Diffraction rings obtained from a suspension of skeletal myofibrils by laser light illumination. Study of internal structure of sarcomeres," *Biophys J*, vol. 56, pp. 1113–1120, dec 1989.

[115] W. G. Gilliar, W. S. Bickel, and W. F. Bailey, "Light diffraction studies of single muscle fibers as a function of fiber rotation," *Biophys J*, vol. 45, pp. 1159–1165, jun 1984.

[116] R. Rüdel and F. Zite-Ferenczy, "Interpretation of light diffraction by cross-striated muscle as Bragg reflexion of light by the lattice of contractile proteins.," *The Journal of Physiology*, vol. 290, pp. 317–330, 1979.

[117] D. K. Sardar, G.-Y. Swanland, R. M. Yow, R. J. Thomas, and A. T. C. Tsin, "Optical properties of ocular tissues in the near infrared region," *Lasers Med Sci*, vol. 22, pp. 46–52, dec 2006.

[118] J. Dirckx, L. Kuypers, and W. Decraemer, "Refractive index of tissue measured with conflocal microscopy," *J. Biomed. Opt.*, vol. 10, no. 4, pp. –, 2005.

[119] H. Ding, J. Q. Lu, W. A. Wooden, P. J. Kragel, and X.-H. Hu, "Refractive indices of human skin tissues at eight wavelengths and estimated dispersion relations between 300 and 1600 nm," *Phys. Med. Biol.*, vol. 51, pp. 1479–1489, mar 2006.

[120] S. Cheng, H. Y. Shen, G. Zhang, C. H. Huang, and X. J. Huang, "Measurement of the refractive index of biotissue at four laser wavelengths," *Proc. SPIE*, vol. 4916, pp. 172–176, 2002.

[121] S.-W. Chu, S.-Y. Chen, G.-W. Chern, T.-H. Tsai, Y.-C. Chen, B.-L. Lin, and C.-K. Sun, "Studies of (2)/(3) Tensors in Submicron-Scaled Bio-Tissues by Polarization Harmonics Optical Microscopy," *Biophys J*, vol. 86, pp. 3914–3922, jun 2004.

[122] D. I. Bassett, "Dystrophin is required for the formation of stable muscle attachments in the zebrafish embryo," *Development*, vol. 130, pp. 5851–5860, dec 2003.

[123] J. Sprague, L. Bayraktaroglu, D. Clements, T. Conlin, D. Fashena, K. Frazer, M. Haendel, D. G. Howe, P. Mani, S. Ramachandran, K. Schaper, E. Segerdell, P. Song, B. Sprunger, S. Taylor, C. E. Van Slyke, and M. Westerfield, "The Zebrafish Information Network: the zebrafish model organism database," *Nucleic Acids Research*, vol. 34, pp. D581–D585, 2006.

[124] R. Chang, J. Eickmans, W. Hsieh, C. F. Wood, J.-Z. Zhang, and J.-b. Zheng, "Laser-induced breakdown in large transparent water droplets," *Appl Optics*, vol. 27, pp. 2377–2385, 1988.

[125] J. P. Singh and S. N. Thakur, eds., *Laser-Induced Breakdown Spectroscopy*. Elsevier, 1st ed., 2007.

[126] F. DeMartini, C. Townes, T. Gustafson, and P. L. Kelly, "Self-steepening of light pulses," *Physical Review*, vol. 164, pp. 312–312, 1967.

[127] W. Liu, O. Kosareva, I. Golubtsov, A. Iwasaki, A. Becker, V. Kandidov, and S. Chin, "Femtosecond laser pulse filamentation versus optical breakdown in H 2 O," *Applied Physics B: Lasers and Optics*, vol. 76, pp. 215–229, mar 2003.

[128] C. Santhosh, A. K. Dharmadhikari, K. Alti, J. A. Dharmadhikari, and D. Mathura, "Suppression of ultrafast supercontinuum generation in a salivary protein," *J. Biomed. Opt.*, vol. 12, no. 2, pp. –, 2007. interesting point to make about damage to zebrafish by lasers – observation of supercontinuum generation.

[129] S. Schürmann, F. von Wegner, R. H. A. Fink, O. Friedrich, and M. Vogel, "Second Harmonic Generation Microscopy Probes Different States of Motor Protein Interaction in Myofibrils," *Biophys J*, vol. 99, pp. 1842–1851, sep 2010.

[130] C. J. Snow, M. Goody, M. W. Kelly, E. C. Oster, R. Jones, A. Khalil, and C. A. Henry, "Time-Lapse Analysis and Mathematical Characterization Eluci-

date Novel Mechanisms Underlying Muscle Morphogenesis," *PLoS Genet*, vol. 4, p. e1000219, oct 2008.

[131] A. S. Jacoby, E. Busch-Nentwich, R. J. Bryson-Richardson, T. E. Hall, J. Berger, S. Berger, C. Sonntag, C. Sachs, R. Geisler, D. L. Stemple, and P. D. Currie, "The zebrafish dystrophic mutant softy maintains muscle fibre viability despite basement membrane rupture and muscle detachment," *Development*, vol. 136, pp. 3367–3376, sep 2009.

[132] J. W. Sanger, J. Wang, B. Holloway, A. Du, and J. M. Sanger, "Myofibrillogenesis in skeletal muscle cells in zebrafish," *Cell Motil. Cytoskeleton*, vol. 66, pp. 556–566, aug 2009.

[133] J. D. Jackson, *Classical Electrodynamics Third Edition*. Wiley, 1998.

[134] P. N. Butcher and D. Cotter, *The Elements of Nonlinear Optics*. Cambridge University Press, first ed., mar 1990.

[135] W. Xiang-Hui, L. Lie, C. Sheng-Jiang, Z. Hao, and H. Shu-Juan, "Examination of validity of paraxial approximation in second harmonic generation microscopy under low numerical aperture," *Chinese Phys Lett*, vol. 25, no. 8, pp. 2884–2887, 2008.

[136] S. Hess and W. Webb, "Focal volume optics and experimental artifacts in confocal fluorescence correlation spectroscopy," *Biophys J*, vol. 83, no. 4, pp. 2300–2317, 2002.

[137] P. Varga, "The Gaussian wave solution of Maxwell's equations and the validity of scalar wave approximation," *Optics Communications*, 1998.

[138] D. Kleinman, "Dependence of second-harmonic generation on the position of the focus," *Physical Review*, 1966.

[139] D. Kleinman and A. Ashkin, "Second-harmonic generation of light by focused laser beams," *Physical Review*, 1966. Fundamental derivation of gaussian focused SHG.

[140] L. Moreaux, O. Sandre, and J. Mertz, "Membrane imaging by second-harmonic generation microscopy," *J Opt Soc Am B*, vol. 17, no. 10, pp. 1685–1694, 2000.

[141] J. Bjorkholm, "Optical second-harmonic generation using a focused Gaussian laser beam," *Physical Review*, 1966.

[142] V. Berger, "Nonlinear photonic crystals," *Phys Rev Lett*, 1998.

[143] P. Xu, S. Ji, S. Zhu, X. Yu, J. Sun, H. Wang, J. He, Y. Zhu, and N. Ming, "Conical Second Harmonic Generation in a Two-Dimensional (2) Photonic Crystal: A Hexagonally Poled LiTaO3 Crystal," *Phys Rev Lett*, vol. 93, sep 2004.

[144] N. Broderick, G. Ross, and H. Offerhaus, "Hexagonally poled lithium niobate: a two-dimensional nonlinear photonic crystal," *Phys Rev Lett*, 2000.

[145] A. Arie, N. Habshoosh, and A. Bahabad, "Quasi phase matching in two-dimensional nonlinear photonic crystals," *Opt Quant Electron*, vol. 39, pp. 361–375, jun 2007.

[146] D. Kleinman and A. Ashkin, "Second-harmonic generation of light by focused laser beams," *Physical Review*, 1966.

[147] J. Mertz and L. Moreaux, "Second-harmonic generation by focused excitation of inhomogeneously distributed scatterers," *Optics Communications*, 2001.

[148] R. Miller, "Optical second harmonic generation in piezoelectric crystals," *Appl. Phys. Lett.*, vol. 5, pp. 17–19, 1964.

[149] C. Garrett and F. Robinson, "Miller's phenomenological rule for computing nonlinear susceptibilities," *Quantum Electronics*, vol. 2, pp. 328–329, 1966.

[150] S. Scandolo, "Miller's rule and the static limit for second-harmonic generation," *Phys Rev B*, vol. 51, no. 11, pp. 6928–6931, 1995.

[151] G. Boyd and D. Kleinman, "Parametric Interaction of Focused Gaussian Light Beams," *J Appl Phys*, vol. 39, no. 8, pp. 3597–3639, 1968.

[152] G. Boyd, "Parametric interaction of focused Gaussian light beams," *J Appl Phys*, 1968.

[153] F. Brejat and B. Wyncke, "Calculation of Double-Refraction Walk-Off Angle Along the Phase-Matching Directions in Non-Linear Biaxial Crystals," *J. Phys. B: At. Mol. Opt. Phys.*, vol. 22, no. 11, pp. 1891–1898, 1989.

[154] M. Fejer, G. Magel, D. Jundt, and R. L. Byer, "Quasi-phase-matched second harmonic generation: tuning and tolerances," *IEEEE Journal of Quantum Electronics*, vol. 28, no. 11, pp. 2631–2654, 1992.

[155] Y. R. Shen and V. Ostroverkhov, "Sum-Frequency Vibrational Spectroscopy on Water Interfaces: Polar Orientation of Water Molecules at Interfaces," *Chem Rev*, vol. 106, pp. 1140–1154, apr 2006.

[156] P. Jungwirth and D. J. Tobias, "Specific ion effects at the air/water interface," *Chem Rev*, vol. 106, pp. 1259–1281, apr 2006.

[157] C. J. Mundy and I. F. W. Kuo, "First-principles approaches to the structure and reactivity of atmospherically relevant aqueous interfaces," *Chem Rev*, vol. 106, pp. 1282–1304, apr 2006.

[158] T. M. Chang and L. X. Dang, "Recent advances in molecular simulations of ion solvation at liquid interfaces," *Chem Rev*, vol. 106, pp. 1305–1322, apr 2006.

[159] G. L. Richmond, "Molecular bonding and interactions at aqueous surfaces as probed by vibrational sum frequency spectroscopy," *Chem Rev*, vol. 102, pp. 2693–2724, aug 2002.

[160] Y. A. Mantz, F. M. Geiger, L. T. Molina, and B. L. Trout, "First-principles theoretical study of molecular HCl adsorption on a hexagonal ice (0001) surface," *J Phys Chem A*, vol. 105, pp. 7037–7046, jul 2001.

[161] S. Narayan, J. Muldoon, M. G. Finn, V. V. Fokin, H. C. Kolb, and K. B. Sharpless, ""On water": Unique reactivity of organic compounds in aqueous suspension," *Angew Chem Int Edit*, vol. 44, no. 21, pp. 3275–3279, 2005.

[162] F. Niu, C.-C. Liu, Z.-M. Cui, J. Zhai, L. Jiang, and W.-G. Song, "Promotion of organic reactions by interfacial hydrogen bonds on hydroxyl group rich nanosolids," *Chem. Commun.*, pp. 2803–2805, 2008.

[163] Q. Du, R. Superfine, E. Freysz, and Y. R. Shen, "Vibrational Spectroscopy of Water at the Vapor Water Interface," *Phys Rev Lett*, vol. 70, pp. 2313–2316, apr 1993.

[164] F. Vidal and A. Tadjeddine, "Sum-firequency generation spectroscopy of interfaces," *Rep. Prog. Phys.*, vol. 68, pp. 1095–1127, may 2005.

[165] C. Y. Lee, J. A. Mccammon, and P. J. Rossky, "The Structure of Liquid Water at an Extended Hydrophobic Surface," *J Chem Phys*, vol. 80, no. 9, pp. 4448–4455, 1984.

[166] K. B. Eisenthal, "Liquid interfaces probed by second-harmonic and sum-frequency spectroscopy," *Chem Rev*, vol. 96, pp. 1343–1360, jun 1996.

[167] S. Gopalakrishnan, P. Jungwirth, D. J. Tobias, and H. C. Allen, "Air-liquid interfaces of aqueous solutions containing ammonium and sulfate: Spectroscopic and molecular dynamics studies," *J. Phys. Chem. B*, vol. 109, pp. 8861–8872, may 2005.

[168] W. Gan, D. Wu, Z. Zhang, R. Feng, and H. Wang, "Polarization and experimental configuration analyses of sum frequency generation vibrational spectra, structure, and orientational motion of the air/water interface," *J Chem Phys*, vol. 124, p. 114705, mar 2006.

[169] L. X. Dang and T. M. Chang, "Molecular dynamics study of water clusters, liquid, and liquid-vapor interface of water with many-body potentials," *J Chem Phys*, vol. 106, pp. 8149–8159, may 1997.

[170] A. Morita and J. T. Hynes, "A theoretical analysis of the sum frequency generation spectrum of the water surface," *Chemical Physics*, vol. 258, pp. 371–390, aug 2000.

[171] V. Buch, "Molecular structure and OH-stretch spectra of liquid water surface," *J. Phys. Chem. B*, vol. 109, pp. 17771–17774, sep 2005.

[172] R. S. Taylor, L. X. Dang, and B. C. Garrett, "Molecular dynamics simulations of the liquid/vapor interface of SPC/E water," *J Phys Chem-Us*, vol. 100, pp. 11720–11725, jul 1996.

[173] A. Perry, C. Neipert, B. Space, and P. B. Moore, "Theoretical modeling of interface specific vibrational spectroscopy: Methods and applications to aqueous interfaces," *Chem Rev*, vol. 106, pp. 1234–1258, apr 2006.

[174] L. F. Scatena, M. G. Brown, and G. L. Richmond, "Water at hydrophobic surfaces: Weak hydrogen bonding and strong orientation effects," *Science*, vol. 292, pp. 908–912, may 2001.

[175] M. G. Brown, D. S. Walker, E. A. Raymond, and G. L. Richmond, "Vibrational sum-frequency spectroscopy of akane/water interfaces: Experiment and theoretical simulation," *J. Phys. Chem. B*, vol. 107, pp. 237–244, jan 2003.

[176] I.-F. W. Kuo, C. J. Mundy, B. L. Eggimann, M. J. McGrath, J. I. Siepmann, B. Chen, J. Vieceli, and D. J. Tobias, "Structure and Dynamics of the Aqueous Liquid-Vapor Interface: A Comprehensive Particle-Based Simulation Study," *J. Phys. Chem. B*, vol. 110, pp. 3738–3746, 2006.

[177] H.-S. Lee and M. E. Tuckerman, "Ab Initio Molecular Dynamics Studies of the Liquid-Vapor Interface of an HCl Solution," *J Phys Chem A*, vol. 113, pp. 2144–2151, 2009.

[178] E. C. Brown, M. Mucha, P. Jungwirth, and D. H. Tobias, "Structure and Vibrational Speectroscopy of Salt Water/Air Interfaces: Predictions from Classical Molecular Dynamics Simulations," *J. Phys. Chem. B*, vol. 109, no. 7934, pp. 7934–7940, 2005.

[179] A. Perry, C. Neipert, C. Ridley, and B. Space, "Identification of a wagging vibrational mode of water molecules at the water/vapor interface," *Phys Rev E*, vol. 71, no. 050601(R), p. 050601(R), 2005.

[180] A. Morita and J. T. Hynes, "A Theoretical Analysis of the Sum Frequency Generation Spectrum of the Water Surface. II. Time-Dependent Approach," *J. Phys. Chem. B*, vol. 106, pp. 673–685, 2002.

[181] B. M. Auer and J. L. Skinner, "Vibrational Sum-Frequency Spectroscopy of the Water Liquid/Vapor Interface," *J. Phys. Chem. B*, vol. 113, pp. 4125–4130, 2009.

[182] Y. Jung and R. A. Marcus, "On the theory of organic catalysis "on water"," *J Am Chem Soc*, vol. 129, pp. 5492–5502, may 2007.

[183] X. Wei and Y. Shen, "Motional Effect in Surface Sum-Frequency Vibrational Spectroscopy," *Phys Rev Lett*, vol. 86, pp. 4799–4802, may 2001.

[184] D. S. Walker, D. K. Hore, and G. L. Richmond, "Understanding the Population, Coordination, and Orientation of Water Species Contributing to the Nonlinear Optical Spectroscopy of the Vapor-Water Interface through Molecular Dynamics Simulations," *J. Phys. Chem. B*, vol. 110, pp. 20451–20459, 2006.

[185] X. Zhuang, P. B. Miranda, D. Kim, and Y. R. Shen, "Mapping molecular orientation and conformation at interfaces by surface nonlinear optics," *Phys Rev B*, vol. 59, pp. 12632–12640, may 1999.

[186] X. Wei, S. C. Hong, X. W. Zhuang, T. Goto, and Y. R. Shen, "Nonlinear optical studies of liquid crystal alignment on a rubbed polyvinyl alcohol surface," *Phys Rev E*, vol. 62, pp. 5160–5172, oct 2000.

[187] Y. Nagata and S. Mukamel, "Vibrational Sum-Frequency Generation Spectroscopy at the Water/Lipid Interface: Molecular Dynamics Simulation Study," *J Am Chem Soc*, vol. 132, pp. 6436–6442, 2010.

[188] P. N. Butcher and D. Cotter, *The Elements of Nonlinear Optics*. Cambridge University Press, 1990.

[189] B. M. Auer and J. L. Skinner, "Vibrational sum-frequency spectroscopy of the liquid/vapor interface for dilute HOD in D2O," *J Chem Phys*, vol. 129, p. 214705, 2008.

[190] Y. R. Shen, *The Principles of Nonlinear Optics*. J. Wiley, 2003.

[191] S. Mukamel, *Principles of Nonlinear Optical Spectroscopy*. Oxford University Press, 1995.

[192] W. Smith and T. R. Forester, *The DL_POLY 2 User Manual*. Daresbury, Warrington, England: CCLRC, Daresbury Laboratory, 1999.

[193] W. L. Jorgensen, J. Chandrasekhar, J. D. Madura, R. W. Impey, and M. L. Klein, "Comparison of Simple Potential Functions for Simulating Liquid Water," *J Chem Phys*, vol. 79, no. 2, pp. 926–935, 1983.

[194] S. Nosé, "A molecular-dynamics method for simulations in the canonical ensemble," *Mol. Phys.*, vol. 52, p. 255, 1984.

[195] W. G. Hoover, "Canonical dynamics - equilibrium phase-space distributions," *Phys. Rev. A*, vol. 31, p. 1695, 1985.

[196] J. P. Ryckaert, C. G, and H. J. C. Berendsen, "Numerical-integration of cartesian equations of motion of a system with constraints - molecular-dynamics of n-alkanes," *J. Comp. Phys.*, vol. 23, p. 327, 1977.

[197] P. Ye and Y. R. Shen, "Local-field effect on linear and nonlinear optical properties of adsorbed molecules," *Phys Rev B*, vol. 28, no. 8, pp. 4288–4294, 1983.

[198] Q. Du, E. Freysz, and Y. R. Shen, "Surface Vibrational Spectroscopic Studies of Hydrogen-Bonding and Hydrophobicity," *Science*, vol. 264, pp. 826–828, may 1994.

[199] A. Luzar and D. Chandler, "Effect of environment on hydrogen bond dynamics in liquid water," *Phys Rev Lett*, vol. 76, pp. 928–931, feb 1996.

[200] J. D. Eaves, J. J. Loparo, C. J. Fecko, S. T. Roberts, A. Tokmakoff, and P. L. Geissler, "Hydrogen bonds in liquid water are broken only fleetingly," *PNAS*, vol. 1 02, no. 37, pp. 13019–13022, 2005.

[201] H. J. C. Berendsen, J. R. Grigera, and T. P. Straatsma, "The missing term in effective pair potentials," *J Phys Chem-Us*, vol. 91, no. 24, pp. 6269–6271, 1987.